



HAL
open science

Volatile transport modeling on Triton with new observational constraints

T. Bertrand, E. Lellouch, B. J. Holler, L. A. Young, B. Schmitt, J. Marques Oliveira, B. Sicardy, F. Forget, W. M. Grundy, F. Merlin, et al.

► **To cite this version:**

T. Bertrand, E. Lellouch, B. J. Holler, L. A. Young, B. Schmitt, et al.. Volatile transport modeling on Triton with new observational constraints. *Icarus*, 2022, 373, 10.1016/j.icarus.2021.114764 . insu-03705379

HAL Id: insu-03705379

<https://insu.hal.science/insu-03705379>

Submitted on 5 Jan 2024

HAL is a multi-disciplinary open access archive for the deposit and dissemination of scientific research documents, whether they are published or not. The documents may come from teaching and research institutions in France or abroad, or from public or private research centers.

L'archive ouverte pluridisciplinaire **HAL**, est destinée au dépôt et à la diffusion de documents scientifiques de niveau recherche, publiés ou non, émanant des établissements d'enseignement et de recherche français ou étrangers, des laboratoires publics ou privés.



Distributed under a Creative Commons Attribution - NonCommercial 4.0 International License

1 Volatile transport modeling on Triton with new observational constraints

2

3 T. Bertrand^{1,2}, E. Lellouch², B. J. Holler³, L. A. Young⁴, B. Schmitt⁵, J. Marques Oliveira², B.
4 Sicardy², F. Forget⁶, W. M. Grundy⁷, F. Merlin², M. Vangvichith⁶, E. Millour⁶, P. Schenk⁸, C.
5 Hansen⁹, O. White¹, J. Moore¹, J. Stansberry³, A. Oza^{10,11}, D. Dubois¹, E. Quirico⁵, D.
6 Cruikshank¹

7

8 ¹ Laboratoire d'Etudes Spatiales et d'Instrumentation en Astrophysique (LESIA), Observatoire de
9 Paris, Université PSL, CNRS, Sorbonne Université, Univ. Paris Diderot, Sorbonne Paris Cité, 5
10 place Jules Janssen, 92195 Meudon, France

11 ² Ames Research Center, Space Science Division, National Aeronautics and Space
12 Administration (NASA), Moffett Field, CA, USA

13 ³ Space Telescope Science Institute, Baltimore, MD, USA

14 ⁴ Southwest Research Institute, Boulder, CO 80302

15 ⁵ Univ. Grenoble Alpes, CNRS, Institut de Planétologie et d'Astrophysique de Grenoble (IPAG),
16 38000 Grenoble, France

17 ⁶ Laboratoire de Météorologie Dynamique, IPSL, Sorbonne Universités, UPMC Université Paris
18 06, CNRS, Paris, France

19 ⁷ Lowell Observatory, 1400 W. Mars Hill Rd., Flagstaff, AZ 86001.

20 ⁸ Lunar and Planetary Institute, Houston, TX 77058, USA

21 ⁹ Planetary Science Institute, 1700 E. Fort Lowell, Suite 106, Tucson, AZ 85719, United States of
22 America

23 ¹⁰ Jet Propulsion Laboratory, California Institute of Technology, Pasadena, CA, USA

24 ¹¹ Physikalisches Institut, Universität Bern, Bern, Switzerland 3012

25 ABSTRACT

26 Neptune's moon Triton shares many similarities with Pluto, including volatile cycles of N₂, CH₄
27 and CO, and represents a benchmark case for the study of surface-atmosphere interactions on
28 volatile-rich Kuiper Belt objects. The observations of Pluto by New Horizons acquired during the
29 2015 flyby and their analysis with volatile transport models (VTMs) shed light on how volatile
30 sublimation-condensation cycles control the climate and shape the surface of such objects. Within
31 the context of New Horizons observations as well as recent Earth-based observations of Triton,
32 we adapt a Plutonian VTM to Triton, and test its ability to simulate its volatile cycles, thereby
33 aiding our understanding of its climate.

34 Here we present numerical VTM simulations exploring the volatile cycles of N₂, CH₄ and CO on
35 Triton over long-term and seasonal timescales (cap extent, surface temperatures, surface
36 pressure, sublimation rates) for varying model parameters (including the surface ice reservoir,
37 albedo, thermal inertia, and the internal heat flux). We explore what scenarios and model
38 parameters allow for a best match of the available observations. In particular, our set of
39 observational constraints include Voyager 2 observations (surface pressure and cap extent),
40 ground-based near-infrared (0.8 to 2.4 μm) disk-integrated spectra (the relative surface area of

41 volatile vs. non-volatile ice) and the evolution of surface pressure as retrieved from stellar
42 occultations.

43 Our results show that Triton's poles act as cold traps for volatile ices and favor the formation of
44 polar caps extending to lower latitudes through glacial flow or through the formation of thinner
45 seasonal deposits. As previously evidenced by other VTMs, North-South asymmetries in surface
46 properties can favor the development of one cap over the other. Our best-case simulations are
47 obtained for a bedrock surface albedo of 0.6-0.7, a global reservoir of N₂ ice thicker than 200 m,
48 and a bedrock thermal inertia larger than 500 SI (or smaller but with a large internal heat flux).
49 The large N₂ ice reservoir implies a permanent N₂ southern cap (several 100 m thick) extending
50 to the equatorial regions with higher amounts of volatile ice at the south pole, which is not
51 inconsistent with Voyager 2 images but does not fit well with observed full-disk near-infrared
52 spectra. Our results also suggest that a small permanent polar cap exists in the northern (currently
53 winter) hemisphere if the internal heat flux remains relatively low (e.g. radiogenic, < 3 mW m⁻²). A
54 non-permanent northern polar cap was only obtained in some of our simulations with high internal
55 heat flux (30 mW m⁻²). The northern cap will possibly extend to 30°N in the next decade, thus
56 becoming visible by Earth-based telescopes. On the basis of our model results, we also discuss
57 the composition of several surface units seen by Voyager 2 in 1989, including the bright equatorial
58 fringe and dark surface patches.

59 Finally, we provide predictions for the evolution of ice distribution, surface pressure and CO and
60 CH₄ atmospheric mixing ratios in the next decades. According to our model, the surface pressure
61 should slowly decrease but remain larger than 0.5 Pa by 2060. We also model the thermal
62 lightcurves of Triton for different climate scenarios in 2022, which serve as predictions for future
63 James Webb Space Telescope observations.

64

65 1. Introduction

66 The largest satellite of Neptune, Triton, is often described as Pluto's sibling, as the two bodies
67 share similar sizes, densities, ices (non-volatile H₂O and volatile N₂, CH₄, CO, Cruikshank et al.
68 1993, 2000, Quirico et al. 1999, De Meo et al., 2010, Merlin et al., 2018), and currently similar
69 heliocentric distances, surface pressures and temperatures, and atmosphere composition (N₂
70 with traces of CH₄ and CO). Its climate and albedo patterns are therefore expected to be
71 dominated by long-term and seasonal volatile condensation-sublimation cycles. However, the
72 geological history (and by extension, interior thermal history) of the two bodies differ: the portion
73 of Triton seen by Voyager 2 during the 1989 flyby has extremely flat topography (vs. dramatic
74 topography of Pluto, Schenk et al., 2018, 2021), an uncratered (geologically young) surface with
75 a globally high Bond albedo (~0.6-0.8, McEwen, 1990, Hillier et al., 1994) without low-albedo red
76 areas, and active geysers (Soderblom et al., 1990). Other differences between the two bodies
77 include the lower amount of atmospheric CH₄ and the colder temperatures in the lower (< 200 km)
78 atmosphere of Triton, ultimately related to the ~10x lower abundance of CH₄ in the ice on Triton,
79 the presence of CO₂ ice on Triton (forming the surface bedrock along with H₂O ice, Quirico et al.,
80 1999, Grundy et al., 2010, Merlin et al. 2018) and the location of the main volatile ice reservoir
81 (Sputnik Planitia on Pluto vs possibly an extended southern cap on Triton, Stern et al., 2015,
82 Smith et al., 1989).

83 These differences may be related to the fact that Triton is thought to be a captured Kuiper Belt
84 object (McKinnon, 1984; Agnor and Hamilton, 2006, Li et al., 2020) as it has a retrograde, highly
85 inclined orbit, with a differentiated interior possibly heated by tidal braking. This peculiar orbit
86 leads to complex seasons and possibly to strong obliquity tides and subsequent resurfacing
87 processes (e.g., cryovolcanism, Nimmo and Spencer, 2015). Consequently, Triton is a

88 benchmark case of a dwarf planet that is tidally activated by a giant planet and offers new insights
89 into the surface-atmosphere interactions controlling the climate of large volatile-rich objects of the
90 Kuiper Belt (including Pluto, and others that may exhibit a similar atmosphere near perihelion,
91 e.g. Eris and Makemake).

92 The flyby of Pluto by New Horizons in July 2015 highlighted the extraordinary complexity of the
93 best studied icy body of the Kuiper Belt (Stern et al., 2015). In particular, volatile transport models
94 (VTMs) of Pluto, constrained by the New Horizons observations, shed light on how the volatile
95 sublimation-condensation cycles can shape the surface of such a planetary body (Bertrand et al.,
96 2016, 2018, 2019, 2020a, 2020b, Johnson et al., 2020). In addition, the correlation of volatile ice
97 deposition with the large global topographic variability of Pluto's surface (total relief exceeding 10
98 km, with a standard deviation of 1.1 km, Schenk et al., 2018) also indicated the importance of
99 elevation in volatile ice transport on icy bodies with thin atmospheres (Trafton et al., 1998,
100 Bertrand and Forget, 2016). Within the context of New Horizons observations as well as recent
101 Earth-based observations of Triton, it is a natural step to adapt these better-constrained VTMs to
102 Triton and test their ability to simulate its volatile cycles, thereby aiding our understanding of its
103 climate.

104 Many fundamental issues remain unsolved regarding the climate and the volatile cycles on Triton,
105 which may shape Triton's surface as they do on Pluto. For instance, how do seasonal cycles
106 affect the volatile ice surface distribution, and over what temporal and spatial scales? Is the
107 southern cap seasonal or permanent? Does the winter hemisphere act as a sink for volatile ices?
108 If so, what is the extent and the nature (seasonal vs permanent) of the northern cap, considering
109 that Moore and Spencer (1990) suggested a long term net transfer of N₂ ice from the north to the
110 south and thus a more extended southern vs northern cap? Where are N₂ and CH₄ currently
111 sublimating and condensing? What are the properties of the volatile ices (thermal inertia,
112 reservoir, etc.)? How will the surface pressure, and CO and CH₄ gas abundances evolve? The
113 cases of Spencer and Moore (1992) that best match occultations had a non-global atmosphere
114 in the 1960's, so does Triton's atmosphere collapse (become non-global)? Near-infrared (NIR)
115 rotational lightcurves suggest the latitudes south of 60°S are bare of N₂ (or at least of large-
116 grained N₂, e.g. Grundy et al., 2010, Holler et al., 2016), but what could explain a difference in
117 composition between high southern latitudes and southern mid-latitudes? Finally, how do the
118 volatile cycles on Triton compare with those on Pluto?

119 Here we present numerical simulations designed to model the evolution of Triton's volatiles
120 (surface ice distribution, surface pressure, and atmospheric abundances) over millions of years
121 on the basis of universal physical equations put into practice with some hypotheses. Our main
122 goal is to investigate where the volatile ices tend to accumulate and sublimate on Triton as the
123 seasons change, and compare our results with the available observations. In particular, we
124 investigate if a perennial northern cap of nitrogen ice can form, and whether our simulations can
125 produce results that are consistent with Earth-based spectroscopic and stellar occultation
126 observations, as well as the observations of the surface by Voyager 2.

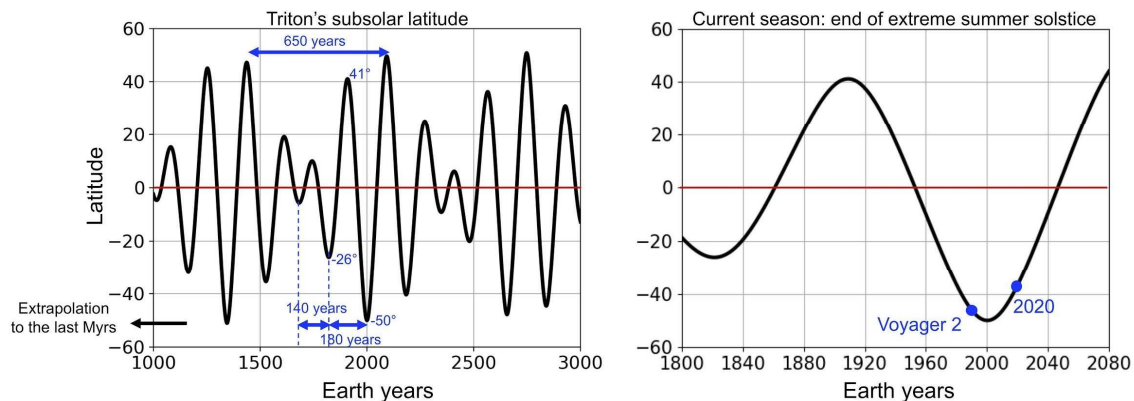
127 Section 2 gives an overview of the past observations of Triton relevant to volatile transport.
128 Section 3 describes the model used, the model parameters, the settings of the reference
129 simulations and defines what the best-case simulations would be. Section 4 discusses the
130 sensitivity of bedrock surface temperatures on Triton to several model parameters. Section 5
131 presents long-term volatile transport simulations performed over several millions of Earth years
132 (Myrs) and explores the impact of North-South asymmetries in internal heat flux, topography and
133 N₂ ice albedo on the ice distribution. Section 6 presents short-term volatile transport simulations
134 performed over several seasonal cycles with fixed N₂ ice reservoirs and explores the sensitivity
135 of the surface pressure cycle to different model parameters, including the ice distribution. Section
136 7 presents a large range of simulation results performed with the full volatile transport model and

137 explores what scenarios and model parameters allow for a best match of the available
138 observations. We discuss these results in Section 8 and provide predictions of Triton's climate for
139 the next decades and future observations with the James Webb Space Telescope (JWST).

140 2. Background: observations and characteristics of the volatile 141 cycle on Triton

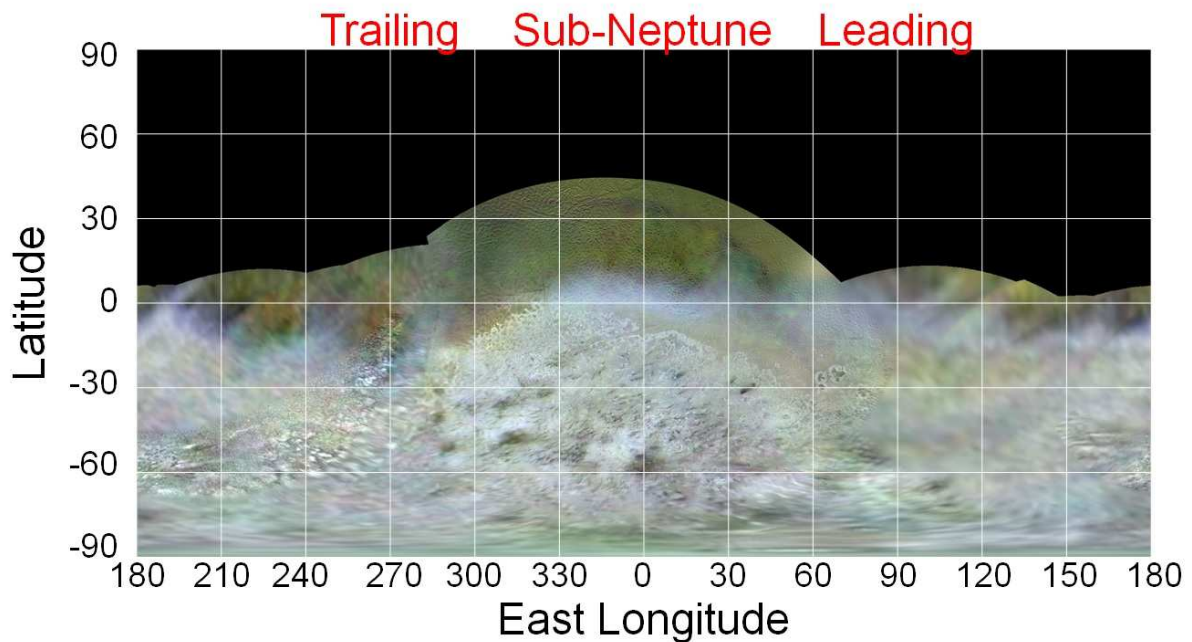
142 2.1 Triton's orbit and seasons

143 Triton is moving in a retrograde and circular orbit with an orbital inclination with respect to Neptune
144 of 157° , that is 23° above the planet's equator. It is tidally locked to Neptune with a rotation period
145 of 5.877 days. The combination of this inclination with Neptune's obliquity of 28° leads to complex
146 seasonal cycles, oscillating between low ($\sim 5^\circ$ latitude), moderate ($\sim 20^\circ$ latitude) and extreme
147 ($\sim 50^\circ$ latitude) summer solstices (Trafton, 1984, also see Appendix) over a period of 140-180
148 years. Each season on Triton lasts ~ 35 -45 terrestrial years. The recent epoch lasting from 1980–
149 2020, during which the highest quality observations of Triton were gathered, corresponds to a
150 period of intense summer in Triton's southern hemisphere (in particular at the south pole), as the
151 subsolar latitude of Triton reached $\sim 50^\circ\text{S}$ in 2000 (Figure 1), and follows a relatively intense
152 winter. At present, the subsolar latitude is rapidly migrating toward the equator. For instance, in
153 2021, the subsolar latitude will be 36°S and previously unseen regions in the northern hemisphere
154 will come into view (up to 54°N).



155

156 Figure 1: Variation of the subsolar latitude on Triton over time. Triton experiences periods with
157 low (e.g., years 2300-2400), moderate (e.g., years 1500-1650) and intense seasons (e.g., years
158 1850-2200).



160
161 Figure 2: Global color map mosaic of Triton (simple cylindrical projection) at 0.35 km/pixel, as
162 seen by Voyager 2 (color-composite uses orange, green and UV filters in the red, green and blue
163 colors; Schenk et al., 2021). 0°E, 90°E, 180°E, 270°E correspond to the sub-Neptune, leading,
164 anti-Neptune and trailing longitudes respectively.

165 In 1989, the Voyager 2 flyby of Triton revealed an amazing world with a geologically young (<100
166 Myr), diverse and active surface as suggested by the presence of plumes (evidence of resurfacing
167 processes), tectonic structures, and very few impact craters (Smith et al., 1989, Croft et al., 1995,
168 Stern and McKinnon, 2000, Schenk and Zahnle, 2007). Figure 2 shows a map of Triton as seen
169 by Voyager 2. Only ~60% of the surface has been imaged (including half of that at relatively high
170 resolution), as much of the northern hemisphere was hidden in the polar night. The northern and
171 southern hemispheres display different terrains in color, albedo, and texture, suggestive of distinct
172 compositions (Cruikshank et al., 1993, McEwen, 1990). Unfortunately, Voyager 2 lacked spectral
173 measurements in the near-infrared, and therefore the exact composition of the different regions
174 remains uncertain.

175 Triton is uniformly very bright, with a normal reflectance of the surface that varies between ~0.7
176 and ~1 (Hillier et al., 1994) and a Bond albedo of ~0.85 (Hillier et al., 1991), with a higher
177 reflectance in the southern hemisphere. Estimates of surface emissivities from Voyager 2 data
178 range from 0.3 to 0.8 (Hillier et al., 1991, Stansberry et al., 1996a ; see Section 3.4.1). The
179 Voyager 2 observations suggest that the southern hemisphere is covered by a bright cap of
180 volatile ice (likely N₂ mixed with CH₄ and CO, see Section 2.3), extending to the equator, whereas
181 the observed part of the northern hemisphere may be volatile-free (e.g., Stone and Miner, 1989;
182 Moore and Spencer, 1990). In the absence of spectral measurements, this is supported by the
183 observations of many local dark areas on the bright ice resembling sublimation patterns on Mars
184 (e.g. Mangold, 2011) and on Pluto (e.g. White et al., 2017, Howard et al., 2017) and by the volatile
185 ice longitudinal variability observed from Earth-based near-infrared spectroscopy (see Section
186 2.3). In this paper, we refer to this geologic terrain as the southern cap (it can include permanent
187 and seasonal volatile deposits), although we note that other types of terrains and ices may be
188 present at the surface in the southern hemisphere. We do not use the term “polar cap” since the

189 caps tend to extend outside the polar regions down to mid-latitudes and to the equator, but both
190 northern and southern caps mentioned in this paper are centered at the pole. In Voyager 2
191 images, the northern latitudes seem to be depleted in volatile ice, based on the albedo, geology
192 and texture of these terrains, and should therefore consist of Triton's exposed "bedrock" (CO₂
193 and/or H₂O). Alternatively, the northern hemisphere could be covered by a thin transparent slab
194 of N₂ ice, so that the albedo of the underlying bedrock is not significantly altered. This has been
195 suggested by Lee et al. (1992), who performed photometric analyses of Voyager 2 high-resolution
196 images and revealed unexpected scattering properties of the surface in the northern hemisphere.

197 Another region of interest is the blue and very bright equatorial fringe of frost seen between 325°E
198 and 30°E in the close encounter images (Smith et al., 1989, McEwen, 1990). A bluer surface is
199 interpreted as a younger, fresher surface where recent deposition of volatiles has occurred. This
200 is due to a shorter period of exposure to radiation and cosmic rays that tends to redden planetary
201 surfaces. More specifically, the blue (or less red) fringe seen by Voyager 2 has been interpreted
202 to be freshly deposited seasonal N₂ (e.g. Lunine and Stevenson, 1985; Zent 1989).

203 Photometric observations of Triton have been performed since the 1950s and revealed changes
204 in surface color with time, possibly due to seasonal volatile transport of N₂, CO and CH₄. In
205 particular, the surface became bluer (less red) between 1979 and the Voyager 2 flyby in 1989
206 (Smith et al., 1989; Buratti et al., 1994; Brown et al., 1995). Whether these bluer regions were
207 brought into view by changing viewing geometry or were created by deposition of volatiles on the
208 already visible hemisphere of Triton is unknown. Possible direct evidence for volatile transport
209 between the Voyager 2 flyby and 2005 was reported by Bauer et al. (2010). They used visible
210 images of Triton obtained with the Hubble Space Telescope (HST) in 2005 to construct visible
211 albedo maps and lightcurves to compare with Voyager 2's observations. Rotational and regional
212 changes in surface albedo were identified, with an overall brightening in the equatorial regions,
213 suggesting recent deposition there, and a darker anti-Neptune hemisphere. Photometry of Triton
214 for the 1992–2004 period found that the color of the surface was similar to that of the 1950–1974
215 period (Buratti et al., 1994, Buratti et al., 2011), thus suggesting that Triton reddened since 1989
216 (assuming it became bluer before 1989). This may be due to the plume activity occurring over the
217 southern cap which tends to redden the ice (wind streaks appear darker and redder than the
218 surrounding deposits, McEwen, 1990) and therefore the global color of Triton (the observed global
219 reddening of Triton's surface could not be linked to insolation changes, Buratti et al., 2011).

220 2.3 Earth-based surface spectroscopic observations

221 In addition to the Voyager data, several ground-based spectroscopic observations of Triton's
222 surface have been performed, leading to different scenarios for the surface distribution of the
223 volatile and non-volatile ices. The volatile ices N₂, CO, CH₄ and non-volatile CO₂ and H₂O ices
224 have been detected by Cruikshank et al. (1993, 2000), with the non-volatile ices forming Triton's
225 bedrock being at the estimated mean surface temperature of ~40-50 K (Broadfoot et al., 1989;
226 Gurrola, 1995). The surface temperature of N₂ ice was estimated to be 38 ± 1K in 1993 (Tryka et
227 al., 1994), and 37.5 ± 1K for the 2010–2013 epoch (Merlin et al., 2018). It was demonstrated that
228 CO and most of the CH₄ are diluted in N₂ ice with ice mixing ratios relative to N₂ of ~0.05%
229 (Cruikshank et al. 1993; Quirico et al. 1999; Grundy et al. 2010, Merlin et al., 2018), with a small
230 fraction of CH₄-rich ice being present elsewhere (Quirico et al., 1999, Merlin et al., 2018). Tegler
231 et al. (2019) also showed that CO and N₂ molecules on Triton are intimately mixed in the ice rather
232 than existing as separate regions.

233 During the 2002-2014 period, ground-based infrared (0.8 to 2.4µm) spectroscopic observations
234 performed using the SpeX instrument at NASA's Infrared Telescope Facility (IRTF) showed a
235 general increase in N₂ and CH₄ band absorption during this period (Holler et al., 2016). Recent
236 IRTF/SpeX results indicate that they are continuing to increase (Young, L. A., personal

237 communication). These trends can be indicative of volatile transport although the monotonic
238 increase in CH₄ absorption could be due to a change in viewing geometry only, if southern high
239 latitudes are deficient in CH₄.

240 Observations of Triton with IRTF/SpeX showed variability in spectral band depth suggesting
241 longitudinal variability of the ice distribution (Grundy and Young 2004, Grundy et al., 2010, Holler
242 et al., 2016). N₂ and CO spectra displayed a peak absorption at the same longitudes in the sub-
243 Neptune hemisphere, confirming that the two species form a molecular solution. This longitudinal
244 variability for N₂ and CO likely results from variations in surface ice coverage, although variations
245 in other physical parameters of the ice (e.g., particle size, vertical segregation, etc.) may also be
246 at work. There is a certain degree of consistency with the Voyager images showing a southern
247 cap (likely N₂ + diluted CO and CH₄) roughly extending to the equator on the sub-Neptune
248 hemisphere and ~30°S in the opposite hemisphere (Figure 2), which suggests that the
249 longitudinal variation of the spectrum has not changed much since the Voyager 2 flyby (more N₂
250 ice in the sub-Neptune hemisphere). However, the marked rotational variation of the N₂ and CO
251 spectra also suggests that the very southernmost latitudes are free of detectable N₂ and CO.

252 The same observations also showed longitudinal variability for CH₄, with an offset of 90°
253 compared to that of N₂ and CO. All the CH₄ bands (weak and strong) were observed in phase,
254 with a maximum absorption near 300°E, but the longitudinal variability decreased from weak to
255 strong CH₄ bands (Grundy et al., 2010, Merlin et al., 2018), suggesting localized regions around
256 300°E with CH₄-rich ice (and thus with larger optical path lengths in CH₄ and a spectral effect
257 most evident in the weakest CH₄ bands).

258 The CO₂ and H₂O spectra showed little longitudinal variability, which means that the equatorial
259 and low latitudes are either CO₂ and H₂O free, or have uniform longitudinal coverage of CO₂ and
260 H₂O. In the former case, it has been suggested that CO₂ and H₂O are exposed at the south pole
261 (roughly between 90°S-60°S), which would thus be devoid of volatile ice during the 2002-2014
262 period (Grundy et al., 2010, Holler et al., 2016). This scenario also has a certain degree of
263 consistency with the observed longitudinal variation of N₂ ice with IRTF/SpeX, whose amplitude
264 would be too shallow if N₂ ice was present at the south pole, according to the near-IR modeling
265 of Grundy et al. (2010). We discuss further this scenario in Section 8.

266 New near-IR observations performed with SINFONI on the Very Large Telescope (VLT) for the
267 2010-2013 period obtain similar variabilities for the band areas and support a spatial configuration
268 involving two main units: one dominated by N₂ (with diluted trace amounts of CO and CH₄), but
269 also including CO₂ ice as small grains, and the other dominated by H₂O and CO₂, but also
270 including a few percent of CH₄-rich ice (Merlin et al., 2018). Note that Merlin et al. (2018) did not
271 detect H₂O ice directly (the absorption bands are not seen entirely or are hidden by CH₄
272 absorption bands), but their model results remain consistent with little longitudinal variability for
273 H₂O and CO₂ ice.

274 The modeling of the near-IR disk integrated spectrum of Triton's surface also provided constraints
275 on the relative surface area (projected on the visible disk) covered or not covered by CH₄ ice
276 (including CH₄-rich or diluted in N₂ ice, so by extension, the method constrains the fractional area
277 volatile ice/non-volatile ice, e.g. Quirico et al. 1999, Merlin et al. 2018). For instance, Quirico et
278 al. (1999) found for 1995 a volatile/non-volatile fractional area of 55%/45% (see their table IV)
279 whereas Merlin et al. (2018) found for the 2010-2013 period a volatile/non-volatile fractional area
280 of 60-70%/30-40% (see their Table 9), although they note that these results remain model-
281 dependent. The coverage of CH₄-rich ice during this period is estimated to represent 2–3% of the
282 observed surface (i.e. the surface projected on the visible disk) and to be larger in the anti-
283 Neptune hemisphere, whereas Quirico et al. (1999) estimated a maximum of 10% for 1995.
284 However, the latitudinal distribution of these units remains uncertain.

285 2.4 Atmospheric surface pressure

286 Triton's atmosphere is mainly N₂ and is in solid-gas equilibrium with the surface N₂ ice (Tyler et
287 al., 1989). A comprehensive dataset of Triton's surface pressure is detailed in Marques Oliveira
288 et al. (2021) (see their Table 4, and their Section 5 and 6). On August 25, 1989, the Voyager 2
289 spacecraft flew by Triton and sent its radio signal (RSS experiment) back to Earth as it passed
290 behind Triton. The analysis of the phases and amplitudes of the recorded radio waves provided
291 the line-of-sight column density of the N₂ atmosphere, and an estimation of the surface pressure
292 of $\sim 1.4 \pm 0.2$ Pa (Broadfoot et al., 1989; Gurrola, 1995).

293 Different sets of ground-based stellar occultation observations were obtained in the following
294 years. Stellar occultations do not probe the same altitude as RSS, and the methods and
295 assumptions used to retrieve atmospheric pressure vary from one group to another.
296 Consequently, careful comparisons between stellar occultation observations must be made. The
297 first stellar occultation observations performed after Triton's flyby were interpreted as showing
298 that the atmospheric pressure doubled during the 1989–1997 period (Olkin et al., 1997, Elliot et
299 al., 1998). Olkin et al. (1997) derived a surface pressure of 1.7 ± 0.1 Pa for 1995, i.e. a 40%
300 increase since 1989, but at a low 1.8- σ significance level. Elliot et al. (2000) and Marques Oliveira
301 et al. (2021) derived a surface pressure of 2.68 ± 0.34 Pa and $2.28^{+5.4}_{-3.6}$ for the same event (but
302 using different analysis methods) in 1997 (July 18th), respectively, i.e. a 60-90% increase since
303 1989. It is possible that this dramatic increase in surface pressure is related to the sublimation of
304 the N₂ southern cap. However, in the analysis from Marques Oliveira et al. (2021), no increase
305 can be claimed between the 1989 and the 1995-1997 epochs at a 3- σ significance level. The 4
306 November 1997 value of Elliot et al. (2003) has a much lower error bar, and at face value does
307 indicate an increase of pressure by a factor 1.76 between 1989 and 1997 ($P_s = 2.11 \pm 0.02$ Pa).
308 This was a single-chord event but with a central flash (chord close to central). The 21 May 2008
309 event provided only two grazing chords, making it difficult to infer any change of pressure between
310 1989 and 2003. Finally, a stellar occultation by Triton was observed on 5 October 2017 and
311 provided 90 chords, 25 of them showing a central flash near the shadow center, from which a
312 surface pressure of 1.41 ± 0.04 Pa was derived (Marques Oliveira et al., 2021). This value for
313 2017 is similar to that measured during the Voyager 2 flyby, which suggests (although at a small
314 confidence level) a pressure maximum around years 2000-2010 and a recent decrease in
315 pressure related to N₂ ice deposition in the northern hemisphere or in the equatorial regions
316 (deposition at the South polar region is ruled out as it remained under continuous daylight). This
317 is also consistent with the N₂ ice temperature of 37.5 ± 1 K measured for the 2010–2013 epoch
318 from spectral analyses of the N₂ band shapes and positions (Merlin et al., 2018), which suggests
319 a $1.6^{+1.6}_{-0.7}$ Pa pressure for this period.

320 2.5 Atmospheric abundances of CO and CH₄

321 Triton's atmosphere contains traces of CO and CH₄. In 1989, the Ultraviolet Spectrometer (UVS)
322 on-board Voyager 2 measured a partial pressure of CH₄ of 2.45×10^{-4} Pa (2.45 nbar) from a solar
323 occultation (Herbert and Sandel, 1991, Strobel & Summers, 1995) and a surface pressure of ~ 1.4
324 Pa, which gives a CH₄ atmospheric volume mixing ratio of $\sim 0.03\%$ near the surface. This is the
325 only direct measurement of the CH₄ mixing ratio on Triton (since both surface pressure and CH₄
326 partial pressure were precisely measured at the same time).

327 Lellouch et al. (2010) reported in 2009 the first detection of CH₄ in the infrared (IR) and the first
328 ever detection of CO in Triton's atmosphere. They found that the partial pressure of CH₄ had
329 increased to $9.8 \pm 3.7 \times 10^{-4}$ Pa (fourfold increase compared to the 1989 value) and estimated the
330 partial pressure of CO to be about 2.4×10^{-3} Pa (24 nbar) with a factor 4 uncertainty. However,
331 they did not measure the surface pressure. If we assume a constant surface pressure of 1.4 Pa

332 for this period (resp. 1.8 Pa), these values correspond to an atmospheric volume mixing ratio for
333 CH₄ of ~0.08%-0.17% (resp. 0.06%-0.13%) and for CO of ~0.17% (resp. 0.13%). This
334 corresponds to a fourfold increase in CH₄ mixing ratio since 1989.

335 These values are higher than what was anticipated on the basis of Raoult equilibrium and an ideal
336 N₂-CH₄-CO mixture ((of the order of 10⁻⁵ %, Trafton et al., 1998). A first explanation for that calls
337 for the presence of relatively pure icy patches on Triton's surface (Stansberry et al., 1996b,
338 Lellouch et al. 2010) which have been indeed identified in small amount at the surface of Triton
339 by near-infrared observations (Quirico et al., 1999, Merlin et al., 2018). It has been demonstrated
340 that it is a plausible mechanism for CH₄ ice (Lellouch et al., 2010, Merlin et al., 2018; note that it
341 has clearly been observed on Pluto, e.g. Schmitt et al., 2017), but not for CO, which cannot
342 thermodynamically separate itself from N₂ (Prokhvatilov and Yantsevich, 1983, Vetter et al., 2007,
343 Tan and Kargel, 2018). A second explanation, which applies to CO, is that the seasonal volatile
344 cycles lead to the formation of enriched layers of CO on top of the surface according to the
345 "detailed balancing model" (Trafton, 1984, Lellouch et al., 2010). Note however that based on
346 recent (2017) mm-observations with ALMA, Gurwell et al. (2019) reported a ~100 ppm (~0.01%)
347 CO mixing ratio for an assumed 1.7 Pa atmosphere. This leads to a 1.7x10⁻⁴ Pa CO partial
348 pressure, sharply inconsistent (more than a factor 10 lower) with the IR-derived value from
349 Lellouch et al. (2010). These differences remain to be investigated and understood in more detail,
350 especially given the fact that IR and mm-observations of CO in Pluto's atmosphere give very
351 consistent results on the CO abundance (Lellouch et al. 2011, 2017).

352 2.6 Seasonal volatile transport: expectations and modeling

353 As described in the previous sections, several pre- and post-Voyager 2 datasets show changes
354 in Triton's surface albedo patterns, spectra, color and optical light curve that aren't completely
355 due to changes in viewing geometry, but instead could be due to volatile ice migration driven by
356 seasonal insolation changes. The last decades on Triton's southern hemisphere correspond to a
357 period of intense summer, with a subsolar point poleward of 40°S (Figure 1). Volatile sublimation
358 in the southern hemisphere is therefore expected and several observations support the fact that
359 the bright southern cap, usually presumed to be mostly made of N₂ ice, is currently sublimating
360 away. First, Voyager 2 images of the equatorial regions show local dark areas on the bright ice
361 (on the sub-Neptune hemisphere), which suggest that erosion due to sublimation of N₂ ice was
362 already significant in 1989, when the subsolar latitude was 46°S (Smith et al., 1989). Second,
363 spectral observations showed a tentative seasonal reduction (at 2-σ) in Triton's N₂ ice absorption
364 during the 2000-2009 period (Grundy et al., 2010). The longitudinal pattern of this decline is
365 consistent with a textural reduction in optical path length in N₂ ice, which suggests N₂ ice
366 sublimation but not a retreat of the N₂ ice southern cap (although this is not a unique interpretation,
367 as complex and poorly known microphysical processes are at play). Third, Triton's global color
368 has become redder during the 1992-2004 period, possibly due to plume activity and deposition of
369 dark reddish material over the southern cap, associated with the rapid sublimation of the cap that
370 also concentrates at the surface non-volatile particles included in the ice (McEwen, 1990, Buratti
371 et al., 2011).

372 Volatile transport models have been developed to investigate the seasonal variations in surface
373 ice distribution on Triton due to the migration of the subsolar point. Stansberry et al. (1990) and
374 Spencer (1990) (superseded by Moore & Spencer 1990, and again by Spencer and Moore 1992)
375 developed zonally-averaged models of the N₂ seasonal cycle and investigated how N₂ ice could
376 evolve and be transported. The former model assumed that N₂ ice is brighter than the underlying
377 bedrock while the latter assumed that fresh N₂ ice is relatively dark and gets brighter with time
378 and insolation, in a similar way than what has been observed on Mars (Paige 1985). However,
379 both models met limited success in reproducing the observed surface albedo. Most importantly,

380 they did not take into account heat conduction in the subsurface, which has a significant impact
381 on the behavior of the seasonal ice on Mars and on Pluto (Wood and Paige 1992, Bertrand and
382 Forget, 2016, Bertrand et al., 2018, 2019).

383 Hansen and Paige (1992) investigated both scenarios of bright and dark N₂ ice with a thermal
384 model of the N₂ cycle which included conduction in the subsurface. Their best agreement between
385 the model results and the available observations at that time was obtained with a relatively dark
386 or transparent frost. However, in light of the occultation observations in the 1990s and in 2017, it
387 seems that their scenario with a bright frost now gives a better agreement. They also found that
388 the southern cap is likely to be a large permanent deposit of N₂ ice, otherwise it could not have
389 been extended to the equator in 1989 as seen by Voyager 2. Brown and Kirk (1994) also
390 developed a volatile transport model for Triton, and coupled it with an internal heat flow. They
391 showed that an anisotropic internal heat flow could produce permanent caps of considerable
392 latitudinal extent. Other volatile transport modeling studies showed that a bright permanent N₂
393 cap (with a reduced N₂ ice reservoir) can also be produced and/or maintained by (a permanent
394 albedo difference between the northern (bedrock) and southern hemispheres (N₂ ice caps) which
395 affects the radiative balance (the “Koyaanismuuyaw” hypothesis, Moore and Spencer 1990,
396 Spencer and Moore, 1992), or by changes in radiative properties of N₂ ice as it goes through the
397 alpha-beta phase transition (this would not produce an asymmetry but would instead help
398 maintain one, Eluszkiewicz, 1991, Duxbury and Brown, 1993, Tryka et al, 1993).

399 A difference in bedrock topography could also trigger an asymmetry between northern and
400 southern N₂ deposits. On Pluto, N₂ ice tends to accumulate and be more stable in topographic
401 basins, where the surface pressure and therefore the equilibrium ice temperature is higher. This
402 is because the warmer N₂ ice deposits at lower altitudes radiate more heat to space, which is
403 balanced by latent heat of sublimation through increased N₂ deposition rates in order to maintain
404 local conservation of energy, vapor-pressure equilibrium, and hydrostatic equilibrium (Trafton et
405 al. 1998, Trafton & Stansberry 2015, Bertrand & Forget 2016, Bertrand et al. 2018, 2019, and
406 Young et al 2017). This atmospheric-topographic process could also apply to Triton, although the
407 surface (at least the portion imaged by Voyager 2) seems to be much flatter than Pluto’s (Schenk
408 et al., 2021).

409 In addition to the volatile cycles, Triton's surface activity may be (globally or locally) impacted by
410 the formation of active geysers, such as those observed at the south pole by Voyager 2. Such
411 processes could act to darken the ice, increase the ice sublimation rates, and thus affect volatile
412 transport. The formation of complex chemical molecules (whose spectral properties in the visible
413 range are fairly reproduced by tholin materials formed in the laboratory, Materese et al., 2015,
414 Auge et al., 2016, Jovanovic et al., 2020), through volatile photochemistry occurring in the
415 atmosphere (Krasnopolsky and Cruikshank, 1999), or through direct volatile irradiation at the
416 surface (Moore and Hudson, 2003), could play a similar role at a more global scale.

417 Finally, complex evolution of N₂:CO:CH₄ mixtures that result in compositional stratification and
418 formation of a bright lag deposit of CH₄ can occur on Triton, in particular where the N₂ sublimation
419 is more intense (Grundy and Fink, 1991, Cruikshank et al, 1991, Quirico et al., 1999). For
420 instance, on Pluto, the northern edge of the N₂ ice sheet Sputnik Planitia is enriched in CH₄ due
421 to intense N₂ sublimation at these latitudes (Protopapa et al., 2017, Schmitt et al., 2017, Bertrand
422 et al., 2018). This could affect the ice and atmospheric mixing ratio of the volatile species.

423 2.7 Reservoirs of volatile ice and internal heat flow

424 Triton's orbital elements likely indicate that it is a captured Trans-neptunian Object (e.g., McCord,
425 1966; McKinnon, 1984; Agnor and Hamilton, 2006, Li et al., 2020), sharing a common volatile
426 origin as the Kuiper Belt Objects (Johnson et al. 2015). Tidal interactions associated with its

427 capture and subsequent circularization around Neptune should have heated its interior
428 significantly (McKinnon et al., 1995, Correia, 2009; Nogueira et al., 2011). Remnant heat
429 stemming from these interactions may have persisted to the present day, as suggested by recent
430 studies showing that the heat flow on Triton should be around 10-100 mW m⁻² (Ruiz, 2003, Martin-
431 Herrero et al., 2018). These values are much larger than those obtained by assuming only
432 radiogenic production and tidal dissipation for fixed orbital eccentricities (2-4 mW m⁻², Gaeman et
433 al. 2012, Brown et al. 1991, Hussmann et al. 2006). The large heat flow could also be produced
434 by internal ocean tidal heating due to Triton's orbit obliquity (Chen et al., 2014; Nimmo and
435 Spencer, 2015; Dubois et al., 2017).

436 3. The Triton Volatile Transport Model: description and simulation 437 settings

438 3.1 Model description: the Pluto VTM legacy

439 We use the latest version of the Triton volatile transport model (VTM) of the Laboratoire de
440 Météorologie Dynamique (LMD). The Triton VTM is a 2D surface thermal model derived from the
441 LMD Pluto VTM, taking into account the volatile cycles of N₂, CH₄, and CO (insolation, surface
442 thermal balance, condensation-sublimation, Bertrand and Forget, 2016), a glacial flow scheme
443 for N₂ ice (Bertrand et al., 2018; based on the equations presented in Umurhan et al., 2017), and
444 the seasonal variation of the subsolar point specific to Triton. The calculations of this complex
445 variation is detailed in the Appendix.

446 As in the Pluto VTM, we consider that Triton's atmosphere is very thin, almost transparent and
447 thus has a negligible influence on the surface thermal balance aside from the condensation,
448 sublimation and exchanges of latent heat with the surface (this is even more true than for Pluto,
449 given the 10x lower CH₄ abundance, and more tenuous haze). We parametrize the atmospheric
450 transport using a simple global mixing function for N₂, CH₄, and CO in place of 3D atmospheric
451 transport and dynamics, with a characteristic time τ for the redistribution of the surface pressure
452 and trace species, based on reference 3D global climate model simulations of Triton. Tests done
453 with the 3D model determined the timescales for atmospheric transport of CH₄ (10⁷ s, i.e., about
454 4 Earth months), N₂ (1 s, instantaneous mixing) and CO (1 s; CO is well mixed in the atmosphere
455 in 3D global climate model simulations) used in the VTM (the same values were used on Pluto,
456 Bertrand et al., 2019). The topography in the model is controlled by the amount of volatile ice on
457 the surface, but we use a flat topography for the non-volatile bedrock.

458 3.2 General simulation settings and paleoclimate algorithm

459 The simulations of this paper are performed on a horizontal grid of 32×24 points, which
460 corresponds to a grid-point spacing of 11.25° in longitude and 7.5° in latitude (about 270 km and
461 180 km at the equator, respectively). We use 96 timesteps per Triton day. At each time step the
462 local solar insolation is calculated taking into account the variation of the subsolar point, the
463 distance Triton-Sun, and the diurnal cycle. In Sections 5 and 7, we perform simulations over
464 several million years (Myrs) using the paleoclimate and ice equilibration algorithm described in
465 detail in Bertrand et al. (2018):

466 Typically, the model is first run over ~4,000 Earth years to capture several seasonal cycles of
467 Triton so that the ice distribution and surface pressure reach an equilibrium. We consider that the
468 first ~2,000 Earth years correspond to a spin up time and we use the last seasonal cycles covering
469 ~2,000 Earth years to estimate the mean sublimation-condensation rates over that period (which
470 is also largely enough to capture several seasonal cycles). These mean sublimation-condensation

471 rates are used to calculate the new amounts of ice over a paleo-timestep of $\Delta t=20,000$ Earth
 472 years, and finally the topography is updated according to the new amounts of volatile ice. These
 473 steps are repeated so that the simulation covers at least 2 Myrs, which is enough for large and
 474 small N_2 ice reservoirs, glacial flow, and surface and subsurface temperatures to reach a steady
 475 state insensitive to the initial state. Consequently, in this paper, the distribution of surface ices
 476 and subsurface temperatures of all the simulations (unless stated otherwise) are the outcome of
 477 several Myrs of evolution.

478 Note that here we neglect any change over time in obliquity (with respect to Triton's orbit around
 479 Neptune) and orbital parameters, which is valid over the relatively short timescales of a few Myrs
 480 (the obliquity of Neptune is suggested to be primordial, Laskar and Robutel, 1993).

481 Also note that the numerical model only applies to global atmospheres (we neglect the effects of
 482 local atmospheres). For Pluto, the approximate limit at which point the atmosphere is non-global
 483 is 0.006 Pa (Johnson et al., 2021, Spencer et al., 1997). For Triton, the rescaled threshold is
 484 0.009 Pa (owing to the larger size and gravity constant). In this paper, most of our simulations do
 485 not reach that threshold. A few of them do, but over an extremely short range of time, and
 486 therefore we do not expect this process to impact the results significantly (it involves very slow
 487 sublimation and condensation rates).

488

489 3.3 Hypothesis and initial state of the different simulation cases

490

Section	Simulation type	Initial State	Model parameters
4	Bedrock surface thermal balance only Several seasonal cycles (~10 000 Earth years)	Bedrock only, no volatile ice	Fixed: $A_{bed}=0.6$, $\epsilon_{bed}=0.8$ Variable: $TI=500-2000$ SI, $HF = 0-30$ mW m ⁻²
5	Full volatile transport Long term (~7 Myrs) with viscous flow North-South asymmetries in heat flux (HF), topography (TP) and N_2 ice albedo (A_{N_2})	Global and uniform cover of 300 m of N_2 ice	Fixed: $A_{bed}=0.7$, $\epsilon_{bed}=0.8$, $A_{N_2}=0.7$, $\epsilon_{N_2}=0.8$ Asymmetry HF: $\Delta F=5-45$ mW m ⁻² , $TI=1000$ SI Asymmetry TP: $\Delta h=2-8$ km, $TI=500-2000$ SI Asymmetry A: $\Delta A_{N_2}=0.04-0.1$, $TI=500-2000$ SI
6	Volatile transport limited to fixed N_2 reservoirs Different polar cap extensions Several seasonal cycles (~10 000 Earth years) Including current seasonal cycle (1900-2100)	Fixed and infinite N_2 reservoirs (no glacial flow, flat topography) N_2 albedo adjusted by model	Fixed: $\epsilon_{N_2}=0.8$ Variable: $TI=500-2000$ SI S. PC size: 90°S-30°S, 90°S-0°, 80°S-0° N. PC size: No cap, 90°-75°N, 60°N, 45°N
7	Full volatile transport Long term with viscous flow Including current seasonal cycle (1900-2100) North-South asymmetries in N_2 ice albedo	N_2 ice initially confined to the south pole (90°S-50°S) Northern hemisphere initially volatile-free and warm ($T\sim 100$ K) N_2 albedo adjusted by model	Fixed: $\epsilon_{bed}=0.8$, $\epsilon_{N_2}=0.8$, $TI_{N_2}=1000$ SI Variable: $A_{bed}=0.1-0.9$, $TI_{bed}=100-2000$ SI, $\Delta F=0-30$ mW m ⁻² , $R_{N_2}=0.3-650$ m Asymmetry in N_2 ice albedo: $\Delta A_{N_2} = 0-0.1$

491

492 Table 1: Summary of the simulation types, initial states and parameters presented in this paper
 493 (see text): albedo (A), emissivity (ϵ), seasonal thermal inertia (TI) in $J s^{-0.5} m^{-2} K^{-1}$ (SI), internal
 494 heat flux (HF), topography (TP), pole-to-pole internal flux, topography gradient and N_2 albedo
 495 difference (ΔF , Δh , ΔA_{N_2}). S. and N. PC are the southern and northern polar caps.

496 In this paper, we postulate that the bright terrains observed by Voyager 2 in the southern
 497 hemisphere correspond to a N_2 ice southern cap (mixed with CH_4 and CO ices), based on Voyager

498 images and Earth-based spectroscopic observations. As described in Section 2.3, some Earth-
499 based spectroscopic observations suggest that N₂ is not exposed or not detectable at the very
500 southernmost latitudes (i.e. the south pole, Grundy & Young 2004, Grundy et al. 2010, Holler et
501 al. 2016). Note that this does not necessarily means that N₂ ice is not present at the south pole
502 (see further discussions on this topic in section 8.3). In general, we leave the model calculate the
503 surface distribution, but we also added simulation cases in which we force the south pole to be
504 depleted in N₂ ice.

505 Since 1989, the southern cap has been under constant illumination and is likely dominated by N₂
506 ice sublimation. Under these conditions, the evolution of surface pressure depends on the N₂
507 condensation in the northern polar night. Table 1 summarizes the different simulations performed
508 in this paper.

509 In Section 4, we run the subsurface and surface thermal balance model without volatile ice in
510 order to estimate the mean surface temperatures of the bedrock, for different values of the thermal
511 inertia and internal heat flow. The bedrock albedo is fixed to 0.6. Note that throughout this paper,
512 the “albedo” in the VTM refers to a Bond albedo.

513 In Section 5, we run long term simulations of the N₂ cycle to explore how North-South asymmetries
514 in internal heat flux, surface N₂ ice albedo and topography lead to asymmetries in the northern
515 and southern cap extents. All simulations start with a global and uniform cover of 300 m of N₂ ice.

516 In Section 6, we run the model over the last seasonal cycles with artificially-prescribed fixed N₂
517 ice distributions in the northern and southern hemispheres. We use a flat topography, no glacial
518 flow, and volatile transport is limited to these artificially-prescribed N₂-covered regions (no
519 formation of seasonal frost outside these regions). We analyze the evolution of the surface
520 pressure that results from these specific latitudinal distributions of N₂ ice and compare to
521 observations.

522 In Section 7, we simulate the full volatile transport over the last 4 Myrs, exploring a large range of
523 parameters (bedrock albedo, thermal inertia, N₂ ice reservoir, internal heat flux, and North-South
524 asymmetry). In these simulations, the ice is initially placed southward of 50°S and the northern
525 hemisphere is warm and volatile-free with its surface and subsurface temperatures initialized to
526 an extremal value of 100 K. This is to demonstrate that the end state of the simulation and any
527 formation of a northern (polar) cap is independent of the initial ice distribution and surface and
528 subsurface temperatures (see discussions in Section 5 and Section 7). The bedrock topography
529 is flat, so the surface topography is equal to the thickness of N₂ ice lying on top.

530 Note that in Section 5, Section 6, and Section 7, the N₂ ice albedo in the simulations is not a free
531 model parameter but instead is constrained by the 1989’s surface pressure: it is automatically
532 adjusted by the model during the first seasonal cycles of the simulation (spin-up time) so that the
533 calculated surface pressure converges toward ~1.4 Pa in 1989, as observed by Voyager 2 (see
534 Section 3.4.1).

535 3.4 Surface properties

536 3.4.1. Albedos and emissivities

537 As on Pluto, the nitrogen cycle on Triton is very sensitive to the nitrogen ice Bond albedo A_{N_2} and
538 emissivity ϵ_{N_2} . The local energy balance on a N₂-covered surface on Triton can be written, to first
539 order (assuming a spatially uniform and isothermal ice with a flat topography, an efficient global
540 transport of N₂, and neglecting thermal inertia and latent heat exchanges) by the classical
541 equation $\epsilon_{N_2}\sigma T^4 \approx (1 - A_{N_2}) F/4$, where F is the solar constant at Triton, σ is the Stefan-Boltzmann
542 constant, and the factor $1/4$ comes from global averaging. As a result, the N₂ ice equilibrium
543 temperature and therefore the N₂ surface pressure, depend on $(1 - A_{N_2})/\epsilon_{N_2}$ (Spencer, 1990). On

544 Pluto, the surface pressure dataset inferred from stellar occultations give a strong constraint on
545 the combination of A_{N_2} and ϵ_{N_2} ; only a small range for these parameters allows for a satisfactory
546 match to the observations (Bertrand et al., 2016, Meza et al., 2018, Johnson et al., 2020). In this
547 paper, we intend to apply this study to Triton. We assume a fixed and relatively high emissivity of
548 $\epsilon_{N_2}=0.8$, as in the Pluto VTM (it would correspond to large cm-sized N_2 ice grains, Stansberry et
549 al., 1996a). This value is consistent with the values estimated for Triton from Voyager 2 data (0.7
550 $< \epsilon_{N_2} < 0.77$, Stansberry et al., 1992), and remains within 10% of the upper value estimated on
551 Pluto from a surface energy balance model ($0.47 < \epsilon_{N_2} < 0.72$, Lewis et al., 2021). However, we
552 note that Hillier et al. (1991) derived a lower surface emissivity of 0.46 ± 0.16 , which could be
553 consistent with smaller grain sizes of ~ 1 mm (Stansberry et al., 1996a). Consequently, in Section
554 7.3.2, we briefly explore the model sensitivity to lower emissivities than 0.8 (fixed $\epsilon_{N_2}=0.3$ and
555 $\epsilon_{N_2}=0.5$). In addition, since the emissivity of N_2 ice is also thought to vary with the ice temperature,
556 being lower in its α -phase than that in its β -phase (Stansberry and Yelle, 1999; Lellouch et al.,
557 2011b), we also explore the case of a temperature dependent emissivity.

558

559 For practical reasons, A_{N_2} is automatically calculated by the model so that the surface pressure
560 is close to 1.4 Pa in 1989, as measured by Voyager 2 (tuning manually A_{N_2} would be extremely
561 expensive in time and computing resources). In all simulations of this paper, A_{N_2} is initially fixed
562 to 0.75, and then the model increments or decrements A_{N_2} by steps of 0.005 during each extreme
563 southern summer (at subsolar latitude $45^\circ S$ corresponding to that of Voyager 2's flyby) so that
564 the surface pressure converges towards 1.4 Pa at this season. Typically, it takes less than 10,000
565 Earth years for A_{N_2} to reach a stable value in the model and thus for the pressure cycle to be
566 consistent with the observed surface pressure in 1989. Since all our simulations of the present-day
567 Triton climate are the results of Myrs of simulations, this means that the convergence occurs
568 quickly at the beginning of the simulations (spin-up time) We ensured that our model results are
569 not sensitive to the initial N_2 ice albedo value and that all our simulations reach a steady state for
570 A_{N_2} and surface pressure. By contrast, the albedo of the bedrock A_{bed} is a free parameter of the
571 model and we tested the sensitivity of the results to several values ranging from 0.1 to 0.9.

572 3.4.2. Thermal inertia (TI)

573 We assume a high seasonal thermal inertia in the sub-surface for N_2 ice, fixed to $800 \text{ J s}^{-1/2} \text{ m}^{-2}$
574 K^{-1} (or SI) as has been suggested on Pluto (Bertrand et al., 2016, Johnson et al., 2020). A high
575 thermal inertia was also inferred by Spencer and Moore (1992), and, in retrospect, their high
576 thermal inertia models are more in agreement with the later observed pressure evolution. Note
577 that to first order, this parameter does not significantly impact the N_2 cycle (see Section 2.2 in
578 Bertrand et al., 2018). The diurnal thermal inertia (for all ices) is set to 20 SI by analogy to Pluto
579 (Lellouch et al. 2011, 2016). Note that Pluto has large areas covered by tholins-like dark materials,
580 which are expected to have low diurnal thermal inertias as they form very porous layers of very
581 small grains. They may have played a significant role in the retrieval of thermal inertia values on
582 Pluto (the lightcurves are mostly sensitive to the thermal inertia of the tholins), so the values on
583 Triton could be higher. More thermal observations of Triton's surface are needed to constrain this
584 parameter. For the bedrock (assumed to be water ice or CO_2 ice, but here in this paper it is only
585 characterized by its albedo, emissivity and thermal inertia), we explored the sensitivity of the VTM
586 results to low and high values of seasonal thermal inertia ranging from 200 to 2000 SI.

587 The thermal skin depth is defined as $\delta = \text{TI}/C \times \sqrt{P/\pi}$ with TI the thermal inertia, C the ground
588 volumetric specific heat (assumed to be $10^6 \text{ J m}^{-3} \text{ K}^{-1}$) and P the period (s) of the thermal wave.
589 With this definition, the diurnal skin depth for 20 SI of ~ 8 mm and a seasonal skin depth for 200
590 SI and 2000 SI of ~ 8 m and 80 m respectively. As in the Pluto VTM, the subsurface is divided into
591 24 discrete layers, with a geometrically stretched distribution of layers with higher resolution near

592 the surface to capture the short period diurnal thermal waves (the depth of the first layer is $z_1 =$
593 1.4×10^{-4} m) and a coarser grid for deeper layers and long seasonal thermal waves (the deepest
594 layer depth is near 1000 m). Note that when a N_2 ice deposit (e.g., 300 m thick) is present at the
595 surface, we assume a subsurface seasonal thermal inertia of 800 SI in the subsurface levels that
596 correspond to the thickness of the deposits (e.g., down to 300 m) and then the seasonal thermal
597 inertia of the bedrock down to the deepest level.

598 3.4.3. N_2 ice reservoir and internal heat flux

599 Previous volatile transport modeling on Triton only used low N_2 ice reservoirs ($R_{N_2} = 0.2-2$ m,
600 Moore and Spencer, 1990, Hansen and Paige, 1992, Spencer and Moore, 1992) and thus were
601 limited to the simulation of seasonal frost. Spencer and Moore (1992) also tested simulations in
602 which a permanent southern cap is artificially and indefinitely maintained to a large size, with the
603 aim of reproducing to first order the effect of large reservoir and viscous spreading of N_2 ice from
604 the pole to the equatorial regions. In retrospect, these simulation cases (e.g. case “L” in Spencer
605 and Moore, 1992) are in relatively better agreement with the later observed pressure evolution.
606 Here, on the basis of these results, we used different N_2 ice reservoirs R_{N_2} ranging from 1 m to
607 650 m in global surface coverage, thus exploring both small and large reservoirs. With large N_2
608 ice reservoirs, the model is able to self-consistently simulate the formation of thick perennial
609 deposits and their viscous flow.

610 At the deepest subsurface level of the model, there may be a positive heat flow, which is balanced
611 by upward thermal conduction from a negative thermal gradient ($-k \, dT/dz$) as in Bertrand et al.
612 (2018, 2019). The reference simulations are performed assuming no internal heat flux, but we
613 also explored the effect of assuming an internal heat flux of 30 mW m^{-2} .

614 3.4.4. Assumptions on the state of N_2 and CH_4 ice in the model

615 N_2 , CH_4 , and CO ices easily mix together and are not expected to exist in perfectly pure states on
616 Triton. Instead, they should form non-ideal solid solutions whose phases follow ternary phase
617 equilibria (Trafton, 2015; Tan and Kargel, 2018). Complex mixtures have been revealed on Pluto’s
618 surface by the analyses of New Horizons observations, with $N_2:CH_4$ (N_2 -rich mixtures, e.g.,
619 Sputnik Planitia) and $CH_4:N_2$ (CH_4 -rich mixtures, e.g., the north pole) solid solutions involving
620 different molecular mixing ratios (Grundy et al., 2016; Protopapa et al., 2017; Schmitt et al., 2017).
621 Observations also suggest mixtures of both N_2 -rich + CH_4 -rich ice phases at some locations,
622 although the exact ‘organization’ (i.e. intimately mixed and/or vertically stratified) of these deposits
623 remains uncertain (Protopapa et al., 2017; Schmitt et al., 2017).

624 We note that sophisticated equations of state exist for the N_2-CH_4 and N_2-CH_4-CO systems
625 under surface conditions (surface pressure and temperature) similar to that of Triton
626 (CRYOCHEM, Tan and Kargel, 2018). Although these ternary and binary systems, when applied
627 to Pluto, give results relatively consistent with the diversity of phases seen on Pluto’s surface, it
628 remains unclear how they would apply to the case of Triton. In fact, on Triton, despite a surface
629 pressure and temperatures similar to that of Pluto, the observed mole fraction of CH_4 in N_2 -rich
630 ice is $\sim 0.05-0.11\%$ (Quirico et al., 1999, Merlin et al., 2018), which is 5-10 times less than on Pluto
631 (Douté et al. 1999; Merlin, 2015). In addition, the mechanisms controlling the formation and
632 evolution of such mixtures remain largely unknown.

633 In this context, and given a certain lack of data on the ice mixtures on Triton, the model presented
634 in this paper is rather simple and sticks to the available observations. As in previous VTM studies
635 (Bertrand and Forget, 2016, Bertrand et al., 2018, 2019, 2020a), for simplicity in coding with a
636 VTM, the model does not compute any evolution of ice mixing ratio and adopts Raoult’s law to
637 describe the solid-gas equilibria. In the simulations, the surface is either volatile-free, covered by

638 pure CH₄ ice or by N₂:CH₄ ice. When both CH₄ and N₂ ices are present on the surface, we assume
639 that CH₄ is diluted in a solid solution N₂:CH₄ with 0.05% of CH₄, as retrieved from the last
640 telescopic observations (Merlin et al., 2018), but we also explored the addition of small areas of
641 CH₄-rich ice (see Section 7.4.2). For CO concentration, we used 0.04% (close to the 0.05%
642 reported by Quirico et al., 1999) and also explored 0.08% to bracket the values 0.04-0.08%
643 suggested by Merlin et al., 2018 (see Section 7.4.1). The modeled N₂:CH₄ ice sublimates by
644 conserving the 0.05% of diluted CH₄. We make the approximation that CH₄-rich ice behaves
645 almost like pure CH₄ ice (Tan and Kargel, 2018), in terms of temperature and vapor pressure at
646 saturation of CH₄, as CH₄-rich ice can contain only up to 3% N₂ around 40K (Prokhvatilov and
647 Yantsevich 1983). It can form after sublimation of N₂ ice (in which CH₄ was trapped before) or
648 directly on a volatile-free surface. In the next sections of this paper, we refer to this phase as CH₄
649 ice. The formation and evolution of other types of binary or ternary phases is out of the scope of
650 this paper, and we neglect their effect in the model (although we acknowledge that it could lead
651 to some unevaluated uncertainties in N₂-rich and CH₄ solid-phase stability).

652 3.5 Observational constraints for the definition of best-case simulations

653 As detailed in Section 3.4.1, the simulations are constrained by one unique observation: the
654 surface pressure of ~1.4 Pa in 1989. The N₂ ice albedo is automatically adjusted by the model
655 during the spin up time to match this constraint.

656 The other available observational constraints, presented in this section, are not explicitly included
657 in the numerical calculations but are considered when interpreting the simulation results and when
658 looking for the best-case simulations. We search for simulations including (1) an ice distribution
659 consistent with Voyager 2 observations and ground-based near-infrared hemispheric spectra (the
660 relative surface area of volatile vs. non-volatile ice), and (2) an evolution of surface pressure
661 consistent with that retrieved from stellar occultations.

662 3.5.1. Constraints from the ground-based near-IR spectroscopy

663 As detailed in Section 2.3, near-IR ground-based spectroscopy of Triton's surface provides a
664 relatively good constraint on the relative surface area (projected on the visible disk) covered or
665 not covered by volatile ice. Based on the results from Quirico et al. 1999 and Merlin et al. 2018
666 for 1995 and 2010-2013, respectively, we assume with some margin that the volatile/non-volatile
667 fractional area is 45-65%/35-55% in 1995 and 55-75%/25-45% in 2010. To take these constraints
668 into account, we used the calculation in the appendix of Holler et al. (2016) to project our VTM-
669 modeled surface on the visible disk at the time of observation (subsolar latitude 49°S and 46°S
670 for 1995 and 2010, respectively). Note, that, in 2010, 60-70% of the disk-projected surface
671 covered by N₂ would correspond to a southern cap extending from 90°S to ~20°S, or 80°S to
672 ~15°S, or 60°S to ~0°.

673 3.5.2. Constraints from Voyager 2 images and infrared surface emission measurements

674 Based on the Voyager 2 images, we assume that the bright southern cap is made of N₂-rich ice,
675 and that its northern edge extends to 30°S-0° in 1989. Note that the volatile/non-volatile fractional
676 area derived from near-IR surface spectroscopy, detailed in Section 3.5.1, is a stronger constraint
677 and is given more weight when interpreting the results because it is a more direct observation
678 (Voyager 2 did not carry any IR spectrometer). We do not make any assumption regarding
679 whether the southernmost latitudes are covered by N₂-rich ice or not. Our model self-consistently
680 calculates the surface ice distribution and we consider that the best-case simulations should have
681 a N₂-rich southern cap (with or without N₂-rich ice at the very pole) with a northern edge extending
682 to 30°S-0° in 1989. In practice, as shown in Section 5 and Section 7, the south pole is always the
683 most efficient cold trap for N₂ ice in seasonal average and all our simulations present a perennial

684 N₂-rich deposit at the south pole (except in the cases where N₂ is artificially removed from the
685 south pole). This point is further discussed in Section 8.3.

686 We assume that the northern (polar) cap, if it exists, was in winter night and therefore not seen
687 by Voyager 2 in 1989, implying that it did not extend to latitudes southward of 45°N. Based on the
688 analysis of Voyager 2 images (McEwen, 1990), we also assume that the albedo of all terrains is
689 higher than 0.6.

690 The Infrared Interferometer Spectrometer (IRIS) instrument on-board Voyager 2 measured the
691 infrared radiation emitted by Triton's surface. The spectra were relatively noisy and the surface
692 emission was mostly detected at the longest wavelengths of the IRIS spectral range (i.e., ~40-50
693 μm). From these measurements, Conrath et al. (1989) and Stansberry et al. (2015) derived a full-
694 disk averaged surface temperature of Triton in 1989 ranging from 37-44 K, depending on the
695 emissivity of the different surface units. We use this range of surface temperature to constrain the
696 best-case simulations. In fact, most simulations satisfying the previous albedo constraint of > 0.6
697 fall in this range.

698 3.5.3. Constraints from the surface pressure from Voyager 2 and stellar occultations

699 Section 2.4 summarizes the different observations that provide estimates of Triton's surface
700 pressure. Table 2 gives the surface pressure data points used in this paper. Based on the analysis
701 of an extremely high-quality occultation dataset from 2017, and the re-analysis of earlier
702 occultation curves, Marques Oliveira et al. (2021) conclude that the increase in surface pressure
703 reported in 1995-1997 (compared to the Voyager 2 value in 1989) remains elusive (as the data
704 are not available for reanalysis using an approach consistent with theirs), but that the 2017 value
705 has been obtained at a high significance level and is fully compatible with that measured by the
706 Voyager 2 RSS experiment.

707 Consequently, in this paper, we consider the values reanalyzed by Marques Oliveira et al. (2021)
708 as the strongest observational constraints of surface pressure for our volatile transport
709 simulations, but we will also assess if the model can predict an increase in surface pressure
710 maximum in the 1990s, as suggested by the other values. We also note that the 2017 event and
711 the Voyager pressure are the best quality datasets among the analyzed events.

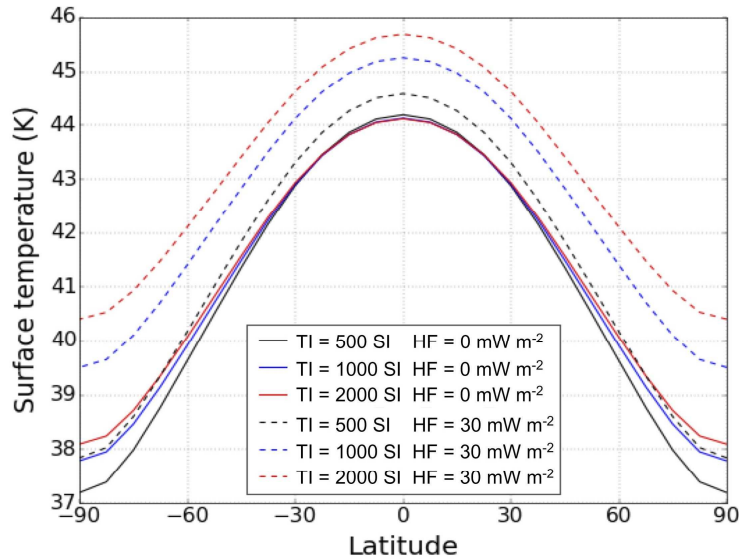
712

Date	Surf. Pressure (Pa)	Reference
25 Aug. 1989	1.4 ± 0.2	Gurrola et al., 1995
14 Aug. 1995	1.7 ± 0.1	Olkin et al., 1997
18 Jul. 1997	$2.28^{+0.54}_{-0.36}$ 2.68 ± 0.34	Marques Oliveira et al., 2021 Elliot et al., 2000
4 Nov. 1997	2.11 ± 0.02	Elliot et al., 2003
21 May 2008	$1.38^{+1.24}_{-0.44}$	Marques Oliveira et al., 2021
5 Oct. 2017	1.41 ± 0.04	Marques Oliveira et al., 2021

713

714 Table 2: Surface pressures on Triton derived from different observations and detailed in Marques
715 Oliveira et al. (2021).

716 4. Bedrock surface temperatures on Triton



717
 718 Figure 3: Zonal mean surface temperatures of the bedrock of Triton (assumed to be water ice, no
 719 volatile ice) averaged over several seasonal cycles (~10,000 Earth years), with subsurface
 720 thermal inertias within 500-2000 SI and internal heat fluxes 0 and 30 mW m⁻². The bedrock albedo
 721 is fixed to 0.6 and its emissivity to 0.8.

722
 723 On average over one or several seasonal cycles the poles on Triton receive less insolation flux
 724 than the equator. As a result, the poles are colder than the equatorial regions, as shown by Figure
 725 3. High subsurface thermal inertia allows the subsurface to store more heat accumulated during
 726 extreme summer and release it during winter, thus dampening and delaying the response of the
 727 surface temperatures to insolation (Spencer, 1989) and raising the mean temperatures (the poles
 728 are ~1 K warmer with high thermal inertia than with low thermal inertia, on average). While on
 729 Pluto, high subsurface thermal inertia allows the poles to be as warm or warmer than the equator
 730 on annual or multi-annual average (see Fig. 3 and 4 in Bertrand et al., 2018), on Triton, the poles
 731 remain colder than the equator by 5-6 K on average because they receive much less flux (~0.25
 732 W m⁻²) than the equator (~0.44 W m⁻²) on average over several seasonal cycles (the subsolar
 733 point never reaches high enough latitudes to make the poles warmer than the equator on average,
 734 and extreme summers are not occurring every seasonal cycle). For a subsurface (i.e., H₂O ice)
 735 TI of 1000 SI, a bedrock surface albedo of 0.6 and no internal flux, maximum and minimum
 736 bedrock surface temperatures are respectively ~49 K and ~33 K at the poles (during extreme
 737 seasons) and respectively ~45 K and ~43 K at the equator.

738 Volatile ice would therefore accumulate at the poles on Triton, and form a cold trap. Due to the
 739 very low eccentricity of Neptune's orbit and the circular orbit of Triton around Neptune, the
 740 northern and southern latitudes of Triton undergo the same seasons over several seasonal cycles
 741 (with the same insolation and heliocentric distances). Figure 3 shows that both poles on Triton
 742 are symmetric in terms of insolation and surface temperatures, on average over several seasonal
 743 cycles. Under these conditions, the volatile transport model would simulate the formation of
 744 symmetric southern and northern caps if all ice and surface properties were constant and uniform.

745 However, in reality, it is likely that one cap “wins” over the other (see Section 5). For instance,
 746 Figure 3 shows that an internal heat flux of 30 mW m^{-2} would raise the bedrock surface
 747 temperatures by up to $\sim 2 \text{ K}$ (for high subsurface thermal inertias), and could locally prevent N_2
 748 condensation at the locations where such a flux reaches the surface.

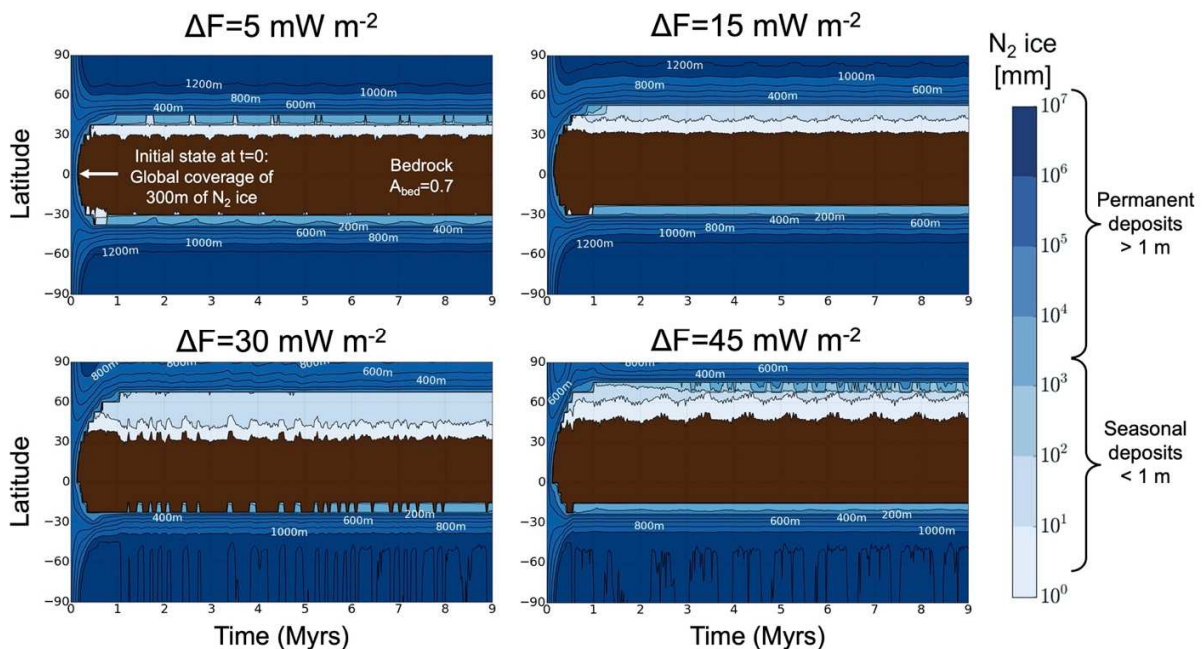
749 5. Long-term VTM simulation of the N_2 cycle with North-South 750 asymmetries

751 As discussed in Section 2.6, the Voyager 2 observations suggest that a southern cap (presumably
 752 made of N_2 ice) extends to the equator. It is not clear whether a north (polar) cap exists on Triton,
 753 as Voyager 2 did not detect it outside the polar night (southward of 45°N) in 1989. If it does exist,
 754 it must therefore be smaller than the southern cap. In Section 2.6, we listed several mechanisms
 755 that have been proposed to explain this asymmetry between the northern and southern caps,
 756 including the asymmetry in internal heat flux and in surface ice albedo, explored in detail by Brown
 757 and Kirk (1994) and Moore and Spencer (1990), respectively.

758 In this section, we use our volatile transport model to test how the N_2 ice deposits evolve when
 759 we set a North-South asymmetry in internal heat flux, surface N_2 ice albedo, and topography. All
 760 simulations start with a global and uniform cover of 300 m of N_2 ice, take into account glacial
 761 viscous flow of N_2 ice (Umurhan et al., 2017), and are run over 9 Myrs, which is long enough so
 762 that the surface and subsurface reach a steady state. Other simulation parameters and settings
 763 are summarized in Table 1.

764 5.1 North-South asymmetry in internal heat flux

765



766

767 Figure 4: Annual mean evolution of nitrogen ice thickness (in zonal mean) throughout entire VTM
 768 simulations (from $t=0$ to $t=9$ Myrs), assuming an internal heat flux in the northern hemisphere only
 769 (uniform from 0°N to 90°N) of 5, 15, 30 and 45 mW m^{-2} , and a subsurface bedrock thermal inertia

770 of 1000 SI. Deposits thinner than 1 m tend to be seasonal. The N₂ ice albedo obtained at
771 equilibrium is 0.755, 0.785, 0.790, and 0.795, respectively.

772

773

774 Brown and Kirk (1994) showed that Triton's internal heat source could significantly affect volatile
775 transport and that asymmetries in its latitudinal distribution (possibly driven by volcanic activity or
776 internal convection) could result in permanent caps of unequal latitudinal extent, including the
777 case with only one permanent cap. As expected, we find similar results when we test this scenario
778 in our volatile transport model.

779

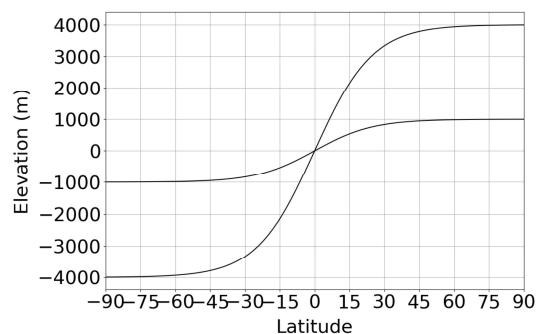
780 Figure 4 shows the annual mean evolution of N₂ ice thickness when we assume an internal heat
781 flux of 5, 15, 30 and 45 mW m⁻² in the northern hemisphere only (the internal heat flux is set to 0
782 mW m⁻² in the southern hemisphere). In the northern hemisphere, the internal heat flux transferred
783 to the surface N₂ ice is consumed through the latent heat of sublimation of N₂ ice and the
784 maintenance of vapor pressure equilibrium. This leads to enhanced N₂ sublimation rates and
785 reduced N₂ condensation rates and thus favors a larger southern N₂ ice cap.

786 Our results show that a permanent northern cap, centered at the pole with a thickness of at least
787 a few hundred meters, forms in all cases. In all cases there is also a southern permanent cap,
788 that is at least a kilometer thick at the pole and hundreds of meters thick at ~30°S, in agreement
789 with our interpretation of Voyager 2 observations.

790

791 Figure 4 shows that a heat flux difference of at least +15 mW m⁻² between both hemispheres is
792 necessary for permanent N₂ ice deposits (>1 m) in the northern cap to remain confined poleward
793 of 45°N (and therefore be hidden in the polar night during the Voyager 2 flyby). For example, if
794 the difference reaches +45 mW m⁻², then the permanent northern cap is very small and only
795 extends down to 80°N, according to our model. We note that in all cases, mm-to-m thick seasonal
796 deposits extend to 30°N-45°N.

797 5.2 North-South asymmetry in topography

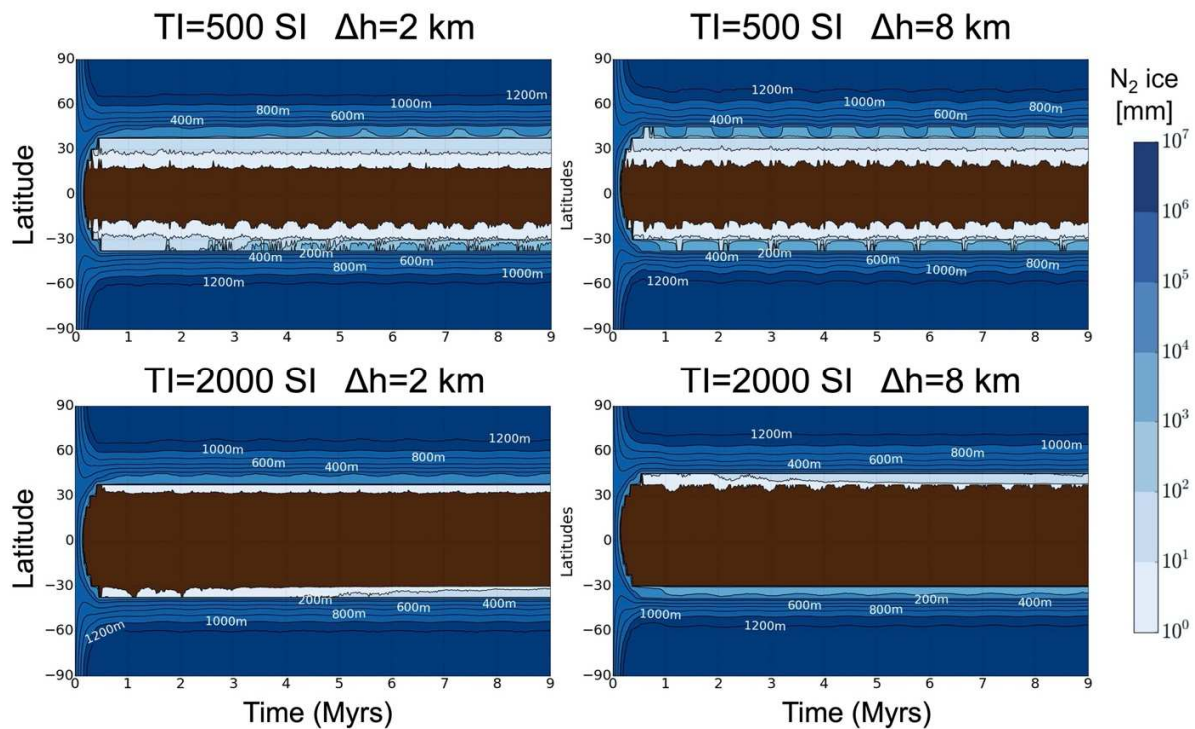


798

799 Figure 5: Topography of the bedrock for the simulations described in Section 5.2, with a North-
800 South asymmetry of ± 1 and ± 4 km.

801

802



803

804 Figure 6: Annual mean evolution of nitrogen ice thickness (in zonal mean) assuming a North-
 805 South asymmetry in topography (as shown on Figure 5, with a pole-to-pole difference of 2 and 8
 806 km), and a subsurface thermal inertia of 500-2000 SI. The N_2 ice albedo obtained at equilibrium
 807 is 0.740 and 0.750 (for $TI=500$ SI), and 0.740, and 0.745 (for $TI=2000$ SI), respectively.

808

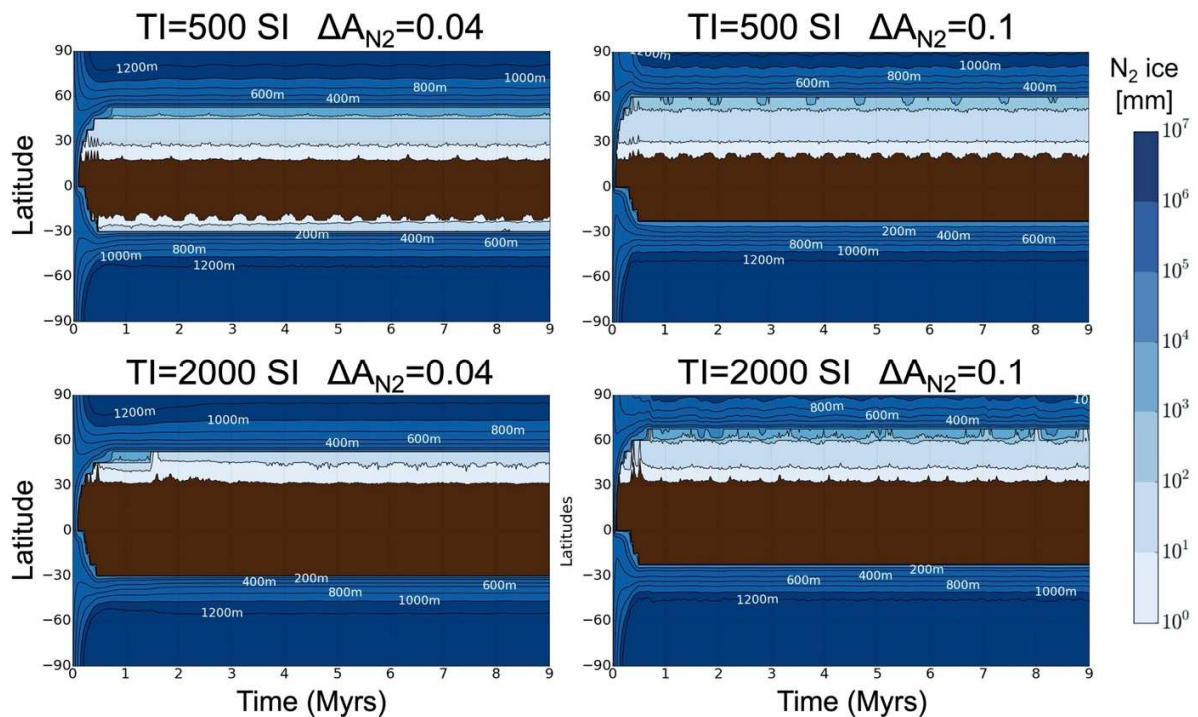
809 As detailed in Section 2.6, the main reservoir of N_2 ice on Pluto is confined within the massive
 810 topographic basin of Sputnik Planitia (estimated to be as much as ~ 10 km deep, McKinnon et al.,
 811 2016) due to (1) its location in the equatorial regions (long-term cold traps induced by the high
 812 obliquity cycles) and (2) higher condensation rates in the basin induced by higher surface
 813 pressure and infrared cooling of the ice. This atmospheric-topographic process is expected to
 814 apply on Triton too, and one could imagine that a North-South topographic asymmetry would favor
 815 the formation of a permanent cap of N_2 ice in the lower-elevation hemisphere. Voyager stereo
 816 and limb observations of Triton's topography (Schenk et al., 2021) are much more limited than for
 817 Pluto, but indicate that topographic amplitudes of the areas observed ($< 25\%$ of the surface) are
 818 only ~ 1 km or less, including the bright deposits of the southern hemisphere. Although topographic
 819 data were lacking over large areas, Schenk et al. (2021) concluded from the lack of discrete large
 820 bright or dark patches similar to Sputnik Planitia that Triton also lacked deep basins or high
 821 plateaus of similar scale. Unresolved basins and plateaus and local extremes of ~ 1 km scale are
 822 possible in these areas, however.

823 We tested the above scenario by performing simulations with a North-South asymmetry in
 824 bedrock topography, as shown by Figure 5, with a high-standing northern hemisphere and low-
 825 standing southern hemisphere of ± 1 and ± 4 km (the former case is well within the current limited
 826 constraints while the latter case is extremely unrealistic but provides insights into the magnitudes
 827 and extents of the processes involved). Figure 6 shows the annual mean evolution of N_2 ice
 828 thickness resulting from this model configuration and for different subsurface thermal inertias.

829 Our results show that the topography asymmetry does not have a strong effect on reducing the
 830 extent of the northern cap, even in the extreme case with a pole-to-pole dichotomy of 8 km. In
 831 this scenario, the low-elevated N₂ ice in the southern hemisphere is ~1 K warmer than the high-
 832 elevated N₂ ice in the northern hemisphere. As a result, the N₂ condensation rates should always
 833 be larger during southern winter than during northern winter. However, as N₂ ice extends to lower
 834 latitudes in the southern hemisphere (and because this is maintained by glacial flow in the model),
 835 more N₂ ice is available for sublimation during southern summer, which counteracts this
 836 difference. This allows for a permanent northern cap of N₂ ice to form in all cases and to be stable
 837 with an expansion of N₂ deposits to relatively low latitudes (40°N-50°N) while the permanent
 838 southern cap extends to 30°S. We also note that low TI allows for more seasonal deposits forming
 839 at the edge of the permanent deposits.

840 5.3 North-South asymmetry in nitrogen ice albedo

841



842

843 Figure 7: Annual mean evolution of nitrogen ice thickness (in zonal mean) assuming a North-
 844 South asymmetry in N₂ ice albedo and a subsurface thermal inertia of 500-2000 SI. The N₂ ice
 845 albedo in the southern hemisphere is automatically changed by the model so that it quickly
 846 converges toward a value allowing a surface pressure of ~1.4 Pa during the season of the
 847 Voyager 2 flyby (see Section 3.4.1). The N₂ ice albedo in the northern hemisphere remains always
 848 lower than that in the southern hemisphere by 0.04 (left panels) and 0.1 (right panels). The N₂ ice
 849 albedo obtained at equilibrium is 0.765 and 0.775 (for TI=500 SI), and 0.795, and 0.775 (for
 850 TI=2000 SI), respectively.

851

852 Volatile transport modeling performed by Moore and Spencer (1990) showed that a permanent
 853 North-South albedo dichotomy should result in a net, long-term transfer of N₂ from one cap to the
 854 other.

855 Here we tested this scenario with our volatile transport model by performing simulations with a
856 North-South asymmetry in nitrogen ice albedo and we obtained similar results. Figure 7 shows
857 the annual mean evolution of N₂ ice thickness predicted by our model when the N₂ ice albedo in
858 the northern hemisphere is lower by 0.04 (left panels) and 0.1 (right panels) than in the southern
859 hemisphere (where the albedo is calculated by the model so that P1989~1.4 Pa), for thermal
860 inertia TI=500 SI (top) and 2000 SI (bottom).

861 A permanent northern cap forms in all cases, but extends to 45-55°N (with mm-to-m thick
862 seasonal deposits extending to 30°N if TI is low) while the permanent southern cap extends to
863 30°S.

864 5.4 Discussions about the North-South asymmetry

865 We tested the scenarios of a North-South asymmetry in heat flux, topography, and N₂ ice albedo,
866 and our results are consistent with previous work (Brown and Kirk, 1994, Moore and Spencer,
867 1990).

868 We note that:

869 (1) We used a large global N₂ reservoir of 300 m, which is required for the expansion of the
870 southern cap to 30°S-0°, as observed by Voyager 2.

871 (2) As described in Brown and Kirk (1994), this N₂ inventory is significantly larger than needed
872 to supply volatile transport. Viscous flow of N₂ ice from the poles (where N₂ condensation
873 is more intense) toward low latitudes balances the net sublimation-condensation flow. On
874 average over several seasonal cycles, net N₂ condensation occurs at the poles and net
875 sublimation occurs in the warm tropical regions, where viscous flow from the pole to the
876 equator ensures that N₂ ice remains available for sublimation. This favors the formation of
877 a permanent northern cap and its expansion to relatively low latitudes.

878 (3) North-South asymmetries in internal heat flux and in surface ice albedo are efficient means
879 to limit the extent of the permanent northern cap to latitudes northward of 45°N. On
880 average over several seasonal cycles, the N₂ condensation rates at the south pole are
881 larger than those at the north pole by a factor ~8 if the surface N₂ ice albedo is 0.6 in the
882 northern hemisphere vs 0.7 in the southern hemisphere (Figure 7), or if the internal heat
883 flux is 45 W m⁻² in the northern hemisphere vs 0 W m⁻² in the southern hemisphere (Figure
884 4). The asymmetry in topography does not produce a significant asymmetry in cap extents.
885 Even in the case of a topography gradient of 8 km between both poles (Figure 6), the
886 surface temperature gradient is less than 1 K (the ice is warmer in the modeled depression
887 at the south pole) and the condensation rates are larger at the south pole by only a factor
888 of ~1.4. In other words, our results remain quantitatively sensitive to the ice properties
889 (albedo, thermal inertia, N₂ reservoir), and insensitive to topography differences, even
890 those that are larger than expected based on Voyager 2 imagery (although this is true for
891 large N₂ reservoirs only, see below).

892 (4) The northern and southern permanent caps simulated with our model quickly reach a
893 steady state after ~1 Myrs and then remain relatively stable over time. If we assume an
894 initially warm volatile-free northern hemisphere, it could take a few Myrs longer, but the
895 end result would remain the same. Note that the timescale associated with viscous flow
896 relaxation is ~1 Myrs for a relatively flat bedrock, a layer of 100 m of N₂ ice, and a
897 characteristic length scale for the southern cap of 1000 km (calculated for Triton as
898 detailed in Umurhan et al., 2017, see their Fig. 9b).

899 (5) Figure 8 shows a few simulation results performed with lower reservoirs (30 m and 100
900 m). Due to the lower reservoirs, the southern and northern caps are smaller in size and

901 thickness, but the general tendencies observed for the simulations with 300 m remain
902 valid. As in Spencer (1990), Stansberry et al. (1990), Hansen and Paige (1992) and
903 Spencer and Moore (1992), simulations performed with very low global N₂ reservoirs (e.g.
904 1 m, not shown) show that most of Triton's N₂ inventory accumulates at the south pole
905 (favored by a North-South asymmetry), and after several seasonal cycles, forms a small
906 southern permanent deposit confined to the south pole and a few meters thick (referred
907 as the problem of ever-shrinking permanent polar caps in Spencer and Moore, 1992). Due
908 to the low amounts of N₂ ice involved, the ice does not flow, and the polar cap never
909 extends to the mid-to-equatorial regions. Thin seasonal deposits can form at the north
910 pole during winter. The topography, albedo and internal flux differences between both
911 poles becomes a more significant driver for N₂ ice migration in these low reservoir cases.

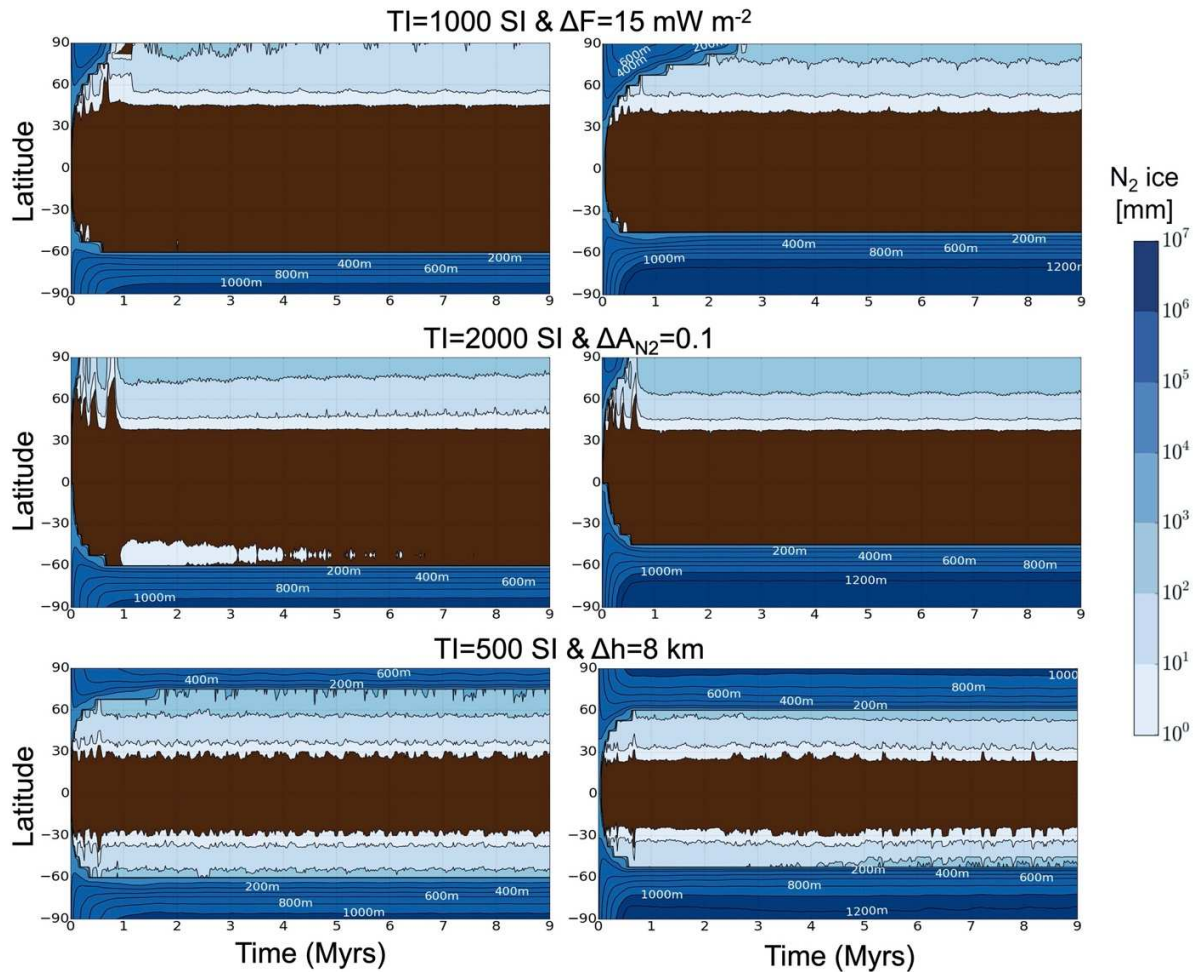
912 (6) Brown and Kirk (1994) and Moore and Spencer (1990) state that an albedo asymmetry
913 between the northern and southern hemispheres is unlikely to be maintained over a long-
914 term period due to (1) seasonal deposition of meter-thick frost layers each winter in the
915 low-albedo hemisphere, possibly brightening the surface except if the layers are
916 transparent enough to have no significant effect on the albedo of the substrate (which
917 remains unlikely), and (2) an increase in albedo as the ice is fractured by passage through
918 the α - β phase transition (Scott, 1976, Duxbury and Brown, 1993). On the other hand, pole-
919 to-pole difference in ice contamination by dark material, sensible heat flux from the
920 atmosphere or positive feedbacks on the surface (shown to have a non-significant effect
921 on Pluto's ice, Bertrand et al., 2020a) may help maintaining an albedo asymmetry, but
922 these processes would need to be investigated in more detail on Triton.

923

924 (7) Amongst the simulations explored here, we do not get any case with N₂ ice at southern
925 low- and mid-latitude but no N₂ ice at the south pole, as suggested by Earth-based
926 spectroscopic observations (see Section 2.3).

927 (8) Many other processes could explain the asymmetry between the caps. The reader is
928 referred to Section 2.6 and previous work by Brown and Kirk (1994) and Moore and
929 Spencer (1990) for more detail about this topic. Constraining the composition of the ices
930 on both hemispheres will be key to distinguishing between these alternatives.

931



932

933 Figure 8: As for previous figures but for a global N_2 reservoir $R=30$ m (left) and $R=100$ m (right).
 934 The N_2 ice albedo obtained at equilibrium is 0.775, 0.750 and 0.720 (for $R=30$ m), and 0.790,
 935 0.765 and 0.745 (for $R=100$ m), respectively.

936

937 6. Surface pressure cycle assuming fixed N_2 ice distribution

938

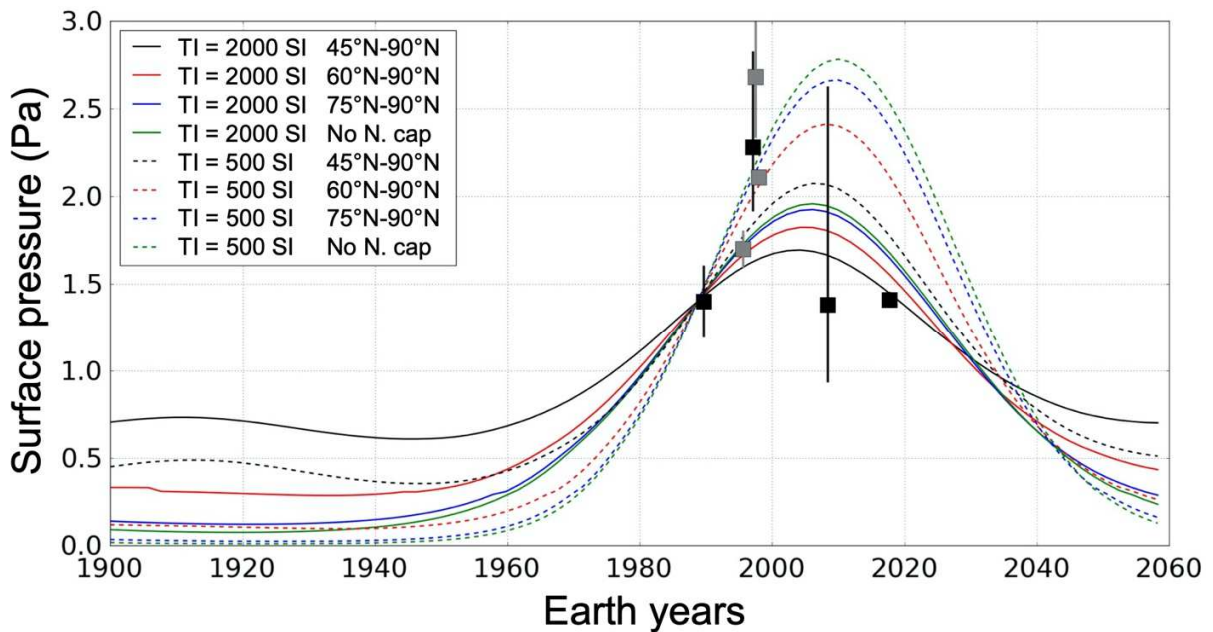
939 As shown in Section 5, the permanent (i.e., non seasonal) northern and southern caps remain
 940 relatively stable over time (if we assume the seasonal changes in insolation as described in
 941 Section 2.1) but their latitudinal extents depend on the model parameters such as albedo, thermal
 942 inertia, and N_2 ice reservoir.

943 In this section, we explore how fixed N_2 ice distributions on Triton and surface properties affect
 944 the current surface pressure cycle. For sake of simplicity, and in order to understand the impact
 945 of each parameter one after another, we neglect the impact of seasonal deposits and therefore
 946 we only use fixed volatile ice distribution (more realistic simulations with full, i.e., self-consistent,
 947 volatile transport including seasonal deposits are presented in Section 7). We use the stellar
 948 occultation datasets to constrain the properties of the northern and southern caps.

949 6.1 Initial state of the simulations with fixed N₂ ice distribution

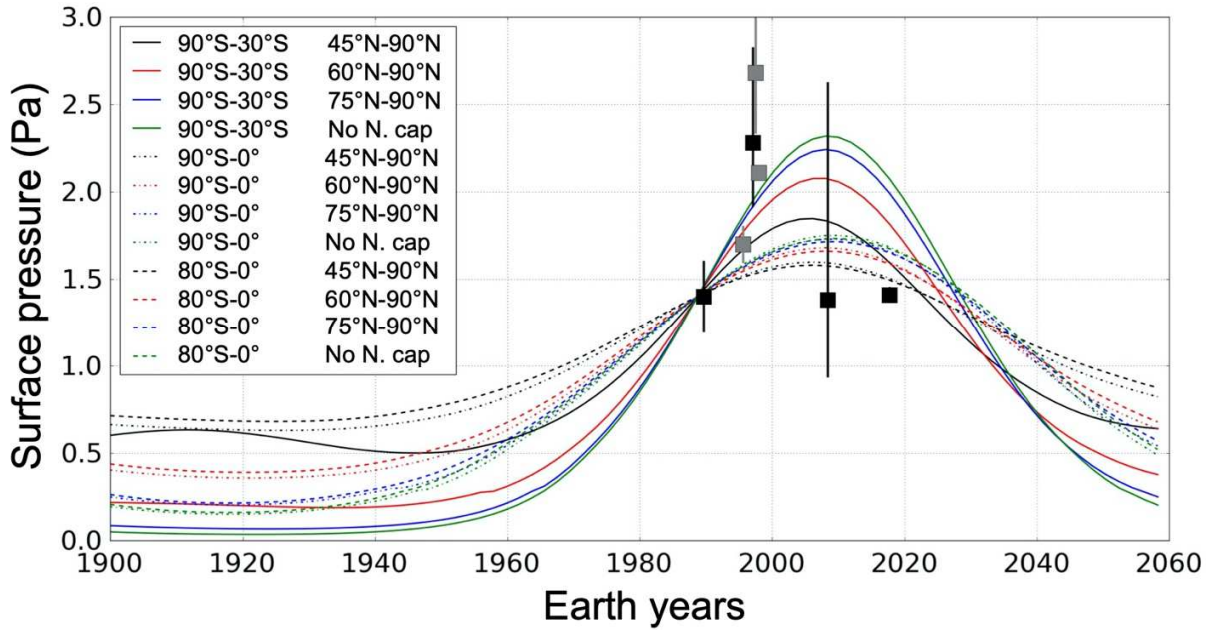
950 Table 1 summarizes the settings of the volatile transport simulations presented in this section.
 951 We place fixed and infinite N₂ reservoirs (no glacial flow, flat topography) confined to 90°S-30°S,
 952 90°S-0°, or 80°S-0° in the southern hemisphere, and to 90°N-75°N, 90°N-60°N or 90°N-45°N in
 953 the northern hemisphere (including the case without a northern cap). We limit the volatile transport
 954 to these reservoirs (no seasonal frost can form). Consequently, the simulation results are
 955 independent of the bedrock surface properties (albedo and emissivity). The simulations are
 956 performed over several seasonal cycles (covering ~10 000 Earth years) in order to reach a steady
 957 state. The N₂ ice albedo is automatically adjusted by the model so that the surface pressure
 958 reaches ~1.4 Pa in 1989, as observed (see Section 3.4.1).

959 6.2 Simulation results with fixed N₂ ice distribution



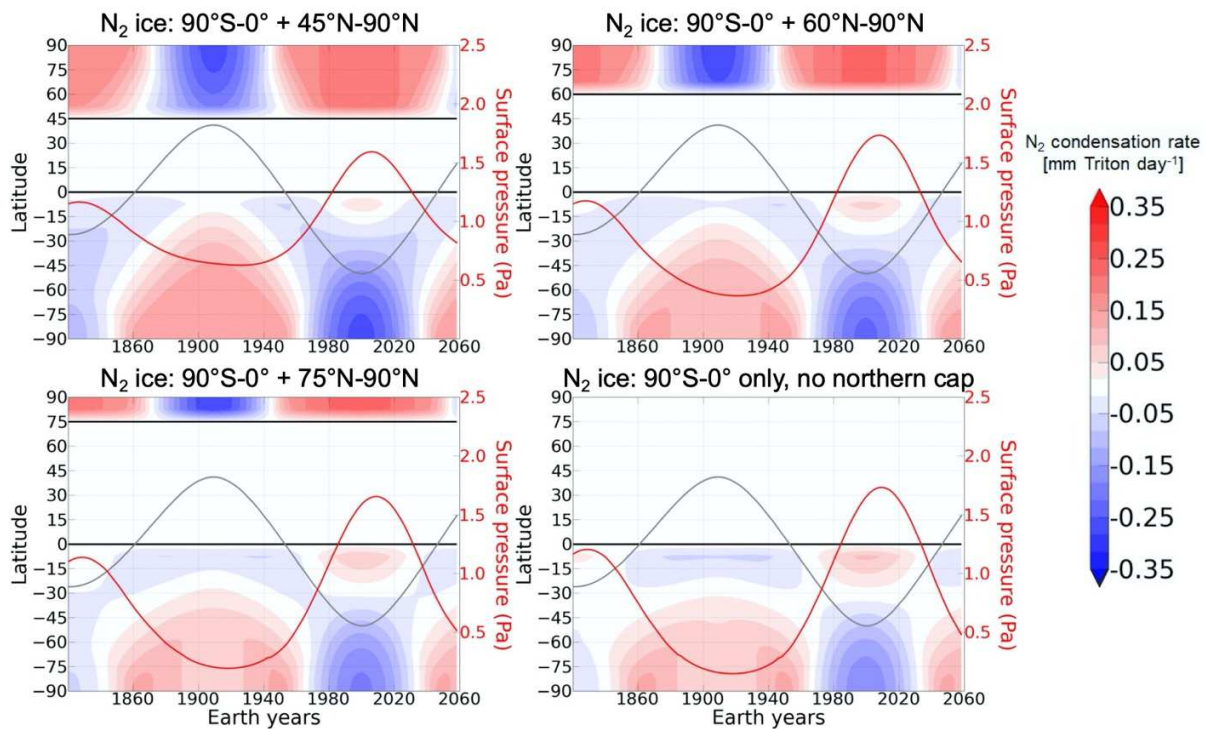
960
 961 Figure 9: Surface pressure on Triton for the period 1900-2060 as predicted by the model when
 962 we assume a fixed N₂ ice distribution with a southern cap placed between 90°S-30°S and a
 963 northern cap placed between 90°N-45°N (black), 90°N-60°N (red), 90°N-75°N (blue) or no
 964 northern cap (green). The seasonal thermal inertia of N₂ ice is set to 2000 SI (solid lines) or 500
 965 SI (dotted lines). Black and grey data points and 3-σ error bars represent the pressure
 966 observations as presented in Table 2 (black are for the data points that we consider are the
 967 strongest observational constraints).

968



969
970
971
972

Figure 10: As Figure 9 but for different fixed N_2 ice distributions in the southern and northern hemisphere. The seasonal thermal inertia is set to 1000 SI.



973
974
975
976
977

Figure 11: Zonal and diurnal mean N_2 condensation-sublimation rate (mm per Triton day) during the period 1820-2060 as obtained in the model for the cases of fixed N_2 ice distributions: $90^\circ\text{S}-0^\circ + 45^\circ\text{N}-90^\circ\text{N}$ (top left), $90^\circ\text{S}-0^\circ + 60^\circ\text{N}-90^\circ\text{N}$ (top right), $90^\circ\text{S}-0^\circ + 70^\circ\text{N}-90^\circ\text{N}$ (bottom left), $90^\circ\text{S}-0^\circ$ and no northern cap (bottom right). The seasonal N_2 ice thermal inertia is set to 1000 SI. The

978 thin black contour indicates the extent of the caps. The red line indicates the surface pressure
979 (right y-axis) and the grey line indicates the subsolar latitude.

980

981 Figures fixedscap and fixedti show the surface pressure for the period 1900-2060, obtained with
982 the model for different N₂ ice distributions and N₂ ice thermal inertia, while Figure 11 shows the
983 latitudinal condensation-sublimation flux of N₂ during the period 1820-2060 for the four different
984 extents of the northern cap explored.

985 The surface pressure is at its minimum during the 1880-1940 period (northern summer), when
986 the subsolar point is above 15°N, because the northern cap is always smaller than the southern
987 cap and therefore the condensation-dominated areas (most of the southern N₂ ice deposits)
988 overcome the sublimation-dominated areas (the northern deposits). During the opposite season
989 (southern summer), the pressure is at its maximum as the sublimation-dominated areas (most of
990 the southern deposits) overcome the condensation-dominated areas (northern deposits), as
991 shown by Figure 11 (all panels). In these simulations, the surface pressure peak occurs slightly
992 after the southern summer solstice (2000) between year 2000-2010. The surface pressure
993 evolutions obtained here are similar to those obtained by Spencer and Moore (1992) when they
994 artificially maintained a permanent large southern cap of bright N₂ (see their Fig. 7).

995 As shown by Figure 9, the larger the northern cap, the more it can serve as a condensation area
996 and buffer N₂ sublimation in the southern hemisphere, which results in a surface pressure peak
997 that is lower and occurs sooner. In addition, the higher the thermal inertia of N₂ ice, the lower the
998 amplitude of surface pressure over a seasonal cycle (higher minimum and lower maximum), and
999 the earlier the surface pressure peaks.

1000 We also tested different N₂ ice distributions in the southern hemisphere. Figure 10 shows that the
1001 amplitude of the surface pressure peak is strongly attenuated if N₂ ice remains between 30°S-0°
1002 (non-solid lines). This is because these latitudes are dominated by condensation rather than
1003 sublimation between the years 1980-2020, thus dampening the pressure peak (Figure 11, all
1004 panels). We also tested a scenario without N₂ ice between 90°S-80°S, leading to a pressure peak
1005 slightly lower as less N₂ is available for sublimation in southern summer (Figure 10, dotted lines).

1006 These results suggest that a mid-to-high thermal inertia of N₂, coupled with a northern cap
1007 extending down to 45°N-60°N, is needed so that the surface pressure is ~1.4 Pa (back to Voyager
1008 2 levels) in 2017, as observed from stellar occultations. If we assume no northern cap, then the
1009 modeled surface pressure remains higher than 1.6 Pa in 2017, which becomes inconsistent with
1010 the observations. A strong increase in surface pressure before 2000 cannot be obtained if N₂ ice
1011 is present between 30°S-0°. We also note that the surface pressure remains greater than 0.5 Pa
1012 even during the opposite season (southern winter) when a permanent northern cap extending
1013 down to 45°N is assumed. The presence of permanent southern and northern caps prevents
1014 Triton's atmosphere from collapsing.

1015 Finally, as discussed in Section 2.3, IRTF/SpeX observations of Triton's near-IR spectrum in 2002
1016 suggest that N₂ is undetectable or absent at high southern latitudes. Here, Figure 11 shows that
1017 about 30-50 cm of N₂ ice is removed at the south pole by sublimation during the period 1970-
1018 2000. It is not clear whether the removal of 30-50 cm of N₂ ice could have altered its detectability,
1019 even if N₂ is not completely removed. We discuss more on this point in Section 8.3.

1020 7. VTM Simulations of the N₂ cycle

1021 In this Section, we simulate the full volatile transport across Triton over the last 4 Myrs and explore
1022 a large range of parameters (bedrock albedo, thermal inertia, N₂ ice reservoir, internal flux and

1023 North-South asymmetry). The results (e.g., cap extents in 1989 and surface pressure in 2017)
 1024 are compared to the available observations in order to better constrain these model parameters.

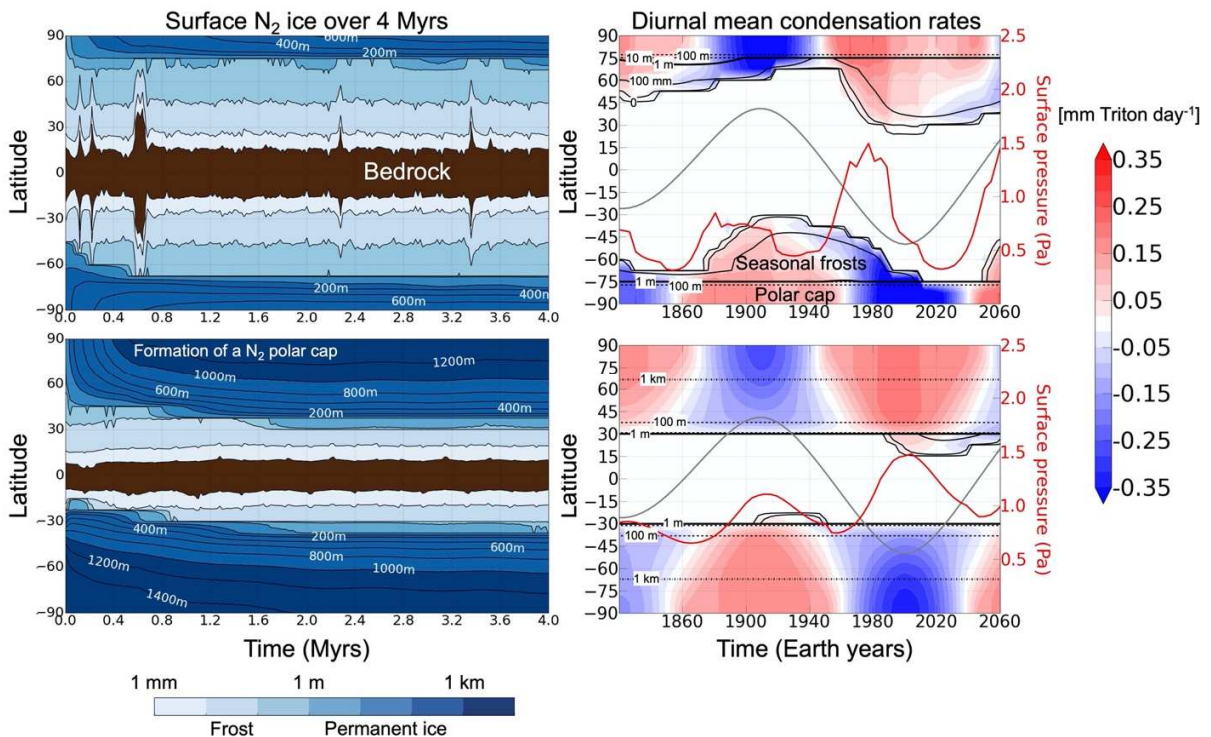
1025 7.1 Initial state of the simulations and main model parameters

1026 Section 3.3 and Table 1 summarize the initial state of the simulations. Note that all the results of
 1027 this section are the outcome of 4-Myrs simulations in which the end state does not depend on the
 1028 initial ice distribution and surface and subsurface temperatures, and in which the N_2 ice albedo is
 1029 calculated by the model and constrained by the surface pressure in 1989 (~ 1.4 Pa). The N_2 ice
 1030 albedo obtained in the model in 1989 usually ranges within 0.7-0.8, depending on the cap extents
 1031 and on the internal heat flux. We first perform simulations with a spatially uniform N_2 ice albedo
 1032 (Section 7.2) and then with a lower albedo in the northern hemisphere (Section 7.3, where the
 1033 albedo of the northern cap is always lower than that of the southern cap by 0.1).

1034 The bedrock and N_2 ice emissivities are fixed to $\varepsilon=0.8$, and the N_2 ice thermal inertia to $TIN_2=1000$
 1035 SI. We explore different values for the bedrock's thermal inertia TI_{bed} (Low: 200 SI; Moderate: 500
 1036 SI, 1000 SI; High: 2000 SI) and albedo A_{bed} (from 0.1 to 0.9), for the global N_2 ice reservoir R_{N_2}
 1037 (from 1 m to 650 m), and with and without a globally uniform internal heat flux of 30 mW m^{-2} .

1038 7.2 Full volatile transport simulations with spatially uniform ice properties (no North-South
 1039 asymmetries)

1040
 1041



1042
 1043 Figure 12: Results from a VTM simulation performed with spatially uniform N_2 ice properties. Top:
 1044 Simulation with $TI_{bed}=1000$ SI, $A_{bed}=0.8$, $R_{N_2}=12$ m. Bottom: $TI_{bed}=500$ SI, $A_{bed}=0.7$, $R_{N_2}=350$ m.
 1045 Left: annual mean evolution of N_2 ice thickness (in zonal mean) over 4 Myrs. Right: Zonal and

1046 diurnal mean N₂ condensation-sublimation rate (mm per Triton day) during the period 1820-2060.
1047 The black contours indicate the extent of the caps (0-line, 10 mm, 100mm, solid), and where the
1048 ice is 1 m (thick solid line) and 1 km thick (dash-dotted line). The red line indicates the surface
1049 pressure (right y-axis) and the grey line indicates the subsolar latitude. Deposits thinner than 1 m
1050 tend to be seasonal.

1051

1052

1053 Figure 12 shows examples of model results when a spatially uniform N₂ ice albedo is assumed,
1054 primarily in two formats: the long-term evolution of N₂ ice thickness over 4 Myrs (left panel) and
1055 the recent seasonal evolution of the diurnal mean N₂ condensation rates obtained during the
1056 1820-2060 period (as the outcome of the 4-Myrs simulation).

1057 First, in the long-term evolution, the northern hemisphere, initially warm and volatile-free, quickly
1058 cools down and allows the formation of a permanent northern cap, which stabilizes along with a
1059 symmetric southern cap after ~2 Myrs. The thickness and the extent of the caps depend on the
1060 global reservoir of N₂ ice. In the tropical regions, mm-to-m thick seasonal deposits can form and
1061 extend to the equatorial regions.

1062 Second, the seasonal evolution (right panel) shows that the southern cap sublimates from ~1960
1063 to ~2040, with N₂ condensing in the northern hemisphere. In the case of Figure 12 (top), the low
1064 amount of N₂ ice in the system reduces N₂ deposits to seasonal layers (mm-to-m thick) at latitudes
1065 equatorward of 70°N or of 75°S, and the southern cap retreats from 40°S to 75°S while the
1066 northern cap expands from 70°N to 20°N between 1960 and 2020. This leads to a strong decrease
1067 of surface pressure from 1989 as N₂ condensation-dominated areas increase in the north and as
1068 sublimation is limited in the south. In the case of Figure panel_uniform1 (bottom), there is enough
1069 N₂ ice on the surface so that the permanent northern and southern caps expand to 30°N and
1070 30°S, respectively. The peak of surface pressure is reached around year 2000, when the sources
1071 of N₂ in the south balance the sinks in the north (~2-3 mm Triton day⁻¹).

1072 In general, all simulations that assume spatially uniform subsurface and ice properties produce
1073 symmetric permanent caps. As shown by Figure 12, this results in either a northern cap that
1074 extends to latitudes southward of 45°N in 1989 (inconsistent with Voyager 2 observations) and/or
1075 a strong decrease of surface pressure between 1989 and 2017 (with values largely below the
1076 reported value of 1.41 Pa in 2017, inconsistent with stellar occultation observations).

1077 In the next section, we impose a North-South asymmetry in N₂ ice albedo in order to force a
1078 smaller northern cap.

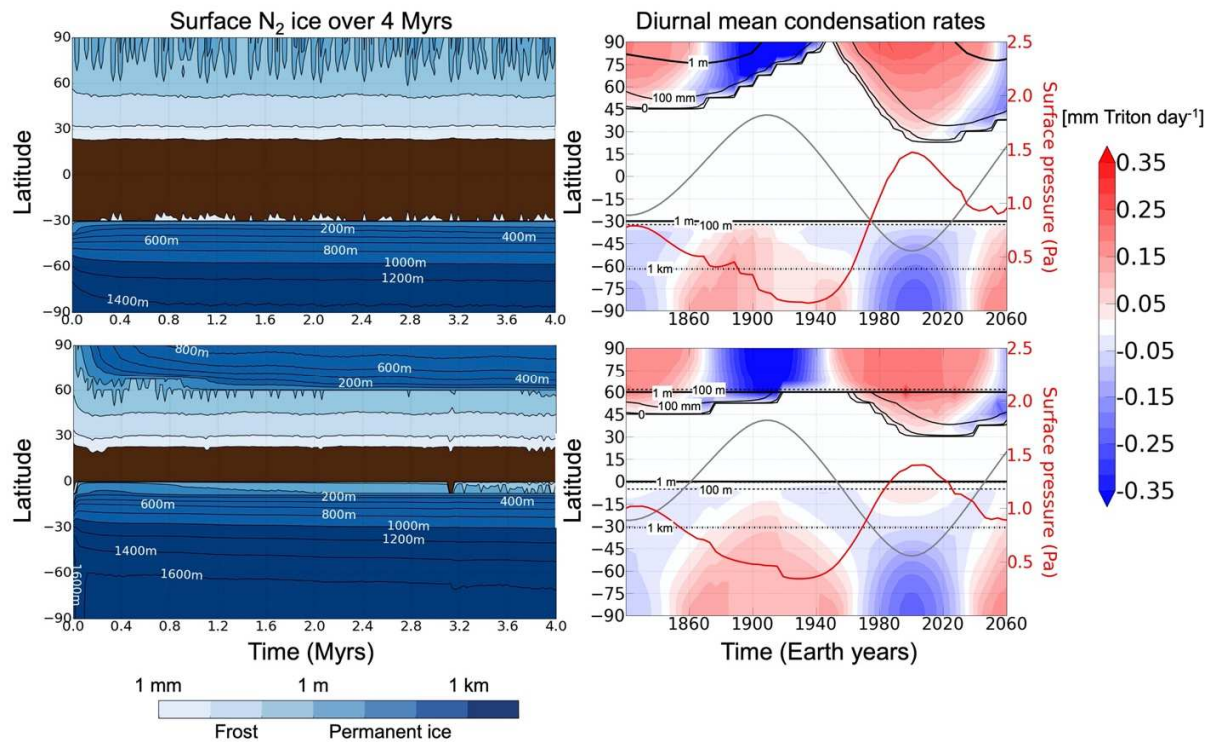
1079 7.3 Full volatile transport simulations with a North-South asymmetry in N₂ ice albedo

1080 In this section, we perform volatile transport simulations following the *Koyaanismuuyaw* model
1081 (Moore and Spencer, 1990): we assume that the N₂ ice albedo in the northern hemisphere is
1082 lower by 0.1 than that in the southern hemisphere, which leads to a larger permanent southern
1083 cap.

1084 7.3.1. Comparison to the case without North-South asymmetry

1085

1086



1087

1088 Figure 13: As Figure 12 but from a VTM simulation performed with a North-South asymmetry in
 1089 N_2 ice albedo ($\Delta A_{N_2}=0.1$). Top: Simulation with $T_{I_{bed}}=1000$ SI, $A_{bed}=0.7$, $R_{N_2}=200$ m. Bottom:
 1090 $T_{I_{bed}}=2000$ SI, $A_{bed}=0.7$, $R_{N_2}=550$ m.

1091

1092 Figure 13 (top) shows an example of a simulation performed with the North-South asymmetry in
 1093 N_2 ice albedo and a global N_2 reservoir of 200 m. A permanent, 1-km thick southern cap forms
 1094 and stabilizes with an extent to $30^\circ S$, due to the relatively high ice albedo and subsurface thermal
 1095 inertia. In the northern hemisphere, only seasonal mm-to-m thick deposits form (Figure 13, top
 1096 left). During the northern summer (1890-1940), these northern deposits entirely sublimate and
 1097 disappear (Figure 13, top right). In this simulation, N_2 re-condenses in the northern hemisphere
 1098 in the current southern summer, with a maximum extent of the frost to $\sim 30^\circ N$, reached in 2000.
 1099 The surface pressure peaks in ~ 2000 , and is back to Voyager levels in 2017, consistent with the
 1100 observations.

1101

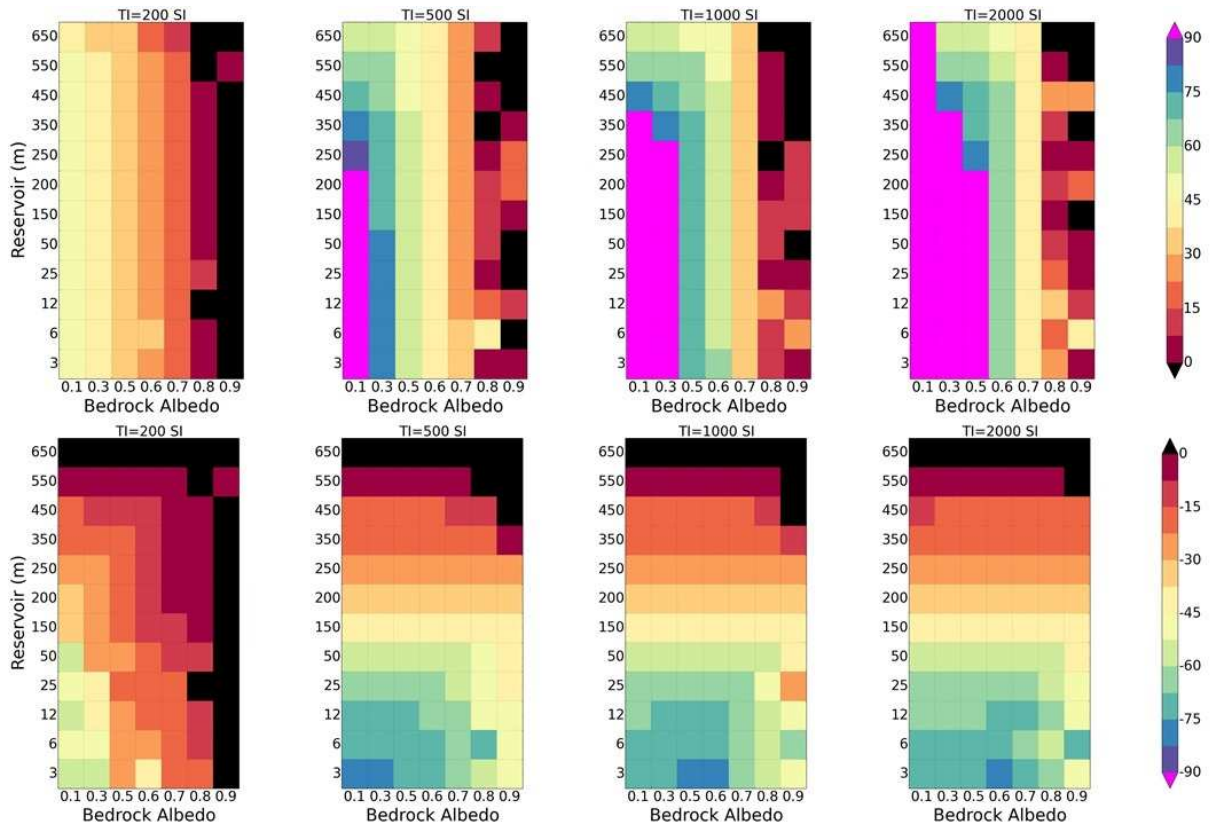
1102

1103 Figure 13 (bottom) describes a similar simulation but with a larger global N_2 ice reservoir
 1104 of 550 m. In this simulation, the permanent southern cap extends to the equator and a smaller
 1105 northern cap forms and extends to $60^\circ N$ (Figure 13, bottom left). The seasonal frosts in the
 1106 Northern hemisphere extend to $\sim 30^\circ N$ in 2000, and the pressure cycle is still consistent with the
 1107 observations with a maximum reached in 2005 and a value close to that of 1989 in 2017. Note
 1108 that N_2 re-condenses in the equatorial regions at the edge of the southern cap between 1980-
 1109 2020 (Figure 13, bottom right), as also shown in Section 6.2. This may be related to the formation
 1110 of the bright blue fringe observed in these regions by Voyager 2 (see discussion on this topic in
 1111 Section 8.4).

1112

1113 7.3.2. Sensitivity of the results to surface properties, internal heat flux and ice reservoir

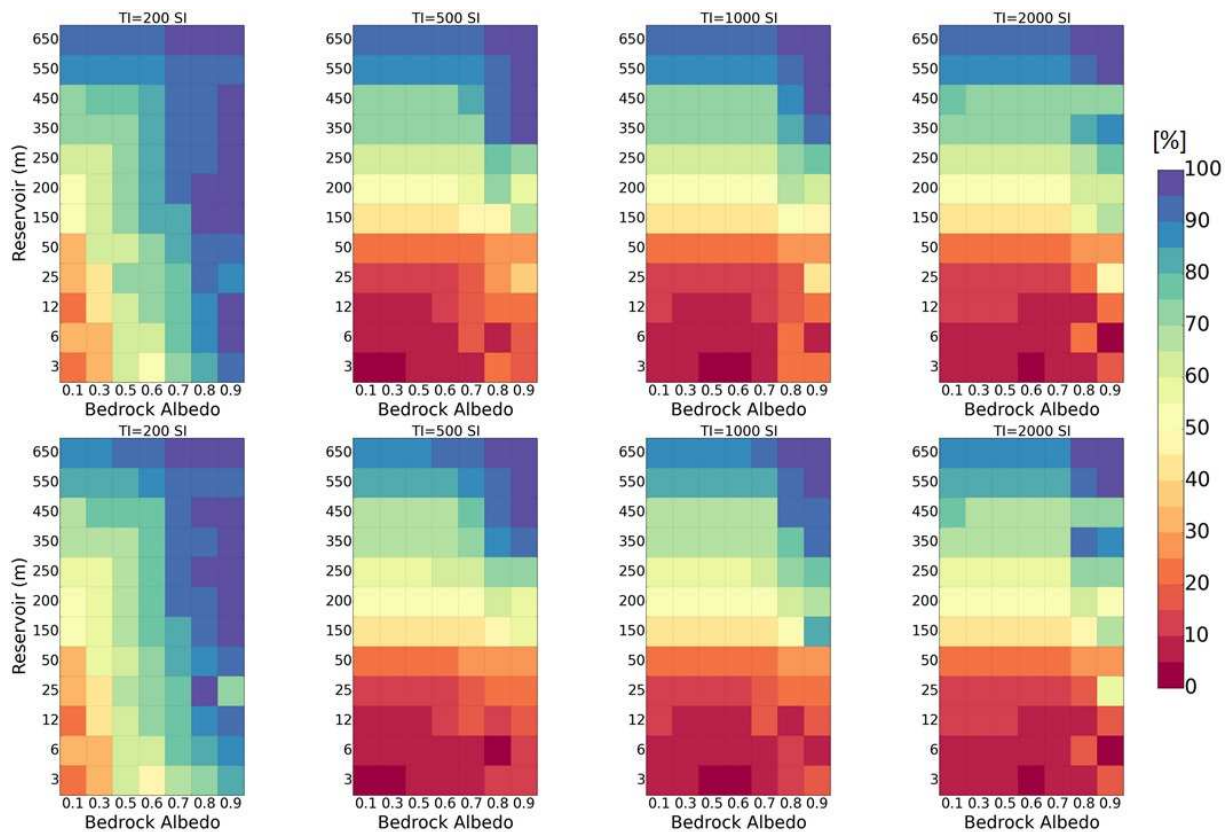
1114



1115

1116 Figure 14: Latitude to which the northern (top) and southern (bottom) caps expand (from the pole)
1117 in 1989 as modeled by simulations with varying subsurface thermal inertia (columns, TI = 200,
1118 500, 1000, and 2000 SI from left to right), N₂ global reservoir (y-axis) and bedrock albedo (x-axis).
1119 The simulations that best match Voyager 2 observations in 1989 are those that show a northern
1120 cap confined poleward of 45°N and a southern cap that extends to 30°S at least.

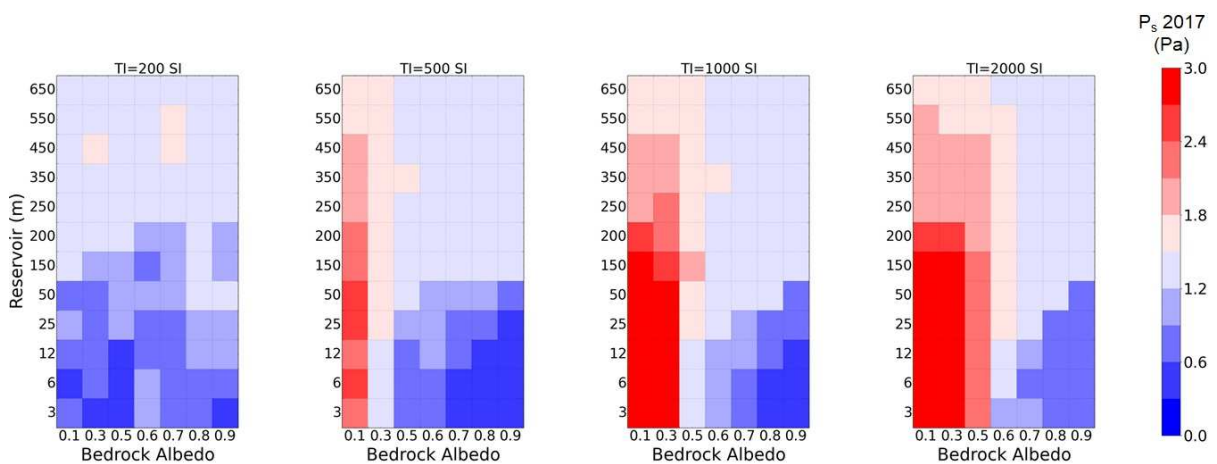
1121



1122

1123 Figure 15: Modeled volatile fractional area (%) in 1995 (top) and 2010 (bottom), projected on the
 1124 visible disk at these dates, with varying subsurface thermal inertia (columns, TI = 200, 500, 1000,
 1125 and 2000 SI from left to right), N₂ global reservoir (y-axis) and bedrock albedo (x-axis). The
 1126 simulations that best match Earth-based spectroscopic observations are those that show a
 1127 volatile fractional area of 50-60% in 1995 (Quirico et al., 1995) and 60-70% in 2010 (Merlin et al.,
 1128 2018). Note that the extent of the southern cap and the latitude of the subsolar point do not change
 1129 much between 1995 and 2010, hence the relatively unchanged volatile fractional area during this
 1130 period of time.

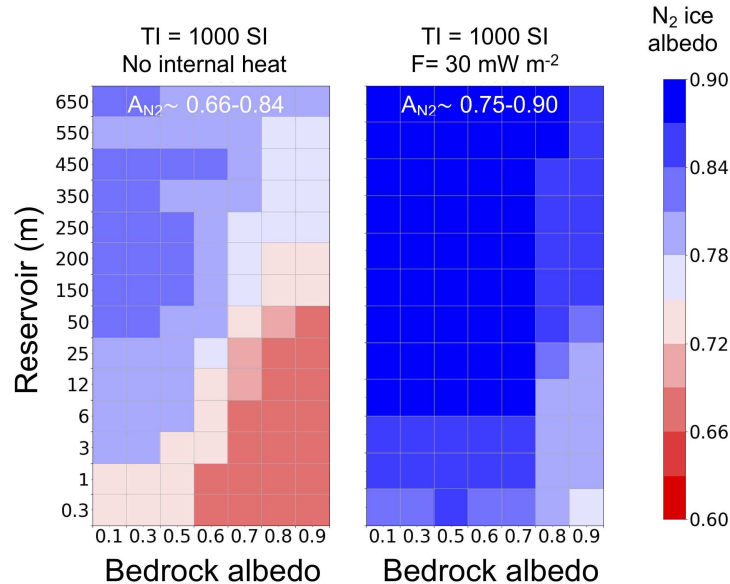
1131



1132

1133 Figure 16: Surface pressure on Triton in 2017 as modeled by simulations with varying subsurface

1134 thermal inertia (columns, TI = 200, 500, 1000, and 2000 SI from left to right), N₂ global reservoir
 1135 (y-axis) and bedrock albedo (x-axis). The simulations that best match the 2017 stellar occultation
 1136 data are those that show a surface pressure of ~1.41 Pa (Marques Oliveira et al., 2021).



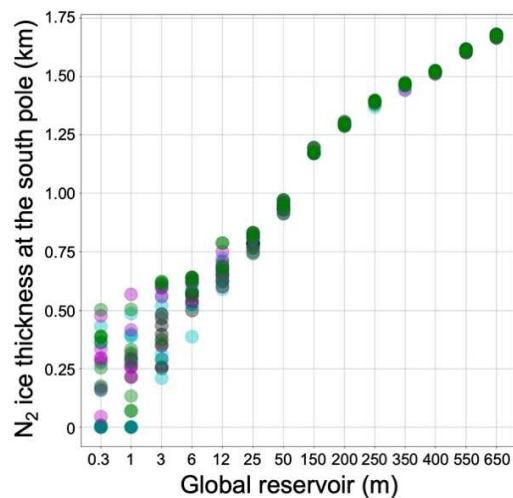
1137
 1138 Figure 17: N₂ ice albedo in the southern hemisphere in 1989 as modeled by simulations without
 1139 (left) and with internal heat flux (right), and for different N₂ global reservoir (y-axis) and bedrock
 1140 albedos (x-axis). Albedos in the model are Bond albedos. The subsurface thermal inertia is set to
 1141 1000 SI.

1142
 1143 We performed similar simulations with varying combinations of bedrock subsurface thermal
 1144 inertias (TI = 200, 500, 1000, and 2000 SI), N₂ global reservoirs (from 0.3 m to 650 m) and bedrock
 1145 albedos (from 0.1 to 0.9). We also explored how results are impacted by a uniform internal heat
 1146 flux of 30 mW m⁻². The model sensitivity to these parameters is described by (1) Figure 14, which
 1147 shows the extent of the caps in 1989, (2) Figure 15, which shows the modeled volatile fractional
 1148 area as seen from Earth in 1995 and 2010, (3) Figure 16, which shows the surface pressure in
 1149 2017, and (4) Figure 17, which shows the value of the N₂ ice albedo in 1989 calculated by the
 1150 model so that the surface pressure reached the observed value (~1.4 Pa). We also tested how
 1151 the volatile cycle responds to a lower N₂ ice emissivity ($\epsilon_{N_2}=0.3, 0.5$, and taking into account the
 1152 α - β phase transition) and higher values of thermal inertias (TI = 4000, 8000 SI).

1153
 1154 **Sensitivity to the N₂ reservoir**

1155 N₂ ice accumulation is always favored in the southern hemisphere, due to the north-south N₂ ice
 1156 albedo asymmetry. As a result, the extent of the southern cap (and thus the volatile fractional
 1157 area) strongly depends on the global N₂ reservoir and the viscous flow of N₂ (Figure 14, bottom).
 1158 This is illustrated by Figure 18. The more N₂ in the system, the thicker the cap, the more it flows
 1159 toward the equator, and the more the ice subsists through an extreme summer (larger perennial
 1160 cap). On the other hand, a low reservoir would lead to a small and thin southern cap, with seasonal
 1161 deposits that disappear during the recent extreme southern summer. As a result, simulations with
 1162 low reservoirs also lead to a low volatile fraction area in 1995-2010 (except for the low thermal
 1163 inertia case) and to surface pressures much lower in 2017 than in 1989 as condensation in the

1164 north then dominates sublimation in the south. Reservoirs lower than 150 m coupled with
 1165 moderate-to-high bedrock TI lead to a southern cap extending to latitudes poleward of 45°S in
 1166 1989, a volatile fraction area less than 40% in 1995-2010 (Figure 15) and surface pressure lower
 1167 than 1.2 Pa in 2017 (Figure 16s), which is inconsistent with Earth-based spectroscopic
 1168 observations and the 2017 stellar occultation. Very large reservoirs (> 350 m) tend to lead to a
 1169 higher volatile fraction area than observed (>70%). They also lead to a higher seasonal minimum
 1170 and a lower seasonal maximum in surface pressure, due to the fact that the caps extend to lower
 1171 latitudes and are more perennial (limited amounts of seasonal deposits), which better balances
 1172 the sources and sinks of N₂ (see Figure 9). A maximal surface pressure of ~2 Pa is reached during
 1173 southern extreme summer for intermediate N₂ reservoirs of 12 m - 450 m coupled with
 1174 intermediate thermal inertia (not shown).



1175
 1176 Figure 18: Modeled maximum N₂ ice thickness at the south pole in 1989 vs initial global N₂ ice
 1177 reservoirs for all simulations performed with north-south N₂ ice albedo asymmetry, no internal
 1178 heat flux. Colors indicate the thermal inertia (black: 200 SI; cyan: 500 SI; magenta: 1000 SI; green:
 1179 2000 SI). For large reservoirs greater than 25 m in global average, the maximum thickness of the
 1180 ice at the south pole mostly depend on the reservoir (and not on the thermal inertia or albedo of
 1181 the bedrock).

1182

1183 **Sensitivity to the bedrock albedo**

1184 The extent of the northern cap does not strongly depend on the global N₂ reservoir but rather on
 1185 the bedrock albedo (Figure 14). This is because N₂ ice is more stable within the southern cap and
 1186 only allows a cap to form in the northern hemisphere if the surface is cold enough there (which,
 1187 in our model, is driven by the bedrock albedo). As described in Section 7.1, our simulations are
 1188 initialized with a warm northern hemisphere depleted of volatile ice. After several Myrs required
 1189 to reach a steady state, most of these simulations present a permanent and/or seasonal northern
 1190 cap in 1989, except when we assume a bedrock albedo much lower than 0.6 and a mid-to-high
 1191 subsurface thermal inertia (Figure 14, top). Such a low albedo value for Triton's bedrock is
 1192 unrealistic, as the surface was observed to be relatively bright in 1989 (with a bolometric Bond
 1193 albedo at least greater than 0.5, McEwen, 1990). Furthermore, Figure 16 shows that a low
 1194 bedrock albedo coupled with a mid-to-high thermal inertia tends to lead to a high surface pressure
 1195 (as this would limit N₂ condensation in the northern hemisphere), greater than 1.8 Pa in 2017
 1196 (Figure 16), which is not consistent with the 2017 stellar occultation. On the other hand, a very

1197 high bedrock albedo would favor more N₂ condensation in the north during southern summer,
1198 leading to a northern cap extending to the equator in 1989 and a low surface pressure in 2017,
1199 which is also inconsistent with observations (Figure 14, top, Figure 16). For instance, if the N₂
1200 reservoir is lower than 150 m, the southern cap considerably shrinks during this season, leading
1201 to surface pressures lower than 1.2 Pa in 2017, inconsistent with the 2017 stellar occultation
1202 (Figure 16).

1203

1204 **Sensitivity to the bedrock thermal inertia**

1205 The lower the bedrock thermal inertia, the higher the amplitude of bedrock surface and subsurface
1206 temperatures across the seasons (higher temperatures during summer, lower temperatures
1207 during winter), and, on average over seasonal cycles, the lower the temperatures, in particular at
1208 the poles. As a result, a lower bedrock thermal inertia leads to the formation of more mm-to-m
1209 seasonal frosts that extend to lower latitudes. In our simulations performed with the low TI = 200
1210 SI and relatively high bedrock albedo (>0.5), the northern cap extends to 15°N in 1989 (Figure
1211 14, top), which is inconsistent with Voyager 2 observations. However, the volatile fractional area
1212 is consistent with Earth-based spectroscopic observations for low thermal inertia coupled with low
1213 to moderate reservoirs and a surface albedo of ~0.6 (Figure 15). The increased presence of
1214 seasonal N₂ frosts forming in the northern hemisphere during winter in the case of low thermal
1215 inertia prevents an increase of surface pressure after 1989. As a result, low thermal inertia tends
1216 to lead to slightly low surface pressure (< 1.2 Pa) in 2017, especially when the N₂ reservoir is low
1217 (frosts would disappear in the southern hemisphere shortly after 1989). Moderate-to-large thermal
1218 inertia (500-2000 SI) limits the decrease of surface and subsurface temperature in the northern
1219 hemisphere during winter and thus allows for a limited extent of the northern cap in 1989. Surface
1220 pressure tends to increase from 1989 to ~2005-2010 and then decrease with a 2017 value close
1221 to that of 1989. Finally, we show on Figure 19.D two simulation cases performed with extremely
1222 (and possibly unrealistically; Ferrari and Lucas, 2016) high thermal inertias of 4000 SI and 8000
1223 SI. Changes to the N₂ cycle are not significant in the case with TI=4000 SI. With TI=8000 SI,
1224 thicker deposits accumulate in the northern hemisphere and the seasonal changes of surface
1225 pressure are reduced, with a higher pressure minimum at 0.5 Pa.

1226

1227 **Sensitivity to the internal heat flux**

1228 A higher internal heat flux (uniformly applied across the globe) increases the surface and
1229 subsurface temperature for a given insolation. In order to keep a surface pressure of ~1.4 Pa in
1230 1989, the N₂ ice must thus remain at the same vapor-pressure equilibrium temperature and must
1231 therefore be brighter. In general, an internal heat flux of 30 mW m⁻² leads to an increase in N₂ ice
1232 albedo of 0.1 compared to the case without internal heat flux (Figure 17) and as a result to slightly
1233 lower condensation and sublimation rates. The evolution of the surface pressure and the extent
1234 of the southern and northern caps remain relatively similar to the cases without internal heat flux.

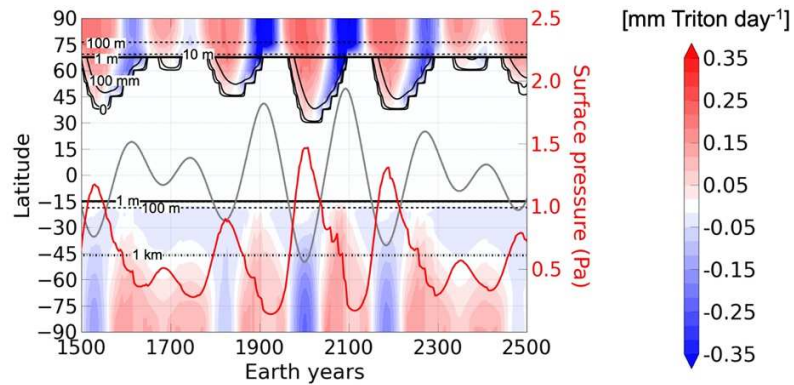
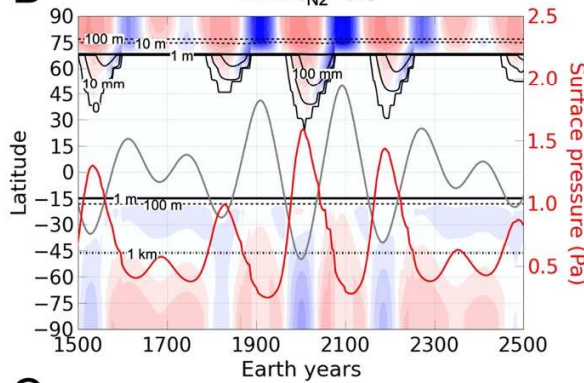
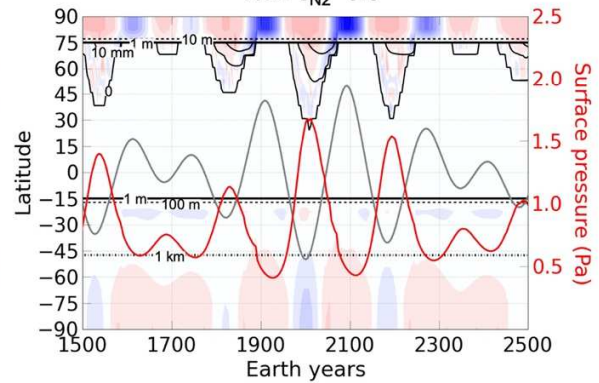
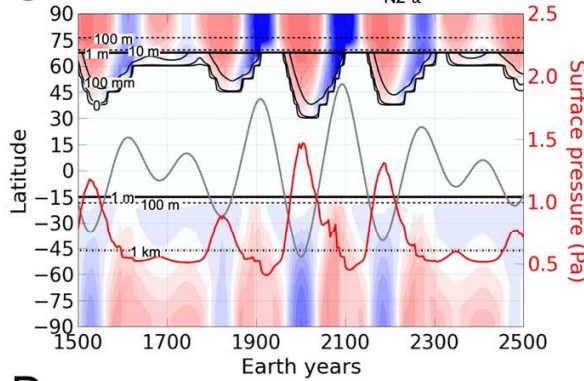
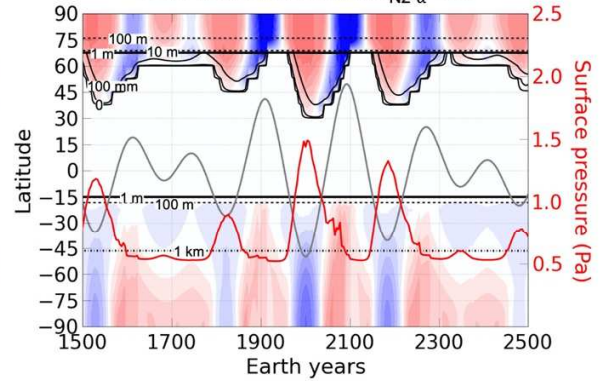
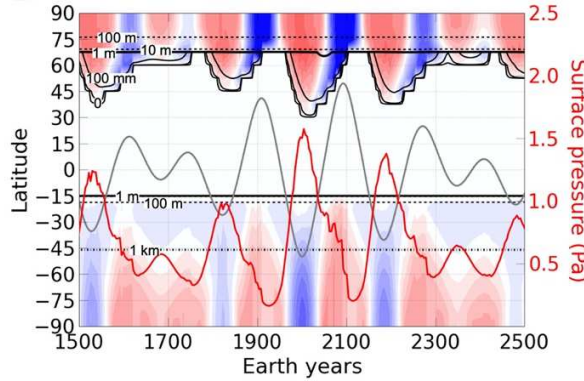
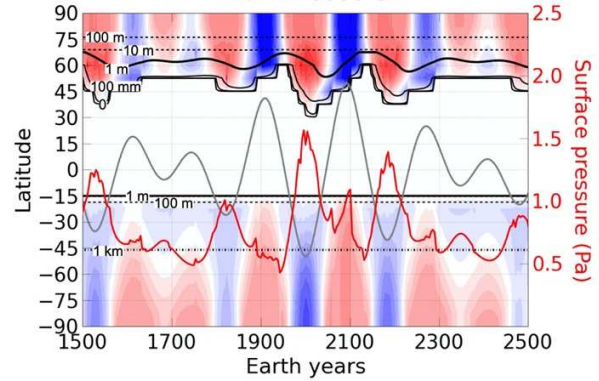
1235

1236 **Sensitivity to the N₂ ice emissivity**As detailed in Section 3.4.1, the N₂ ice emissivity on Triton
1237 may be lower than what is assumed in the model ($\epsilon_{N_2}=0.8$). Figure 19.A-B shows how the volatile
1238 cycle is impacted by a lower N₂ ice emissivity by comparing a reference simulation using a fixed
1239 emissivity $\epsilon_{N_2}=0.8$ with the same simulation but using $\epsilon_{N_2}=0.3$ and $\epsilon_{N_2}=0.5$. In addition, Figure 19.C
1240 shows the case of a temperature dependent N₂ ice emissivity, with an α - β phase transition for N₂
1241 ice at $T_{\alpha-\beta}=35.6$ K, as implemented in the model and tested for Pluto in Bertrand et al., 2019 (see
1242 their equation 1). In all these “low emissivity cases” (and as for all the other simulations of this

1243 section), the model had to adjust (increase by steps of 0.005, typically from 0.75 to 0.8) the N₂ ice
1244 albedo during the spin-up time so that the surface pressure remained close to 1.4 Pa in 1989.

1245 Overall, the fixed lower emissivity induce higher pressure minima, which remain above 0.4 Pa in
1246 the case with $\epsilon_{N_2}=0.3$. Together with the subsequent increase of N₂ ice albedo needed to match
1247 the Voyager 2 pressure constraint, it induces lower condensation-sublimation rates and a smaller
1248 northern cap.

1249 The cases with the α -transition are slightly different. The change of emissivity forces the ice
1250 surface temperature to remain at the transition temperature $T_{\alpha-\beta}=35.6$ K during the periods of low
1251 pressure (i.e., northern summers) and therefore the surface pressure during these periods also
1252 remains constant at ~ 0.5 Pa. However, ϵ_{N_2} remains at 0.8 during most of time, and therefore the
1253 condensation-sublimation rates and the extension and thickness of the northern cap do not
1254 change much compared to the reference case.

AReference run: $TI=2000$ SI, $R=350$ m, $\epsilon_{N_2}=0.8$, $A_{bed}=0.7$, $F=0$ mW m⁻²**B**With $\epsilon_{N_2}=0.5$ With $\epsilon_{N_2}=0.3$ **C**With α -transition and $\epsilon_{N_2-\alpha}=0.5$ With α -transition and $\epsilon_{N_2-\alpha}=0.3$ **D**With $TI=4000$ SIWith $TI=8000$ SI

1256 Figure 19: Sensitivity of the volatile cycle to low N₂ ice emissivity and high thermal inertia. (A)
 1257 Reference simulation among best-case runs, with the North-South asymmetry in N₂ ice albedo,
 1258 TI=2000 SI, $\epsilon_{N_2}=0.8$, showing the zonal and diurnal mean N₂ condensation-sublimation rate (mm
 1259 Triton day⁻¹) during the period 1500-2500 (about 7 seasonal cycles). The black contours indicate
 1260 the extent of the caps (0-line, 10 mm, 100mm, solid), and where the ice is 1 m (thick solid line)
 1261 and 1 km thick (dash-dotted line). The red line indicates the surface pressure (right y-axis) and
 1262 the grey line indicates the subsolar latitude. (B) As in (A) but with $\epsilon_{N_2}=0.5$ (left) and $\epsilon_{N_2}=0.3$ (right).
 1263 (C) As in (A) but with the α - β phase transition, $\epsilon_{N_2-\beta}=0.8$, $\epsilon_{N_2-\alpha}=0.5$ (left) and $\epsilon_{N_2-\alpha}=0.3$ (left). (D) As
 1264 in (A) but with TI=4000 SI (left) and TI=8000 SI (right).

1265

1266

1267 7.3.3. Best simulations matching observations

1268 As defined in Section 3.5, realistic simulations must be consistent with the volatile fractional area
 1269 retrieved from Earth-based spectroscopic observations, the relatively bright surface and the
 1270 extent of the caps seen by Voyager 2 in 1989, and the surface pressure of ~1.41 Pa retrieved by
 1271 stellar occultation in 2017 (all simulations match by construction the 1.4 Pa surface pressure
 1272 measured by Voyager 2 in 1989).

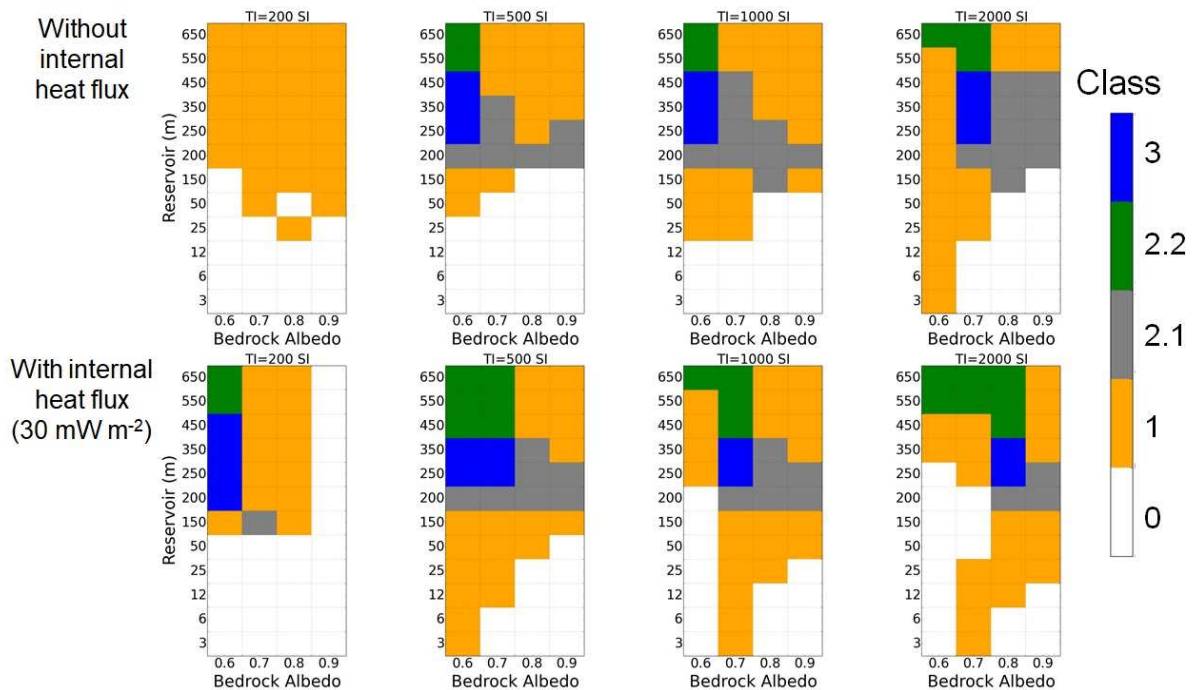
1273 Here we define four classes of simulations, summarized in Table 3. Simulations of Class #1 are
 1274 consistent with the observed surface pressure in 2017 (1.41 Pa, with 30% margin, i.e. ± 0.4 Pa)
 1275 and with a relatively bright surface Bond albedo ($A_{bed} \geq 0.6$). Note that all simulations of Class
 1276 #1 satisfy the constraint of having a full-disk averaged surface temperature of 37-44 K in 1989
 1277 (although this constraint is not stringent enough to distinguish between best-case simulations).
 1278 Simulations of Class #2.1 are of Class #1 and are in addition consistent with the volatile fractional
 1279 area observed in 1995 and 2010, with relatively large margins (we assume 45-75% for both 1995
 1280 and 2010). Simulations of Class #2.2 are also of Class #1, but are consistent with the extent of
 1281 the caps observed in 1989 by Voyager 2 (poleward of 45°N in the northern hemisphere and about
 1282 15°S in the southern hemisphere, with some margins on these values). Both Class #2.1 and Class
 1283 #2.2 require a more constrained surface pressure in 2017 of 1.41 Pa \pm 0.2 Pa. Finally, simulations
 1284 of Class #3 are the most realistic ones. They are of Class #1, #2.1 and #2.2. Here we only analyze
 1285 the simulations performed with the North-South N₂ albedo asymmetry (those without the
 1286 asymmetry can match Class #1 criteria but do not match any of the Class #2 criteria, as shown in
 1287 Section 7.2).

Class 1: Matching 2017 stellar occultations and surface albedo
Surface pressure in 2017: 1.41 \pm 0.4 Pa
Surface albedo (all ices, including bedrock) \geq 0.6 (relatively bright surface)
Class 2.1: Matching Earth-based spectroscopic observations
Must be of Class 1
Volatile fractional area within 45-75% in 1995 and in 2010
Surface pressure in 2017: 1.41 \pm 0.2 Pa
Class 2.2: Matching cap extents seen by Voyager 2
Must be of Class 1
Southern cap extent within 35°S-5°N in 1989
Northern cap extent poleward of 35° in 1989
Surface pressure in 2017: 1.41 \pm 0.2 Pa
Class 3: Best cases
Must be of Class 1, 2.1 and 2.2

1288

1289 Table 3: Classification of the simulations, based on the available observations and with some
1290 margins. Most realistic simulations are of Class #3.

1291



1292

1293 Figure 20: Classification of our simulations (with the North-South N₂ albedo asymmetry) without
1294 (top) and with (bottom) 30 mW m⁻² internal flux as defined by Table 3, with varying subsurface
1295 thermal inertia (columns, TI = 200, 500, 1000, and 2000 SI from left to right), N₂ global reservoir
1296 (y-axis) and bedrock albedo (x-axis). Best case simulations (Class #3) are shown in blue. Class
1297 0 does not meet any constraint.

1298

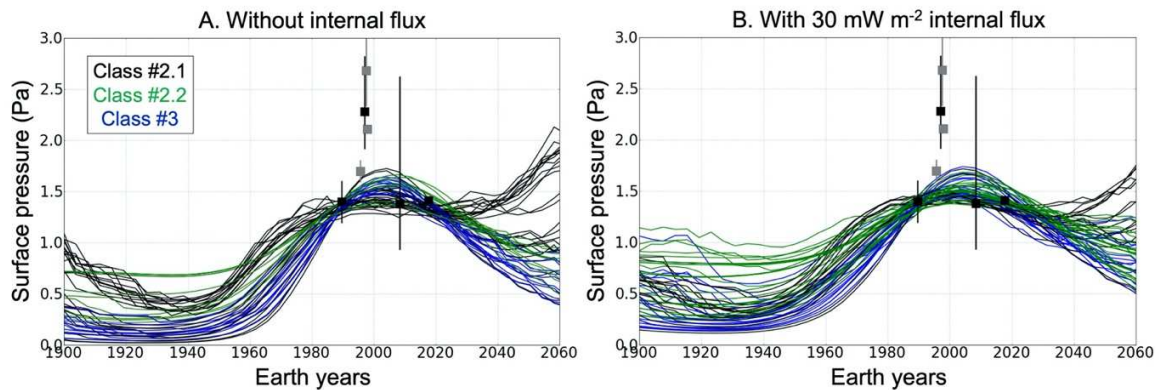
1299 Figure 20 shows the classification for all the simulations performed with the North-South N₂ albedo
1300 asymmetry. We note that:

1301 – All simulations performed with a low TI of 200 SI are generally of Class #0 or #1 because
1302 they are inconsistent with the extent of the caps seen in 1989 and with the observed
1303 volatile fractional area (too large), except for the cases with an internal heat flux, a large
1304 reservoir and a bedrock surface albedo of 0.6 (Classe #3).

1305 – The most realistic simulations in terms of surface pressure and N₂ ice distribution (extent
1306 in 1989 and fractional area in 1995-2010) have a bedrock albedo within 0.6-0.8 and a
1307 large N₂ ice reservoir greater than 200 m. In particular, the northern cap is confined to
1308 poleward of 45°N in 1989 for moderate bedrock albedo (< 0.8) and mid-to-high bedrock
1309 thermal inertia, while the southern cap extends to at least 30°S in 1989 for large N₂
1310 reservoirs (> 200 m). As a result, these simulations are of Class #2 (2.1 or 2.2) at least.

1311 – The fact that best case simulations are obtained for a bedrock albedo within 0.6-0.8 is
1312 consistent with Voyager 2 observations.

- 1313 – Simulations of Class #3 that closely match all observations listed in Table 3 are generally
 1314 obtained for mid-to-large reservoir (200-450m) coupled with (1) high thermal inertia (2000
 1315 SI) and a bedrock albedo of 0.7-0.8, or (2) intermediate thermal inertia (500-1000 SI) and
 1316 a bedrock albedo of 0.6-0.7, or (3) low thermal inertia (200 SI), a bedrock albedo of 0.6
 1317 and high internal heat flux.
 1318

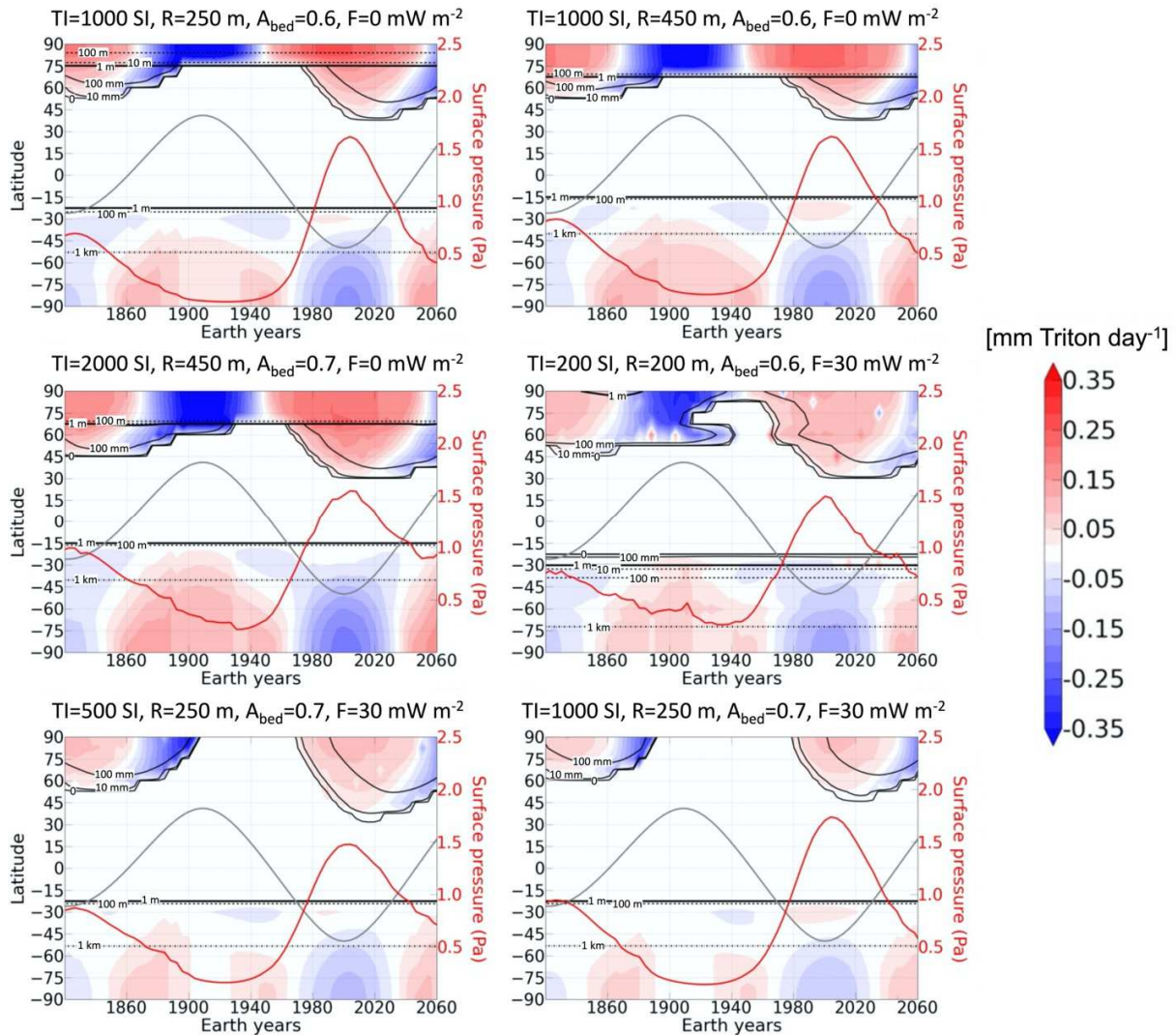


1319
 1320 Figure 21: Surface pressure from 1900 to 2060 as obtained in the best case simulations, Classes
 1321 #2.1 (black), #2.2 (green) and #3 (blue), without (A) and with internal heat flux (B). Black and grey
 1322 data points and error bars represent the pressure observations as presented in Table 2 (black are
 1323 for the data points that we consider are the strongest observational constraints).

1324
 1325 Figure 21 shows the evolution of surface pressure in the best case simulations. The evolution is
 1326 relatively similar for all these simulations: the surface pressure increases by a factor of 1.5-2
 1327 during the period 1980-2010, reaches a maximum of 1.5-1.8 Pa in ~2005-2010 and then
 1328 decreases to reach 1-1.5 Pa in the period 2020-2040 and 0.5-1 Pa by 2060.

1329 We note an increase in surface pressure between 2040-2060 in some Class #2.1 simulations.
 1330 This is due to the fact that the seasonal northern cap is strongly extended (equatorward) in these
 1331 simulations around year 2000, following a large accumulation of deposits at low latitude during
 1332 southern summer. As a result, when the subsolar point moves northward (close to 0° in 2040-
 1333 2060), there are large amounts of N₂ ice available for sublimation (at the equator and mid-
 1334 latitudes) and sublimation tends to dominate condensation (at the poles) in global average,
 1335 causing an increase in surface pressure.

1336
 1337
 1338
 1339



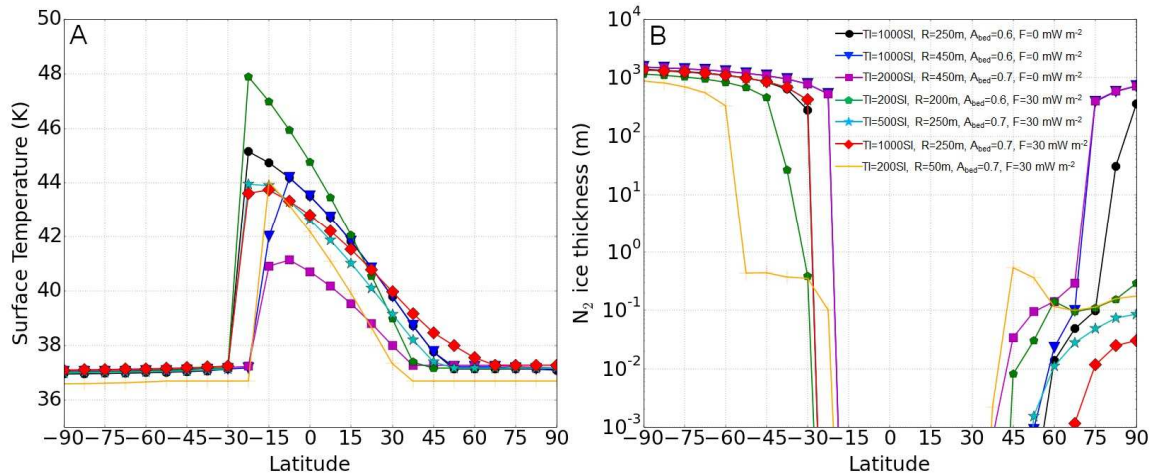
1340

1341 Figure 22: Best case simulations with the North-South asymmetry in N_2 ice albedo. Zonal and
 1342 diurnal mean N_2 condensation-sublimation rate ($\text{mm Triton day}^{-1}$) during the period 1820-2060.
 1343 The black contours indicate the extent of the caps (0-line, 10 mm, 100mm, solid), and where the
 1344 ice is 1 m (thick solid line) and 1 km thick (dash-dotted line). The red line indicates the surface
 1345 pressure (right y-axis) and the grey line indicates the subsolar latitude. Deposits thinner than 1 m
 1346 tend to be seasonal.

1347

1348 Figure 22 shows the seasonal evolution of the N_2 condensation-sublimation rates for six of the
 1349 best-case (class #3) simulations, while Figure 23 shows the latitudinal distribution of ice and
 1350 surface temperatures as obtained for 1989 for the same simulations. The modeled southern cap
 1351 is permanent and extends to $\sim 15^\circ\text{S}$, with low latitudes being dominated by sublimation, but
 1352 replenished in N_2 ice by viscous glacial flow. All best simulations suggest a southern cap that is
 1353 >1 km thick poleward of 60°S . A small permanent northern polar cap is suggested for best-case
 1354 simulations without internal heat flux, while only a seasonal northern cap is suggested for best-
 1355 case simulations with 30 mW m^{-2} internal heat flux. In all simulations, the northern cap extends at
 1356 least to 45°N in the period 2020-2040, and to $\sim 30^\circ\text{N}$ in some cases. At the southern summer

1357 solstice, the sublimation and condensation rates are about $\sim 0.1\text{-}0.2$ mm per Triton day (i.e. $2\text{-}4 \times 10^{-7}$ mm s $^{-1}$), and about 0.13-0.26 m if applied over 20 Earth years. Simulations performed
 1358
 1359 with a high internal heat flux ($F=30$ mW m $^{-2}$) show reduced N₂ condensation-sublimation rates due to the higher N₂ ice albedo ($\sim 0.05\text{-}0.15$ mm per Triton day), and smaller permanent caps. In
 1360
 1361 all cases, N₂ recondenses in the low latitudes of the southern hemisphere during the period 1980-
 1362
 1363 2020. Sublimation from the polar southern cap and condensation at the northern edge was also
 1364 suggested by the thermal balance model of Grundy et al. (2010) and could help explain the longitudinal variation of the N₂ 2.15 μ m feature.



1365
 1366 Figure 23: (A) Zonal mean surface temperature vs latitude for the best-case simulations in 1989,
 1367 as shown by Figure best_flux1: Without internal heat flux : TI=1000 SI - R=250 m - A_{bed}=0.6 (black
 1368 circle), TI=1000 SI - R=450 m - A_{bed}=0.6 (blue triangle), TI=2000 SI - R=450 m - A_{bed}=0.7 (purple
 1369 square). With internal heat flux: TI=200 SI - R=200 m - A_{bed}=0.6 (green polygon), TI=500 SI -
 1370 R=250 m - A_{bed}=0.7 (cyan star), TI=1000 SI - R=250 m - A_{bed}=0.7 (red losange). The orange solid
 1371 line shows the cases of a low reservoir and low thermal inertia simulation (TI=200 SI - R=50 m -
 1372 A_{bed}=0.7 - F=30 W m⁻²) that is consistent with observed caps extent and volatile fractional area
 1373 but inconsistent with the observed pressure in 2017 (too low, see text in Section 8.3). (B). Same
 1374 as A but showing the surface N₂ ice thickness.

1375 7.4 On the seasonal cycle of CO and CH₄

1376 Our results show that CO and CH₄ remain mixed with N₂ and never form pure deposits (except
 1377 for pure CH₄ frost residuals forming at the cap edge when N₂ ice sublimates and disappears, but
 1378 these frosts quickly disappear within one Earth years or less). This contrasts with Pluto, where
 1379 CH₄-rich ice deposits cover a large part of the surface (thick and permanent deposits in the
 1380 equatorial regions, seasonal frosts or permanent mantle at mid-to-polar latitudes). This may be
 1381 due to a difference in the global reservoir of CH₄ ice (which may be too small on Triton to form
 1382 permanent CH₄-rich deposits). Another basic understanding of the absence of broad permanent
 1383 CH₄-rich deposits on Triton is the following: on Pluto, N₂ and CH₄ ices tend to accumulate in the
 1384 equatorial regions, which are colder than the mid-to-high latitudes, in average over a Pluto year
 1385 and over several astronomical cycles, due to the relatively high obliquity of the spin axis (e.g.,
 1386 Bertrand et al., 2019). Whereas N₂ ice preferably accumulates in depressions, CH₄ ice preferably
 1387 accumulates at high altitude (e.g., Bertrand and Forget, 2016, Bertrand et al., 2020b). The fact
 1388 that the equatorial regions on Pluto correspond to a large area displaying a variegated
 1389 topography, including deep depressions (such as the $\sim 6\text{-}10$ km deep Sputnik Planitia impact
 1390 crater) and tall mountains (e.g. Pigafetta Montes, or the region of Tartarus dorsa) allows the

1391 formation of both permanent N₂-rich (Sputnik Planitia ice sheet) and CH₄-rich (bladed terrain)
1392 deposits at different locations. On Triton, however, the coldest regions are the poles (maybe one
1393 pole in particular if one assumes an asymmetry in internal heat flux for instance), which
1394 correspond to a relatively small area where only small variations in topography may be displayed,
1395 thus not allowing the formation of both deposits (instead, the ice mix together at the poles).

1396 Although we do not expect broad and thick CH₄-rich ice deposits to form on Triton, the formation
1397 of small and transitory CH₄-rich ice patches in our model may be limited by the spatial resolution
1398 used or the different assumptions made regarding the behavior of ice mixtures. Here we tested
1399 different scenarios for CO and CH₄ and describe the model predictions of CO and CH₄
1400 atmosphere mixing ratios, and compare to observations. The various observations of CO and CH₄
1401 surface ice and atmosphere mixing ratios are summarized in Section 2.3 and Section 2.5,
1402 respectively.

1403 7.4.1. The CO seasonal cycle

1404 In our model, when we impose a constant CO ice mixing ratio of 0.04% (respectively 0.08%) into
1405 N₂ ice and we assume that the vapour pressure equilibrium is controlled by Raoult's law, we
1406 obtain a mean CO gas volume mixing ratio of 0.006% (respectively 0.012%) during the period
1407 2000-2020, in good agreement with the 2017 ALMA mm-observations (Gurwell et al. 2019), and
1408 therefore inconsistent with the 10x higher IR-derived value from Lellouch et al. (2010). The limited
1409 seasonal variation is due to the volatility of CO being close to that of N₂ and the absence of CO-
1410 rich ice deposits (Tegler et al., 2019, and absent on Pluto's surface as well, Bertrand and Forget
1411 2016, Schmitt et al., 2017). In the model, CO tends to follow N₂ and condenses where N₂-rich
1412 deposits are already present. This is consistent with ground-based spectroscopic data of Triton
1413 (CO follows N₂ in longitude) and with observations of Pluto's surface by New Horizons. According
1414 to our model, the CO gas volume mixing ratio should remain very close to these values in the
1415 next decades (with a slight decrease in 2040 to 0.005% and 0.01%, respectively), although small
1416 variations in the CO gas volume mixing ratio are possible if the surface of some areas becomes
1417 enriched or depleted in CO ice as N₂ sublimates or condenses.

1418 7.4.2. The CH₄ seasonal cycle

1419 As detailed in Section 2.5, the observed CH₄ atmospheric mixing ratio is much larger (by three
1420 orders of magnitude) than expected for an ideal mixture, i.e. if CH₄ ice only exists on Triton as
1421 CH₄ diluted in a N₂-rich solid solution (Stansberry et al. 1996b), or for an intimate mixture. Instead,
1422 using the CH₄ patch model of Stansberry et al. (1996b), Merlin et al., 2018 (respectively, Quirico
1423 et al., 1999) estimated that CH₄-rich ice (at ~40 K) covered 2-3% in 2010-2013 (respectively, a
1424 maximal value of 10% in 1995) of the visible disk of Triton, which could be sufficient to maintain
1425 a CH₄ atmospheric volume mixing ratio around 0.03%, as observed by Voyager 2.

1426 We tested this scenario in one of our reference simulations (TI=2000 SI, R=400 m, A_{bed}=0.6) by
1427 imposing pure CH₄ ice deposits on Triton's surface (with a fractional area consistent to the
1428 observations of Quirico et al., 1999 and Merlin et al., 2018), assuming that they follow Raoult's
1429 law and are a proxy for CH₄-rich ice (this assumption is good enough, as described in Young et
1430 al., 2021). We tested two different locations for these deposits:

1431 (1) At the edges of the southern cap, thus forming a latitudinal band of CH₄ ice near the
1432 equator, with a fractional area of ~5% of the projected disk as seen from Earth at the time
1433 (~2010) of the observations of Merlin et al. (2018): these regions should contain seasonal
1434 volatile frosts, which would favor the formation of CH₄-rich ice by segregation as N₂ ice
1435 sublimates and disappears. Voyager 2 images showed features in these regions

1436 suggestive of intense N₂ ice sublimation, which could lead to an enrichment in CH₄-rich
1437 ice on the surface.

1438 (2) At the south pole (~2% of the disk surface seen from Earth in 2010): our simulations show
1439 that the N₂ ice sublimation rates are strongest at the south pole, which could favor the
1440 formation of CH₄-rich deposits on top of the surface.

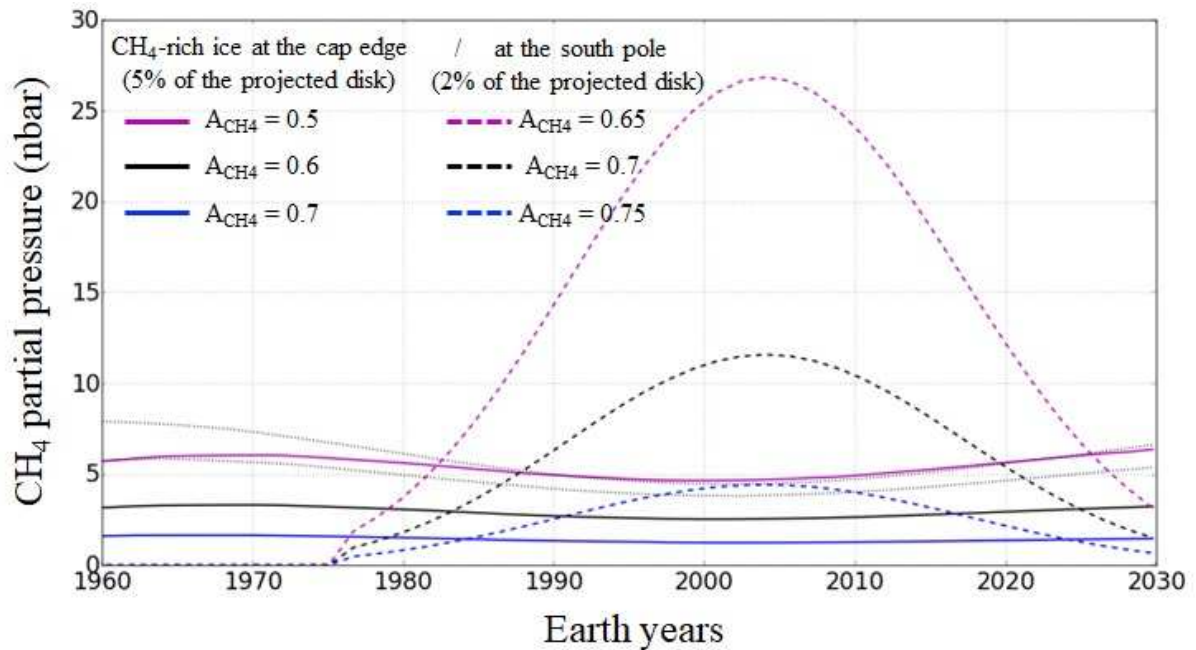
1441 Figure 24 shows the seasonal evolution of the global mean mixing ratio of atmospheric CH₄ over
1442 time for both scenarios, and assuming different albedos for the pure CH₄ ice. Note that the
1443 evolution of the surface pressure remains relatively unchanged for all cases compared to that in
1444 the reference simulation (without CH₄-rich ice).

1445 The simulations with CH₄-rich ice at the cap edge produce a CH₄ partial pressure of 1-5x10⁻⁴ Pa
1446 in 1989, which is consistent with the 2.45x10⁻⁴ Pa observed by Voyager 2 (Figure 24, solid lines).
1447 Slightly larger amounts can be obtained with a lower CH₄ ice albedo and a higher surface CH₄ ice
1448 coverage (solid grey lines). The simulations with CH₄-rich ice at the south pole produce an
1449 increase in CH₄ partial pressure until 2005, followed by a decrease as the south pole exits polar
1450 day (Figure 24, dashed lines). A small fraction of the south pole covered by CH₄-rich ice is
1451 sufficient to produce a CH₄ partial pressure of a few nbar, as observed. The simulation including
1452 a CH₄-rich patch at the south pole with albedo of 0.7, is particularly promising to explain the factor
1453 of 4 (2.45 to 9.8x10⁻⁴ Pa) increase in the CH₄ partial pressure from 1989 to 2009, as reported by
1454 Lellouch et al. (2010). In contrast, the models in which CH₄-rich ice is concentrated at the N₂ cap
1455 edge do not reproduce this increase in the CH₄ atmospheric abundance over 1989-2009.
1456 However, a decrease in CH₄ ice albedo or increase in CH₄ ice coverage during this period can
1457 also explain the observed increase in CH₄ partial pressure. It is possible that both the pole and
1458 cap edge become enriched in CH₄ ice, with different amounts and timescales.

1459 Note that here we assume that these modeled CH₄-rich deposits, exposed at the surface once N₂
1460 ice locally disappeared, are permanent during southern summer. If CH₄ ice also disappears from
1461 the surface, the CH₄ atmospheric mixing ratio would slowly fall back to the levels expected for an
1462 ideal mixture (a few 10⁻⁵ %).

1463 Also note that the relatively low CH₄ atmospheric mixing ratio observed (~0.03%) and simulated
1464 (>0.01%), would still be enough to block most of the incoming Lyman-α radiation (121.6 nm, 10.19
1465 eV) from direct sunlight and from backscattering from the interplanetary medium, which has
1466 implication for the direct photolysis and subsequent darkening of the ices on the surface.

1467



1468

1469 Figure 24: Global mean CH_4 partial pressure (nbar, or $\times 10^{-4}$ Pa) over time, as obtained for the
 1470 simulation $\text{TI}=2000$ SI, $R=450$ m, $A_{\text{bed}}=0.6$, with CH_4 -rich ice at the cap edge (fractional area of
 1471 5% of the visible disk in 2010, solid lines) and at the south pole (2% of the visible disk, dashed
 1472 lines), for different CH_4 ice albedos. The two grey curves are for a simulation with CH_4 -rich ice at
 1473 the cap edge (and $A_{\text{CH}_4}=0.6$, as for the solid black curve) but covering 9% and 12% of Triton's
 1474 visible surface area, respectively.

1475 8. Discussion

1476 8.1. On the formation of a northern (polar) cap

1477

1478 All long-term simulations performed in Section 5 with North-South asymmetries in internal heat
 1479 flux, topography, and N_2 ice albedo, along with a global N_2 ice reservoir of 300 m, predict the
 1480 formation of a permanent N_2 (polar) cap in the northern hemisphere (>100 m thick). Most of the
 1481 best-case simulations (Class #1 to #3) performed in Section 7 also predict a permanent N_2 cap in
 1482 the northern hemisphere. The northern cap is much smaller and thinner in the best-case
 1483 simulations performed with an internal heat flux of 30 mW m^{-2} , due to the warmer subsurface. A
 1484 few results with intermediate thermal inertia and moderate global N_2 reservoir ($\text{TI}=1000$ SI,
 1485 $R=250\text{-}350$ m, $A_{\text{bed}} = 0.6$) predict no permanent cap. The northern cap is not permanent if a
 1486 smaller global N_2 ice reservoir (< 250 m) is used along with large North-South asymmetries (see
 1487 Figure 13, $R=200$ m, and $\Delta A_{\text{N}_2} = 0.1$). However, these low-reservoir simulations are not consistent
 1488 with the available observations.

1489 The formation of a permanent N_2 northern cap is primarily the result of two effects:

1490 1. The northern polar night is long enough so that surface temperatures of the bedrock drop below
 1491 34 K for a bedrock surface albedo of 0.6. Consequently, N_2 condensation is easily triggered at
 1492 the north pole if the surface pressure becomes higher than the pressure at solid-gas equilibrium
 1493 (e.g., ~ 1 Pa at 37 K).

1494 2. In the simulations, N₂ ice flows (slowly, on timescales longer than the seasonal timescales)
1495 from the southern cap towards the warmer sublimation-dominated mid-to-low latitudes, thus
1496 maintaining large amounts of ice in these regions, supplying N₂ for further sublimation and
1497 allowing the surface pressure to exceed that at solid-gas equilibrium at the north pole.

1498 Note that all best-case simulations explored predict that N₂ condensation has been occurring in
1499 the northern hemisphere since 1980. They show that at least a seasonal deposit of a few mm of
1500 N₂ ice was covering the northern polar latitudes in 1989 and should cover the northern latitudes
1501 down to 30°N-45°N in the period 2010-2030 (see Figure 22). In general, the current extent of the
1502 northern cap is related to the extent of the southern cap by the surface pressure: a large extent
1503 of the northern cap down to 30°N-45°N (i.e., a large condensation-dominated area) is only
1504 possible if the southern cap remains extended to at least 15°S (i.e., a large sublimation-dominated
1505 area) during this period, and a smaller southern cap would imply little to no N₂ deposits in the
1506 northern hemisphere, otherwise northern condensation would largely dominate southern
1507 sublimation and the surface pressure would have significantly dropped in 2017 to levels
1508 inconsistent with observations. The scenario of a large permanent southern cap and the seasonal
1509 appearance of N₂ ice deposits in the northern hemisphere below the terminator could also explain
1510 the increase in N₂ band absorption observed with SpeX/IRTF during the period 2002-2020 (Holler
1511 et al., 2016, 2020).

1512 8.2. On the evolution of surface pressure during the period 1989-2017

1513

1514 All best-case simulations show the same trend for the evolution of surface pressure, with an
1515 increase from 1920 to 2005-2010 (shortly after the southern summer solstice) followed by a
1516 decrease back to the 1920 levels in 2080.

1517 Our results do not suggest a strong surge in surface pressure, as it has been reported for the
1518 period 1995-1997 (e.g., Elliot et al., 2000). During the 1989-2005 period, our best-case class #3
1519 simulations suggest an increase in surface pressure by a factor of 1.1-1.2 only, with a peak around
1520 1.5-1.7 Pa. Some of the Class #1 simulations show a peak in surface pressure reaching 2.3 Pa,
1521 i.e. a factor of 1.6 compared to the Voyager 2 epoch (these simulations typically predict a 2017
1522 surface pressure that is above the 1.41±0.2 Pa constraint, not shown). These values are
1523 consistent with the 1995 occultation event and the derived pressure reported by Olkin et al.
1524 (1997), and also eventually with the 1997 occultation event and the derived pressure reported by
1525 Marques Oliveira et al. (2021), although the simulations only match this latter value at the 1 σ
1526 significance level. However, they are inconsistent with the higher values reported in 1997 (Elliot
1527 et al., 2000, 2003). We note that a reanalysis of some of these data indicates that this pressure
1528 increase was not significant at the 3- σ level (Marques Oliveira et al., 2021). Such a strong increase
1529 in surface pressure could still have occurred if processes not taken into account in our model play
1530 an important role on Triton, such as strong surface albedo feedback for instance.

1531 8.3. On the presence of volatile ice at the south pole

1532

1533 As detailed in Section 2.3, ground-based spectroscopy of Triton's surface performed with
1534 IRTF/SpeX in 2002-2014 and VLT/SINFONI in 2010-2013 showed little longitudinal variability for
1535 CO₂ and H₂O ice, unlike the three volatile ices N₂, CH₄, CO (Grundy et al. 2010, Holler et al.,
1536 2016, Merlin et al., 2018). To explain these observations, it has been suggested that CO₂ and
1537 H₂O ices are exposed at the south pole (the very southernmost latitudes, roughly 90°S-60°S),
1538 which would be bare of volatile ice (Grundy et al. 2010, Holler et al., 2016).

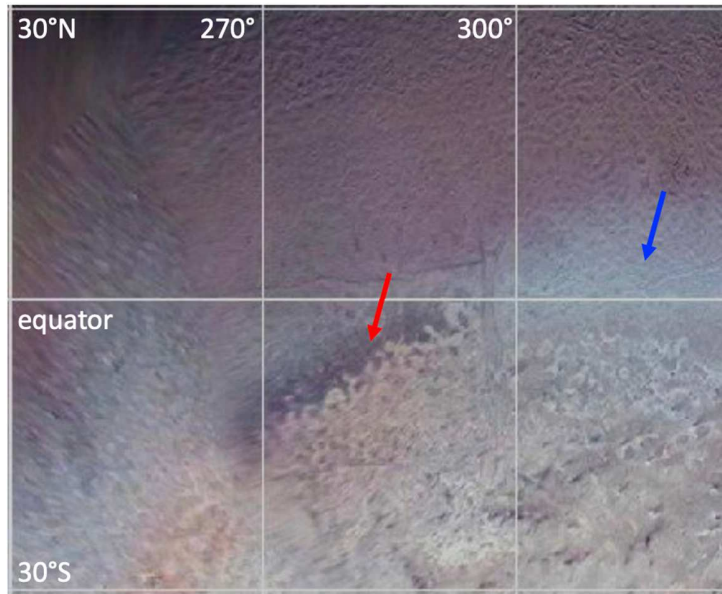
1539 However, our volatile transport model challenges this scenario since it always predicts a
1540 permanent cap at the south pole, except if an extremely low N₂ reservoir, i.e. only seasonal frosts,
1541 is assumed, but these simulation cases typically present (at least for moderate to high thermal
1542 inertias) a too low surface pressure in 2017 (< 1.41 Pa, Figure 16), a low volatile fractional area
1543 (< 40%, Figure 15) and a southern cap extent poleward of 45°S in 1989 (Figure 14). Our model,
1544 and its current modeled physical processes, cannot predict such a “hole” in volatile ice at the
1545 south pole (90°S-60°S). Physical processes not taken into account in the model may play an
1546 important role to mask the detection or completely remove N₂ ice at the south pole (see model
1547 uncertainties in Section 8.7). For instance, the predicted sublimation of 30-50 cm of N₂ ice at the
1548 south pole during the period 1970-2000 (Figure 11, Figure 22) could have led to an accumulation
1549 of CH₄-rich ice at the south pole could mask the detection of N₂ ice and be a possible scenario,
1550 although it would imply a relatively large CH₄-rich-covered area that would remain to be consistent
1551 with other observations.

1552 The near-IR VLT/SINFONI observations and subsequent modeling of Merlin et al. (2018) showed
1553 that CO₂ ice is actually present in the form of very small grains and has two components (see
1554 their Table 9), one in which it is mixed into the N₂:CH₄:CO matrix (unit 1) and another in which it
1555 is mixed into H₂O ice (unit 2). These results suggest that CO₂ ice is present almost everywhere
1556 (with an equivalent area of 50% and very small grains). In addition, their model suggests that H₂O
1557 ice is present in unit 2 only (H₂O+CO₂+CH₄-rich) and does not need to be invoked in unit 1
1558 (N₂:CH₄:CO). Based on these results, Merlin et al. (2018) imagined two scenarios that could
1559 reconcile the presence of both N₂ and CO₂ ices at the south pole: (1) A bedrock surface (CO₂ ice)
1560 covered by small CO₂ grains (regolith) covered by a transparent N₂-based matrix (allowing CO₂
1561 to stay detectable), and (2) Small CO₂ particles on top or inside the N₂-based matrix, as the result
1562 of endogenous processes (e.g. active geysers tearing particles of CO₂ from the bedrock, transport
1563 and spatial redistribution of these particles by the winds, and deposition onto the surface).

1564 Our model results are consistent with these two scenarios, since they do not prevent N₂ ice to be
1565 present at the south pole. However, in general, it remains difficult to be confident on the
1566 composition of Triton’s south pole, given the limited amount of observational datasets, the relative
1567 simplicity of the VTM, and the large number of model parameters in both the VTM and the near-
1568 IR spectra analysis models.

1569 8.4. On the different terrains observed at the cap edge by Voyager 2

1570



1571
 1572 Figure 25: Equatorial regions on Triton at longitudes 240°E-330°E displaying alternation of
 1573 relatively bright blue frosts (blue arrow, 240°E-270°E and 300°E-330°E) and relatively dark
 1574 terrains without blue frost (red arrow, 270°E-300°E) at the edge of the southern cap.

1575
 1576 Figure 25 highlights two different terrains observed in the equatorial regions at the cap edge: (1)
 1577 a relatively bright blue (or less red) surface, with photometric properties consistent with a freshly
 1578 deposited frost (McEwen, 1990); this terrain is seen at almost all longitudes and forms a fringe at
 1579 the cap edge (Figure 2), and (2) a relatively dark surface, without much blue frost, around 270°E-
 1580 300°E.

1581 We hypothesize that this dark terrain is the result of a high concentration of dark materials (e.g.
 1582 tholins-like haze deposits and/or irradiated ices) that had been mixed in N₂ ice and have now
 1583 been revealed at the surface as the N₂ ice sublimates away. The composition of this unit may be
 1584 similar to some degree to the dark N₂ ice plains located at the northern edge of Sputnik Planitia
 1585 on Pluto, which are enriched in dark materials and in CH₄ ice due to intense N₂ ice sublimation
 1586 (White et al., 2017). The fact that this unit on Triton may be enriched in CH₄ ice is consistent with
 1587 IRTF/SpeX observations, which show a peak absorption for CH₄ near ~290°E and also a
 1588 maximum of shift in the position of the CH₄ bands indicating an increased amount of CH₄-rich ice.
 1589 However, these observations are for the period 2002-2014 only (Grundy et al., 2010, Holler et al.,
 1590 2016). We also note that the formation of this dark terrain on Figure 25 could be related to
 1591 topography (see Section 8.5).

1592 This observed longitudinal asymmetry in CH₄ ice distribution could suggest the presence of CH₄-
 1593 rich deposits at the cap edge, rather than at the south pole. Our simulations with CH₄-rich ice at
 1594 the cap edge could explain the fourfold increase in CH₄ partial pressure from 1989 to 2009
 1595 reported by Lellouch et al. (2010) if the CH₄ ice albedo significantly lowered or if the CH₄ ice
 1596 surface coverage significantly increased during this period. The latter would also be consistent
 1597 with the observed increase in CH₄ band absorption during the period 2002-2020 (Holler et al.,
 1598 2016, 2020). It should be noted that such a scenario of a variable-width ring of segregated less-
 1599 volatile ice surrounding retreating volatile seasonal deposits has already been observed on Mars
 1600 in the analogue case of water ice trapped in seasonal CO₂ ice deposits (Appéré et al. 2011). On

1601 Mars, this moving ring also triggers a strong seasonal increase in water vapor during its
1602 sublimation (e.g. Pankine et al., 2009, 2010).

1603 Our simulations with CH₄-rich ice at the south pole also explain the fourfold increase in CH₄ partial
1604 pressure (suggested for the period 1989-2009) as being driven by insolation changes. However,
1605 it remains unclear how CH₄-rich ice would form there in the first place. The surface composition
1606 of the south pole on Triton in 1989 could also be comparable to the northern dark plains of Sputnik
1607 Planitia on Pluto in 2015, since these plains correspond to thick N₂ ice deposits experiencing the
1608 constant insolation of the polar day, as Triton's south pole. In Sputnik Planitia, the plains display
1609 darker N₂-rich ice deposits enriched in CH₄ ice. The permanent and cold N₂ ice layer located there
1610 may buffer the increase of surface temperatures and limit the formation of CH₄-rich deposits on
1611 top of the ice layer. On Pluto, CH₄-rich ice is mostly detected outside Sputnik Planitia, with more
1612 spatial variability in the CH₄:N₂ mixture at mid latitudes, where thinner seasonal deposits are found
1613 (Schmitt et al., 2017). By analogy, on Triton, CH₄-rich ice may tend to form primarily at mid-to-
1614 equatorial latitudes where volatile ice deposits are thinner, and at the cap edge where the deposits
1615 are seasonal.

1616 The bright "blue" surface may be freshly deposited N₂ frost (relatively clean ice, hence the less
1617 red color). Our model suggests that N₂ recondenses in the equatorial regions after 1980 (and until
1618 2020, Figure 22). This happens only if the exposed "bedrock" locally has a high surface albedo
1619 or if N₂ ice is already present or was recently present in these regions; in the latter case the
1620 exposed "bedrock" surface would have remained cold enough to permit N₂ recondensation. The
1621 locations of this hypothetical blue N₂ frost are relatively consistent with IRTF/SpeX observations,
1622 which show a minimal (respectively maximal) N₂ absorption roughly where the combined extent
1623 of the cap and of the blue fringe is minimal (respectively maximal). The formation and expansion
1624 of this frost would also be consistent with the observed increase in N₂ band absorption during the
1625 period 2002-2020 (Holler et al., 2016, 2020).

1626 Alternatively, the bright "blue" surface could be made of freshly-condensed CH₄-rich ice. As
1627 detailed in Section 2.3, the amount of CH₄ ice that is not diluted in N₂ ice is estimated to cover a
1628 relatively small area on Triton's surface: 2–3% of the surface projected on the visible disk in 2010
1629 (Merlin et al., 2018) and a maximum of 10% in 1995. The blue fringe roughly covers a latitudinal
1630 band of 15° at the equator, which accounts for ~10% of the disk-projected surface, so exposed
1631 CH₄-rich frost at the location of the blue fringe would remain in the range of possible values
1632 (although close to the highest possible value) consistent with surface spectroscopic observations.
1633 Would there be enough gaseous CH₄ in the atmosphere to permit CH₄ condensation onto the
1634 surface in the equatorial regions? We can estimate the saturation vapour pressure volume mixing
1635 ratio of CH₄ (above a volatile-free surface) by using equation 14 in Forget et al. (2017), derived
1636 from the thermodynamic relations computed by Fray and Schmitt (2009). For a surface
1637 temperature of 38 K, 39 K, 40 K and 41 K (i.e. slightly warmer than N₂ ice in 1989), we find a CH₄
1638 saturation volume mixing ratio of 0.017%, 0.036%, 0.075% and 0.153% respectively.
1639 Consequently, a volume mixing ratio of CH₄ of ~0.03% (measured by Voyager 2 in 1989) would
1640 permit condensation onto a surface colder than ~39 K.

1641 However, the hypothesis of CH₄-rich frost for the blue fringe faces three main issues: (1) In our
1642 model, the bedrock surface temperatures in 1989 in the equatorial regions at the cap edge are
1643 relatively warm at ~42-44 K and become colder than 39 K in the terrains poleward of 30°N
1644 (bestsurf1989), which is not consistent with a blue fringe made of freshly-condensed CH₄. We
1645 note that CH₄ condensation could still be favored at the cap edge by locally enhanced winds or if
1646 the bedrock surface is locally colder than modeled (e.g. with a higher albedo). (2) A CH₄ ice
1647 composition of that region does not match well the longitudinal trends seen in the near-IR spectra.
1648 (3) The scenario of a CH₄ ice deposit left after N₂ sublimation is not likely, as the remaining deposit

1649 would also contain a certain amount of tholins-like dark materials and therefore would not appear
1650 less red (i.e. cleaner) than the surrounding terrains.

1651 Finally, on Pluto, it has been shown that albedo and composition positive feedback could further
1652 increase local contrasts in ice sublimation/condensation rates, which could explain the transition
1653 from bright to dark plains in Sputnik Planitia (Earle et al., 2018, Bertrand et al., 2020a). Such
1654 processes may also be operating on Triton and could explain the diversity of terrains and colors
1655 observed at the cap edge. For instance, N₂ sublimation and the subsequent darkening of the
1656 surface would lead to an amplifying positive feedback by increasing the absorption of incoming
1657 radiation and thus the sublimation rate, whereas N₂ condensation and the subsequent brightening
1658 of the surface would lead to further condensation.

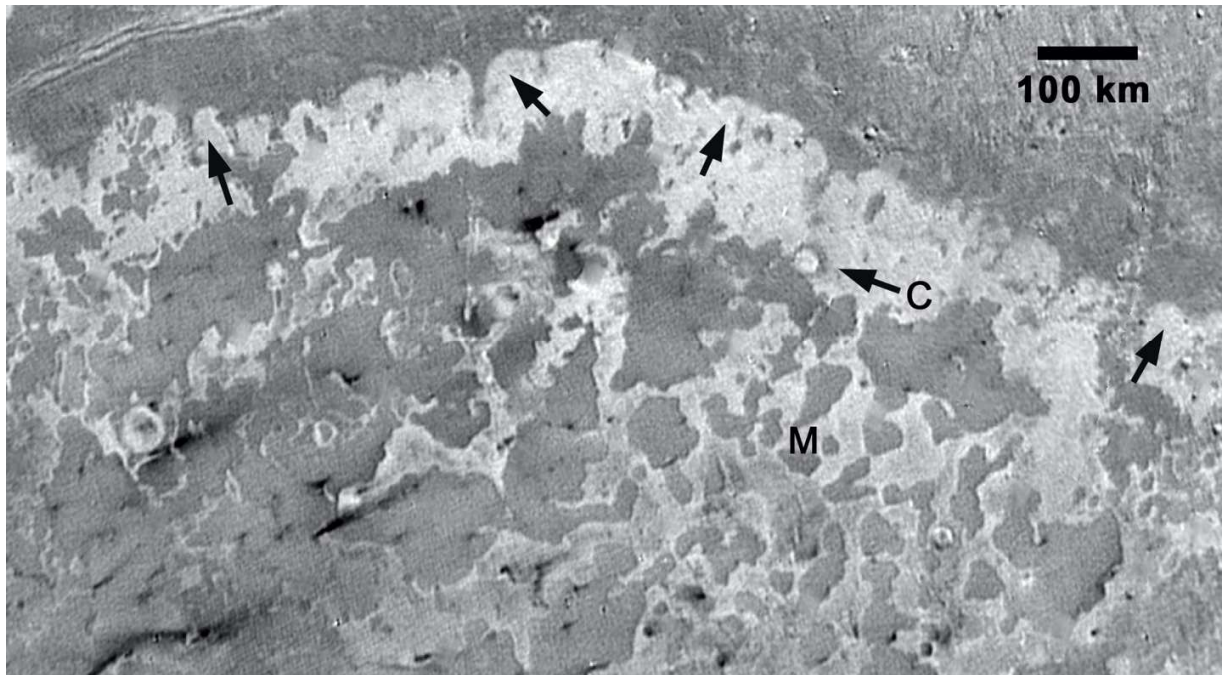
1659 8.5. On the topography and N₂ ice thickness in the southern hemisphere

1660

1661 Our best-case simulations have been obtained with a relatively large global reservoir of N₂ ice
1662 (>200 m), and suggest a thick southern cap (> 1 km at the south pole, > 100 m at the mid-latitudes
1663 and > 1 m at the equator, balanced by glacial flow). Interestingly, some simulations performed
1664 with a low bedrock thermal inertia of 200 SI have been able to produce a southern cap extended
1665 to the equatorial regions in 1989 with a lower N₂ global reservoir in the range 20 m - 200 m,
1666 leading to N₂ ice thickness of 0.1-1 m in the equatorial to mid-latitude regions and >100m at the
1667 south pole (Figure 14, and see solid orange line on Figure 23). In these simulations, the equatorial
1668 to mid-latitude deposits are not balanced by glacial flow (i.e., they are not connected to the polar
1669 deposits) but remain permanent due to the relatively cold bedrock, although in some of these
1670 cases a thin mid-latitude band of N₂ ice entirely sublimates in the period 2030-2050. However,
1671 these simulations with low bedrock thermal inertia are not among our best-case simulations (they
1672 are only of Class #1 at best), see Figure 20), mostly because they predict N₂ ice deposits in the
1673 northern hemisphere extending from 90°N to at least 30°N in 1989 (due to the colder surface
1674 induced by lower thermal inertia, Figure 14), and consequently a surface pressure in 2017 much
1675 lower than the reported value of 1.41 Pa.

1676 In general, the relatively coarse spatial resolution of Voyager 2 images and the lack of useful
1677 topography data above the southern cap do not allow us to determine with confidence the order
1678 of magnitude of the thickness of the bright southern deposits, which makes it difficult to conclude
1679 on the nature (less than 1 m thick seasonal vs. more than 1 m thick permanent) of these large-
1680 scale deposits. The spatial resolution also does not allow us to determine if glacial flow has
1681 occurred or not. However, the sharp dichotomy between the southern and northern terrains
1682 suggests that the northern bright deposit boundary is controlled by topography, possibly by a
1683 topographic barrier (e.g., scarps) of ~100 m to several 100 m (Figure 26), which reinforces our
1684 best-case model results suggesting thick and permanent volatile ice deposits in these regions.

1685



1686

1687 Figure 26: Enlargement of global cylindrical map showing macular southern terrains near the
 1688 equator of Triton. Possible example of a topographic barrier in the form of scarps (arrows),
 1689 possibly ~100 m to several 100 m in height, along the sharp dichotomy between the bright
 1690 southern and northern terrains seen by Voyager 2. "M" denotes a region of mesas south of the
 1691 main boundary. "C" shows a possible, partially buried crater. Image center ~15°S, 0°E. North is
 1692 up.

1693

1694 Finally, the sigmoidal contact line of the edge of the dark terrain in Figure 25 seems to be related
 1695 to topography (Paul Schenk, personal communication). This region forms the southwestern extent
 1696 of the known region of cantaloupe terrain (Croft et al., 1995), which is characterized by closed
 1697 topographic cells 20-50 km across and up to 500 m deep (Schenk et al., 2021). The dark material
 1698 appears to occur mainly on the elevated boundaries between the cells, suggesting that these
 1699 elevated terrains prevent volatile ice condensation or accelerate sublimation. These color and
 1700 topography contrasts between the northern and southern deposits at the cap edge could indicate
 1701 a gradual decrease in elevation to the south.

1702 **8.6. Model predictions for the next decades**

1703 **8.6.1. General climate predictions**

1704

1705 **Surface pressure and stellar occultations**

1706 Our best-case simulations that best match the observed surface pressure of the 2017 event
 1707 suggest a slow decrease in surface pressure over the next decades, at least until 2080 when the
 1708 subsolar point will be above 30°N and when northern sublimation should dominate over southern
 1709 condensation (Figure 21). These simulations suggest a surface pressure of ~1-1.5 Pa in the
 1710 period 2020-2040 and ~0.5-1 Pa by 2060. This is large enough for Triton's atmosphere to remain
 1711 global during this period. In the next decades, stellar occultation events will be key to confirming

1712 or disproving the trend suggested by our model. The next Triton occultation will be on Oct. 6,
1713 2022, and should indicate a surface pressure close to the 2017 value.

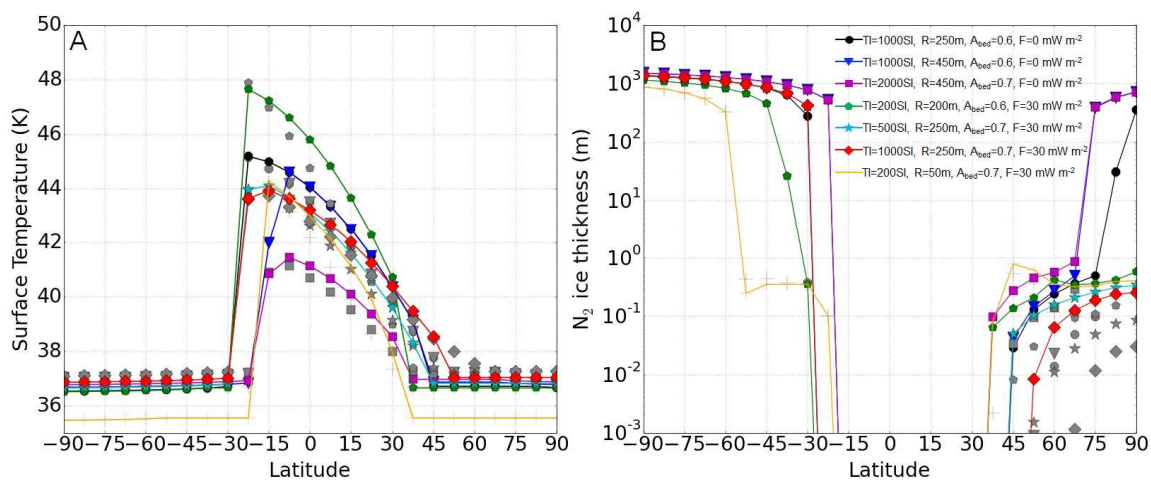
1714

1715 The southern and northern volatile ice deposits

1716 Our results suggest that most of the N_2 deposits in the southern hemisphere are permanent, and
1717 the southern cap extent should therefore not change much over seasonal timescales (Figure 22,
1718 Figure 27.B). Our simulations performed with a low global N_2 reservoir (< 200 m) tend to predict
1719 a retreat of the southern cap, but they fail to meet the observational constraints on the northern
1720 cap extent in 1989 and on the surface pressure in 2017. In particular, the southern cap should
1721 not have retreated by more than 30° latitude since 1989 from its $\sim 15^\circ S$ extent at that time,
1722 otherwise the surface pressure would have dramatically collapsed since 1989, and would be
1723 inconsistent with the 2017 occultation (see Figure best_pres.B, Figure profile.B).

1724 We obtained a large diversity of results regarding the thickness and the nature (perennial,
1725 seasonal, or non-existent) of the northern deposits. Our best-case simulations suggest that the
1726 N_2 northern cap will extend to at least $60^\circ N$ in 2040 (and possibly down to $30^\circ N$, Figure 22, Figure
1727 27). The extent of the seasonal northern N_2 deposits should be maximal during the period 2010-
1728 2030 (Figure 22). As the subsolar latitude currently increases with time, northern latitudes that
1729 were hidden in the polar night during the Voyager 2 flyby in 1989 start to be revealed. In the
1730 following decades, the northern cap at $60^\circ N$ (at least its seasonal deposits), if existing, should
1731 therefore become visible below the northern limb in ~ 2025 (subsolar latitude $\sim 30^\circ S$). Future
1732 observations of Triton with HST, JWST, and the Extremely Large Telescope (ELT) would be able
1733 to provide a new and rich dataset of Triton's surface (e.g., surface composition, rotational light-
1734 curves, and albedo maps at different wavelengths), which should give strong constraints on the
1735 extent of the northern and southern caps as well as on the surface properties of the different
1736 terrains (see examples in Section 8.6.2).

1737 In our model, N_2 ice sublimation is more intense at the south pole than at the cap edge during the
1738 current season, and will continue until 2025-2030. The south pole may thus appear darker and to
1739 be enriched in CH_4 ice in the coming years. In 2030, the south pole should start to be dominated
1740 by N_2 condensation (Figure 22), which should reverse this trend. Finally, equatorial N_2
1741 condensation is predicted until ~ 2025 , possibly forming bright N_2 -rich frosts. After 2025, N_2
1742 sublimation should dominate in the equatorial regions, and any equatorial seasonal N_2 frost
1743 should start to disappear.



1744

1745 Figure 27: A. Surface temperature vs latitude for the best-case simulations in 1989 (grey symbols,
1746 as in Figure 23) and in 2030 (solid line with colored symbols). Without internal heat flux : TI=1000
1747 SI - R=250 m - $A_{\text{bed}}=0.6$ (black circle), TI=1000 SI - R=450 m - $A_{\text{bed}}=0.6$ (blue triangle), TI=2000
1748 SI - R=450 m - $A_{\text{bed}}=0.7$ (purple square). With internal heat flux: TI=200 SI - R=200 m - $A_{\text{bed}}=0.6$
1749 (green polygon), TI=500 SI - R=250 m - $A_{\text{bed}}=0.7$ (cyan star), TI=1000 SI - R=250 m - $A_{\text{bed}}=0.7$
1750 (red losange). The orange solid line shows the cases of a low reservoir and low thermal inertia
1751 simulation (TI=200 SI - R=50 m - $A_{\text{bed}}=0.7$ - $F=30 \text{ W m}^{-2}$) that is consistent with observed caps
1752 extent and volatile fractional area but inconsistent with the observed pressure in 2017 (too low,
1753 see text in Section 8.3). Right. Same as A but showing the surface N_2 ice thickness.

1754 **Atmospheric abundances of CO and CH₄**

1755 According to our model and assuming a constant and uniform CO ice mixing ratio into N_2 ice of
1756 0.04%-0.08%, the CO gas volume mixing ratio should remain relatively constant with time, with
1757 values around 0.005%-0.01% in 2040 (see Section 7.4.1). The evolution of the CH_4 atmospheric
1758 mixing ratio in the next decades remains uncertain (and very sensitive to the surface area covered
1759 by CH_4 -rich deposits, see Section 7.4.2). It would tend to increase as the surface pressure
1760 decreases, in particular if new CH_4 -rich deposits form in the mid-to-low latitudes at the edge of
1761 the southern cap. However, if most of the CH_4 -rich deposits formed at the south pole, the CH_4
1762 atmospheric mixing ratio would decrease in the next decades (see Figure 24) as the south pole
1763 will approach polar winter. CH_4 gas is relatively easy to observe from the ground (Lellouch et al.
1764 2010) and could be further monitored with e.g. CRRES+ at the VLT, and subsequently with
1765 HIRES on ELT.

1766 8.6.2. Thermal lightcurve predictions for JWST

1767 In this section, we model thermal lightcurves of Triton for different climate scenarios in 2022.
1768 Thermal lightcurves of Triton have never been observed before due to the inability of previous
1769 facilities (e.g., Spitzer, Herschel) to separate Triton from Neptune, given the maximum $\sim 15^\circ$
1770 angular distance. Although ALMA can easily resolve Triton from Neptune, thermal radiation at
1771 mm wavelength is actually more sensitive to emissivity effects than to thermal inertia. JWST
1772 would be able to measure Triton's thermal lightcurve for the first time with the Mid-Infrared Instrument
1773 (MIRI, imaging mode), at 21 and 25.5 μm . We show here that future observations of Triton with
1774 JWST/MIRI would provide us with a one-of-a-kind dataset of Triton's surface that would strongly
1775 constrain the ice distribution and the surface properties (temperature, emissivity, roughness...) of
1776 the volatile-covered vs. bedrock terrains. In addition, these observations would be able to test our
1777 model predictions and to discriminate between the climate scenarios presented in this section.

1778 We designed and ran three simulations of the current seasonal cycle of Triton based on some of
1779 our best-case simulations (TI=1000 SI, no internal heat flux, R=200 and 650m, A=0.6 and 0.7).
1780 In these three simulations, we artificially prescribed the longitudinal asymmetry of the southern
1781 cap seen in the Voyager 2 images and inferred from the IRTF/SpeX spectra, with the bright
1782 deposits roughly extending to the equator on the sub-Neptunian hemisphere and to $\sim 30^\circ\text{S}$ in the
1783 opposite hemisphere (peak-to-peak magnitude of $\pm 15^\circ$ in latitude), and we assumed that the
1784 longitudinal variation of the spectrum has not changed since 1989. The three simulations are
1785 realistic in the sense that they are consistent with (1) a projected surface area of the volatile ice
1786 (given by NIR spectra) of $\sim 60\text{-}70\%$ in the period 1995-2010 (2) a southern cap extending to 15°S
1787 $\pm 15^\circ$ and no northern deposits south of 45°N in 1989 (consistent with Voyager 2 images), (3) a
1788 disk-averaged brightness temperature of 38-41 K at 45 μm in 1989 (consistent with the values
1789 retrieved from Voyager 2/IRIS), (4) relatively high Bond albedos for all terrains (0.6-0.8), and (5)
1790 a surface pressure of $\sim 1.4 \pm 0.2 \text{ Pa}$ in 1989 and $\sim 1.41 \pm 0.4 \text{ Pa}$ in 2017 (see Figure 29.A).

1791 However, the three simulations differ in terms of bedrock surface albedo ($A=0.6$ vs. $A=0.7$) and
 1792 of the extent of the southern cap in 2022 (large permanent cap to 7.5°S vs small cap to 37.5°S)
 1793 as shown by Figure 28, which leads to three different climate scenarios (relatively cold, relatively
 1794 warm, and intermediate):

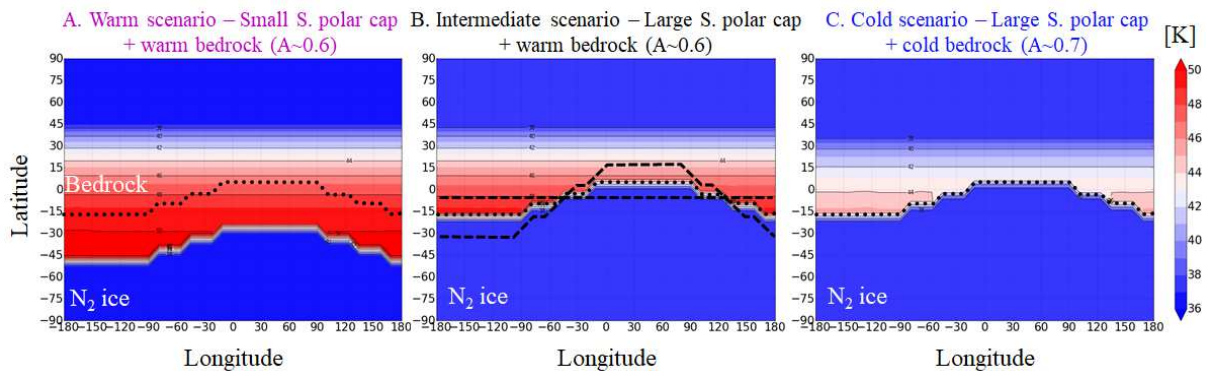
1795 **(A) Warm scenario:** Based on the simulation with $TI=1000$ SI, $A=0.6$, $R=200\text{m}$. In this scenario,
 1796 we artificially set the thickness of N_2 ice to a few centimeters in the mid-to-equatorial southern
 1797 regions so that these deposits become seasonal, undergo sublimation since 1989, and lead to a
 1798 retreat of the southern cap from the equator in 1989 to 37.5°S in 2022. We also assume a warm
 1799 bedrock surface ($A=0.6$) north of these deposits, which leads to a relatively warm global mean
 1800 surface temperature.

1801 **(B) Intermediate scenario:** Based on the simulation with $TI=1000$ SI, $A=0.6$, $R=650\text{m}$. This
 1802 scenario assumes a large permanent N_2 southern cap (extending to 7.5°S) and a warm bedrock
 1803 surface ($A=0.6$).

1804 **(C) Cold scenario:** Based on the simulation with $TI=1000$ SI, $A=0.7$, $R=650\text{m}$. This scenario
 1805 assumes a large permanent N_2 southern cap (extending to 7.5°S), a cold bedrock surface ($A=0.7$),
 1806 and more extended N_2 ice in the northern hemisphere, which leads to a relatively cold global mean
 1807 surface temperature.

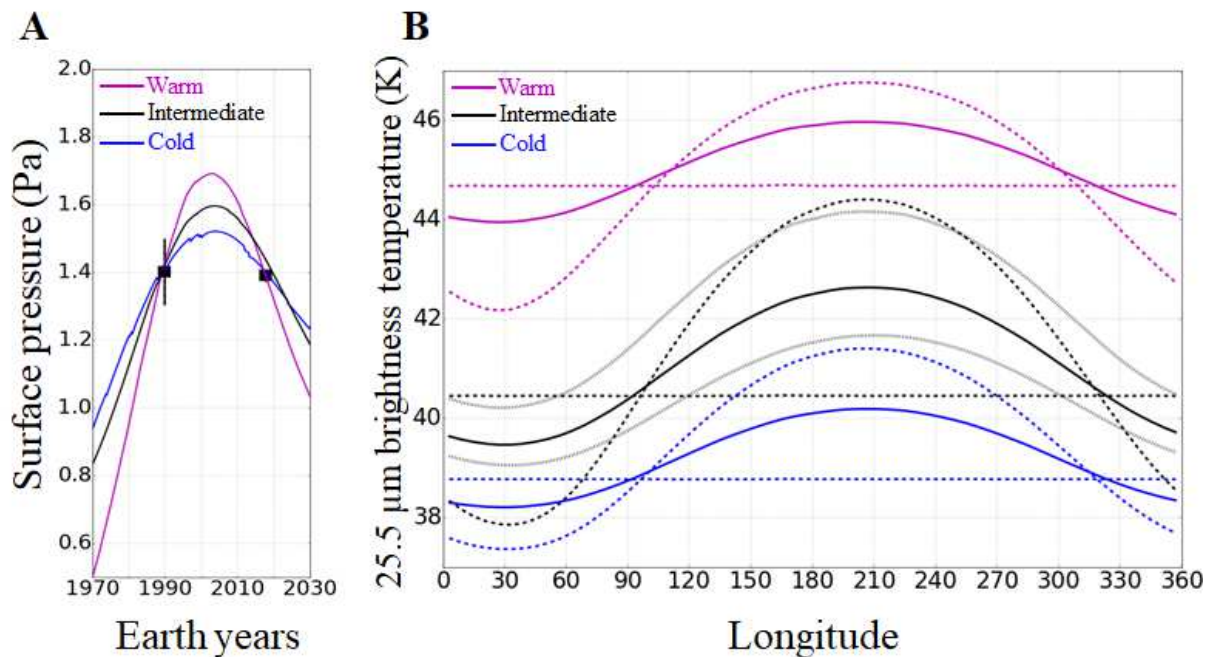
1808 We also performed similar simulations with no longitudinal asymmetry for the southern cap or with
 1809 a longitudinal asymmetry amplified to a magnitude of $\pm 25^\circ$ latitude. The boundary of the cap edge
 1810 in these cases is illustrated by the dashed lines on Figure 28.B.

1811



1812
 1813 Figure 28: Modeled surface temperatures on Triton in 2022 (at local noon) for three climate
 1814 scenarios with different extents for the southern cap and bedrock surface albedo. A. Warm
 1815 scenario: reduced cap extent and warm bedrock ($A=0.6$). B. Intermediate scenario: large cap
 1816 extent and warm bedrock ($A=0.6$). C. Cold scenario: large cap extent, cold bedrock ($A=0.7$), and
 1817 more extended N_2 ice in the northern hemisphere. Dotted lines indicate the modeled cap extent
 1818 in 1989 (the cap retreated only in scenario A). Dashed lines in panel B illustrate the cap extent in
 1819 alternative simulations in which the longitudinal asymmetry disappeared or amplified to a
 1820 magnitude of $\pm 25^\circ$ latitude ($\pm 15^\circ$ is the reference case and roughly corresponds to the asymmetry
 1821 seen by Voyager 2 in 1989).

1822



1823
1824
1825
1826
1827
1828
1829
1830

Figure 29: Triton climate model results. A. Surface pressure evolution for the 3 scenarios presented on Figure 28. Black squares indicate the Voyager 2 and 2017 occultation observations (Gurrola, 1995, Marques Oliveira et al., 2021). B. Triton 25.5 μm lightcurve for the 3 climate scenarios (with a 15° longitudinal asymmetry), with a diurnal thermal inertia of 20 SI (solid line). Dashed lines show the light curve for the alternative simulations with no or with ±25° longitudinal asymmetry. Grey lines for the intermediate scenario are for TI=10 (warmer) and TI=40 SI (colder).

1831 Figure 28 shows that the N₂ southern cap surface temperature in 2022 is ~37 K (at solid-gas
1832 equilibrium) for the 3 cases while the equatorial volatile-free bedrock surface temperature (at local
1833 noon) is ~46 K for the warm and intermediate scenarios (A=0.6) and ~44 K for the cold scenario
1834 (A=0.7). In the case of a significant cap retreat since 1989, the volatile-free surface temperature
1835 in the mid-southern latitudes may reach ~50 K in 2022 (Figure 28.A). We note that locally, even
1836 warmer (resp. colder) patches could exist on Triton's surface due to subsurface heating activity
1837 (hot spots) or if the bedrock surface Bond albedo is significantly lower than 0.6 (resp. higher than
1838 0.7). JWST/MIRI will be able to measure the thermal lightcurve of Triton (as seen from the Earth,
1839 i.e. of the projected disk) at 25.5 μm (and also at 21 μm) with its F2550W filter. Figure 29.B shows
1840 the modeled thermal lightcurves at 25.5 μm for the 3 climate scenarios in 2022. The thermal
1841 rotational variation on Triton is anti-correlated to the (subdued) optical light curve, with the
1842 warmest brightness temperatures being associated with the darkest regions (note that N₂-rich
1843 regions have a uniform temperature, ~37K, controlled by the surface pressure and the global
1844 albedo but not the local albedo). The thermal lightcurve variation and overall flux level therefore
1845 sensitively depend on ice distribution, mainly the presence/absence of volatile ice at the south
1846 pole, the southern cap extent, and the longitudinal variability between 45°S-20°N. Although N₂ ice
1847 deposits could cover the latitudes 90°N-30°N in 2022 and thus be seen by Earth-based telescopes
1848 in a small crescent below the terminator (56°N), they will have a weak quasi-negligible contribution
1849 to the lightcurves due to their cold surface and their small contribution (~ 3% in 2022, see
1850 Appendix A in Holler et al., 2016) to the total projected area relative to Triton's visible disk.

1851 The thermal lightcurve is also sensitive to the thermal and energetic properties of the N₂-free
1852 terrains (thermal inertia, surface roughness, bolometric and spectral emissivity, Lellouch et al.,
1853 2011, 2016). In particular, the measured mean brightness temperature can discriminate between
1854 warm or cold scenarios (Figure 29.B). We expect generally low diurnal thermal inertias (TI=10-30
1855 SI) as on Pluto (Lellouch et al., 2016), but this can be confirmed or disproved by thermal lightcurve
1856 measurements as the amplitude, general flux level and shape of the light curve will decrease for
1857 higher thermal inertia (see grey lines on Figure 29.B).

1858 8.7. Uncertainties and future work

1859

1860 Although we explored the volatile cycles on Triton by using a large range of model parameters,
1861 other combinations may exist that also reproduce the observations. In particular, in the volatile
1862 transport simulations of this paper (Section 7), we fixed the diurnal and seasonal thermal inertia
1863 of N₂ ice to 20 SI and 800 SI respectively, and we only explored a north-south asymmetry in N₂
1864 ice albedo ($\Delta A_{N_2}=0.1$). Other values for the thermal inertia are possible, although they should not
1865 impact the results to first order if they remain in the range of what has been suggested for Pluto
1866 (10-40 SI and 500-2000 SI, respectively). Other north-south or local asymmetries in albedo,
1867 emissivity, ice composition or internal heat flux are possible and may significantly impact the
1868 results. In particular, albedos and ice composition feedback probably have a significant role as
1869 geysers could deposit dark material (resp. bright ice grain) on top of the ice, and further darken
1870 (resp. brighten) the ice. Haze particle deposition and volatile ice sublimation could also contribute
1871 to darken the ice locally. We also consider that Triton's atmosphere remains always global, even
1872 when it hits a non-global limit in the past, with N₂ ice temperatures varying over the body. These
1873 processes are not taken into account in our model.

1874 In addition, in our model, when both CH₄ and N₂ ices are present on the surface and CH₄ is
1875 sublimating, we assume that CH₄ is diluted in a solid solution N₂:CH₄ with a mole fraction of CH₄
1876 in N₂ ice of 0.05% (Quirico et al. 1999, Merlin et al., 2018). We apply Raoult's law to compute the
1877 CH₄ atmospheric mixing ratio at saturation, as in Forget et al. (2017). We do not take into account
1878 possible variations and deviations from equilibrium. Tan and Kargel (2018) showed that these
1879 volatile ices should not exhibit such ideal behavior and form solid solutions whose phases follow
1880 ternary phase equilibria (N₂, CO, CH₄). We note that sophisticated equations of state exist for the
1881 N₂-CO-CH₄ systems under Triton surface conditions (CRYOCHEM, Tan and Kargel, 2018). As
1882 these equations of state have not been coded for use in a climate model or been applied to the
1883 specific distribution of ices and temperatures seen on Triton, we have substituted the alternative
1884 of relying on Raoult's law.

1885 Future work involving laboratory experiments, spectroscopic analyses, thermodynamic models,
1886 and global circulation models (GCMs) is strongly needed to improve the models, constrain the
1887 timescales for ice relaxation toward thermodynamic equilibrium, and explore in detail the effect of
1888 the ternary phase equilibrium on Triton and Pluto (and on other Trans-Neptunian objects). Lastly,
1889 coupling the volatile transport model with models of internal structure (including cryovolcanic
1890 activity, obliquity tides) and outgassing could also help us better understand the formation of
1891 geysers on Triton and atmospheric escape.

1892 Conclusions

1893

1894 We simulated the long-term and seasonal volatile cycles of Triton, exploring a large range of model
1895 parameters (thermal inertia, bedrock surface albedo, global reservoir of N₂ ice, internal heat flux)

1896 and comparing with available observations (Voyager 2 images and surface pressure, infrared
1897 surface emission measurements, albedo maps, volatile fractional area from Earth-based near-
1898 infrared spectra and surface pressure evolution from stellar occultations) to better constrain these
1899 parameters. In particular, we use an extremely high-quality occultation dataset obtained in 2017
1900 to define our best-case simulations (Marques Oliveira et al., 2021). The following results were
1901 obtained:

- 1902 1. Permanent volatile ice caps form at the poles and extend to low latitudes through
1903 glacial flow or through the formation of thinner seasonal deposits. North-South
1904 asymmetries in surface properties can favor the development of one cap over the
1905 other, as previously evidenced. A difference in topography has little impact on the
1906 North-South N₂ ice asymmetry.
- 1907 2. Best-case simulations are obtained for a bedrock surface albedo of 0.6-0.7, a global
1908 reservoir of N₂ ice thicker than 200 m, and a bedrock thermal inertia larger than 500
1909 SI or smaller but with a large internal heat flux (>30 mW m⁻²). The large N₂ ice reservoir
1910 implies a permanent N₂ southern cap (several 100 m thick, and up to 1.5 km thick)
1911 extending to the equatorial regions with higher amounts of volatile ice at the south
1912 pole, which is not inconsistent with Voyager 2 images but does not reconcile well with
1913 observed full-disk near-infrared spectra. In particular, the lack of variability of the non-
1914 volatile ices (H₂O, CO₂, and ethane) with longitude (Holler et al., 2016) is not explained
1915 by our model.
- 1916 3. Our results suggest that a small permanent polar cap should exist in the northern
1917 hemisphere, in particular if the internal heat flux remains relatively low (e.g. radiogenic,
1918 < 3 mW m⁻²) and if the bedrock albedo is >0.7. A non-permanent northern polar cap
1919 was only obtained for simulations with high internal heat flux (30 mW m⁻²). The
1920 northern cap will possibly extend to 30°N in the next decade, thus becoming visible by
1921 Earth-based telescopes. The southern cap should not significantly retreat in the next
1922 decades compared to what has been observed in 1989.
- 1923 4. Our model predicts N₂ condensation at the northern edge of the southern cap in the
1924 period 1980-2020, which could explain the bright equatorial fringe observed by
1925 Voyager 2 in 1989. The model predicts that over the last 30 years, the southern polar
1926 cap lost ~0.3 m of N₂ ice by sublimation, while ~0.1 m of ice deposited in the equatorial
1927 regions and mid northern latitudes.
- 1928 5. Best-case surface pressures are consistent with a moderate increase of pressure
1929 during the 1990-2000 period. The model suggests that the peak of surface pressure
1930 occurred between 2000-2010 and did not exceed ~2 Pa (although albedo feedback
1931 may have increase the peak amplitude).
- 1932 6. According to our model, the atmosphere of Triton never collapses. The surface
1933 pressure should slowly decrease but remain larger than 0.5 Pa by 2060. Simulations
1934 performed with low ice emissivity ($\epsilon_{N_2}=0.3-0.5$) show that the surface pressure could
1935 always remain larger than 0.5 Pa. Seasonal thin deposits play a significant role in the
1936 evolution of the surface pressure. The internal heat flux does not significantly impact
1937 the surface pressure curve since the ice albedo is adjusted to match the Voyager 2
1938 pressure constraint (it impacts locally the sublimation-condensation rates but not the
1939 net mass balance of N₂).
- 1940 7. In our model, CO tends to follow N₂ and condenses where N₂-rich deposits are already
1941 present. By using a CO/N₂ ice mixing ratio of 0.04%-0.08%, we obtain an atmospheric

1942 CO gas volume mixing ratio of 0.006%-0.012% during the period 2000-2020, and
1943 slightly slower values for the next decades (0.005%-0.01%).

1944 8. Unlike for Pluto, no permanent CH₄-rich deposit form in our Triton model. We tested
1945 two scenarios with small CH₄-rich ice patches to explain the observed CH₄
1946 atmospheric mixing ratio. Simulations with CH₄-rich ice at the cap edge (equatorial
1947 regions) produce a CH₄ partial pressure of $1-5 \times 10^{-4}$ Pa that remains relatively constant
1948 during the period 1980-2030. Simulations with CH₄-rich ice at the south pole produce
1949 a strong increase in CH₄ partial pressure until 2005, followed by a decrease as the
1950 south pole exits polar day. Both "cap edge" and "south pole" scenarios could reconcile
1951 the 2.45×10^{-4} Pa partial pressure observed by Voyager 2 and the increase in the CH₄
1952 partial pressure (factor of 4) observed from 1989 to 2009 (Lellouch et al., 2010),
1953 although the "cap edge" scenario would require a decrease in CH₄ ice albedo or
1954 increase in CH₄ ice coverage with time to lead to a significant increase in CH₄ partial
1955 pressure.

1956 9. JWST/MIRI will be able to measure the thermal lightcurve of Triton at 25.5, 21 μ m,
1957 which will help in discriminating several possible climate scenarios, as well as in
1958 providing strong constraints on the thermal and energetic properties of the N₂-free
1959 terrains.

1960 Triton remains relatively unexplored. In particular, we note that there is a strong need for more
1961 and continuing Earth-based observations (JWST, HST, VLT, Keck, ELT) of Triton's surface and
1962 atmosphere in order to provide a temporal context and understand Triton's seasonal evolution.
1963 Surface ice distribution has never been mapped, only inferred from disk integrated rotational
1964 curves of ice band depths, and except for very limited observations, surface temperatures have
1965 not been measured. This manifests as a substantial gap in our understanding of Triton's climate
1966 evolution. Finally, an orbiter mission such as Neptune Odyssey or a flyby mission to Triton such
1967 as Trident would provide a rich science-breakthrough dataset with which to understand the
1968 physical and dynamical processes at play on Triton and their seasonal evolution (by comparison
1969 with existing Earth-based observations), which would be insightful to further understand this class
1970 of volatile-rich object, including Pluto, Eris, and Makemake.

1971

1972 Acknowledgments

1973

1974 T. B. was supported for this research by an appointment to the National Aeronautics and Space
1975 Administration (NASA) Postdoctoral Program at the Ames Research Center administered by
1976 Universities Space Research Association (USRA) through a contract with NASA. Part of the work
1977 leading to these results has received funding from the European Research Council under the
1978 European Community's H2020 2014-2021 ERC Grant Agreement n°669416 "Lucky Star". Under
1979 contract with NASA, part of this work was conducted at the Jet Propulsion Laboratory, California
1980 Institute of Technology.

1981 References

1982 Agnor, C.B., Hamilton, D.P., 2006. Neptune's capture of its moon Triton in a binary-planet
1983 gravitational encounter. *Nature* 441, 192-194.

1984

- 1985 Augé, B. and 12 colleagues, 2016. Irradiation of nitrogen-rich ices by swift heavy ions. Clues for
 1986 the formation of ultracarbonaceous micrometeorites. *Astronomy and Astrophysics* 592.
 1987 doi:10.1051/0004-6361/201527650.
- 1988
- 1989 Bauer, J.M., Buratti, B.J., Li, J.-Y., Mosher, J.A., Hicks, M.D., Schmidt, B.E., Goguen, J.D., 2010.
 1990 Direct detection of seasonal changes on Triton with Hubble Space Telescope. *ApJL* 723, L49-
 1991 L52.
- 1992
- 1993 Bertrand, T., & Forget, F., 2016. Observed glacier and volatile distribution on Pluto from
 1994 atmosphere-topography processes. *Nature*, 540(7631). <https://doi.org/10.1038/nature19337>.
- 1995
- 1996 Bertrand, T., Forget, F., Umurhan, O. M., Grundy, W. M., Schmitt, B., Protopapa, S., Zangari, A.
 1997 M., White, O. L., Schenk, P. M., Singer, K. N., Stern, A., Weaver, H. A., Young, L. A., Ennico, K.,
 1998 & Olkin, C. B., 2018. The nitrogen cycles on Pluto over seasonal and astronomical timescales.
 1999 *Icarus*, 309, 277–296. <https://doi.org/10.1016/j.icarus.2018.03.012>.
- 2000
- 2001 Bertrand, T., Forget, F., Umurhan, O. M., Moore, J. M., Young, L. A., Protopapa, S., Grundy, W.
 2002 M., Schmitt, B., Dhingra, R. D., Binzel, R. P., Earle, A. M., Cruikshank, D. P., Stern, S. A., Weaver,
 2003 H. A., Ennico, K., & Olkin, C. B., 2019. The CH₄ cycles on Pluto over seasonal and astronomical
 2004 timescales. *Icarus*. <https://doi.org/10.1016/j.icarus.2019.02.007>.
- 2005
- 2006
- 2007 Bertrand, T., Forget, F., White, O., Schmitt, B., Stern, S. A., Weaver, H. A., Young, L. A., Ennico,
 2008 K., & Olkin, C. B., 2020a. Pluto's Beating Heart Regulates the Atmospheric Circulation: Results
 2009 From High-Resolution and Multiyear Numerical Climate Simulations. *Journal of Geophysical*
 2010 *Research: Planets*, 125(2), 1–24. <https://doi.org/10.1029/2019JE006120>.
- 2011
- 2012 Bertrand, T., Forget, F., Schmitt, B., White, O. L., & Grundy, W. M., 2020b. Equatorial mountains
 2013 on Pluto are covered by methane frosts resulting from a unique atmospheric process. *Nature*
 2014 *Communications*, 11, 5056.
- 2015
- 2016 Broadfoot, A. L., et al., 1989. Ultraviolet spectrometer observations of Neptune and Triton.
 2017 *Science* 246, 1459-1466.
- 2018
- 2019 Brown, R. H., Johnson, T. V., Goguen, J.D., Schubert, G., Ross, M. N., 1991. Triton's Global Heat
 2020 Budget. *Science* 251, 1465–1467. doi:10.1126/science.251.5000.1465.
- 2021
- 2022 Brown, R. H., Kirk, R. L., 1994. Coupling of volatile transport and internal heat flow on Triton.
 2023 *Journal of Geophysical Research* 99, 1965–1982. doi:10.1029/93JE02618.
- 2024

2025 Brown, R. H., Cruikshank, D. P., Veverka, J., Helfenstein, P., Eluszkiewicz, J., 1995. Surface
2026 composition and photometric properties of Triton. *Neptune and Triton*, 991–1030.
2027

2028 Buratti, B. J., Goguen, J. D., Gibson, J., Mosher, J., 1994. Historical photometric evidence for
2029 volatile migration on Triton. *Icarus* 110, 303-314.
2030

2031 Buratti, B. J., Bauer, J. M., Hicks, M. D., Hillier, J. K., Verbiscer, A., Hammel, H., Schmidt, B.,
2032 Cobb, B., Herbert, B., Garsky, M., Ward, J., & Foust, J., 2011. Photometry of Triton 1992-2004:
2033 Surface volatile transport and discovery of a remarkable opposition surge. *Icarus*, 212(2), 835–
2034 846. <https://doi.org/10.1016/j.icarus.2011.01.012>.
2035

2036 Chen, E. M. A., Nimmo, F., Glatzmaier, G. A., 2014. Tidal heating in icy satellite oceans. *Icarus*
2037 229, 11–30. doi:10.1016/j.icarus.2013.10.024.
2038

2039 Conrath, B. and 15 colleagues, 1989. Infrared Observations of the Neptunian System. *Science*
2040 246, 1454–1459. doi:10.1126/science.246.4936.1454.
2041

2042 Correia, A. C. M., 2009. Secular evolution of a satellite by tidal effect: Application to triton.
2043 *Astrophysical Journal*. <https://doi.org/10.1088/0004-637X/704/1/L1>.
2044

2045 Croft, S. K., Kargel, J. S., Kirk, R. L., Moore, J. M., Schenk, P. M., Strom, R. G., 1995. The geology
2046 of Triton. In: Cruikshank (Ed.), *Neptune and Triton*. University of Arizona Press, Tucson, pp. 879–
2047 947.
2048

2049 Cruikshank, D. P. and 7 colleagues, 1991. Tentative Detection of CO and CO₂ Ices on Triton.
2050 *Bulletin of the American Astronomical Society*.
2051

2052 Cruikshank, D. P., Roush, T. L., Owen, T. C., Geballe, T. R., de Bergh, C., Schmitt, B., Brown, R.
2053 H., Bartholomew, M. J., 1993. Ices on the surface of Triton. *Science* 261, 742-745.
2054

2055 Cruikshank, D. P., Schmitt, B., Roush, T. L., Owen, T. C., Quirico, E., Geballe, T. R., de Bergh,
2056 C., Bartholomew, M. J., Dalle Ore, C. M., Douté, S., Meier, R., 2000. Water ice on Triton. *Icarus*
2057 147, 309-316.
2058

2059 DeMeo, F. E., Dumas, C., de Bergh, C., Protopapa, S., Cruikshank, D. P., Geballe, T.R., Alvarez-
2060 Candal, A., Merlin, F., Barucci, M. A., 2010. A search for ethane on Pluto and Triton. *Icarus* 208,
2061 412-424.
2062

2063 Doute, S., B. Schmitt, E. Quirico, T. C. Owen, D. P. Cruikshank, C. de Bergh, T. R. Geballe, and
2064 T.L. Roush, 1999. Evidence for methane segregation at the surface of Pluto. *Icarus*, 142, 421-
2065 444.

2066 Dubois, D. , Patthoff, D.A, Pappalardo, R.T., 2017. Diurnal, Nonsynchronous Rotation and
2067 Obliquity Tidal Effects on Triton Using a Viscoelastic Model: SatStressGUI. Implications for Ridge
2068 and Cycloid Formation. LPSC, LPI #1964, 2897.

2069 Duxbury, N. S., Brown, R. H., 1993. The Phase Composition of Triton's Polar Caps. *Science* 261,
2070 748–751. doi:10.1126/science.261.5122.748.

2071

2072 Earle, A. M., Binzel, R. P., Young, L. A., Stern, S. A., Ennico, K., Grundy, W., Olkin, C. B., Weaver,
2073 H. A. New Horizons Surface Composition Theme, 2018. Albedo matters: understanding runaway
2074 albedo variations on Pluto. *Icarus* 303, 1–9. doi: 10.1016/j.icarus.2017.12.015.

2075

2076 Elliot, J. L., et al., 1998. Global warming on Triton. *Nature* 393, 765-767.

2077

2078 Elliot, J. L., Strobel, D. F., Zhu, X., Stansberry, J. A., Wasserman, L. H., & Franz, O. G., 2000.
2079 The thermal structure of triton's middle atmosphere. *Icarus*, 143(2), 425–428.
2080 <https://doi.org/10.1006/icar.1999.6312>.

2081

2082 Elliot, J. L., Person, M. J., Qu, S., 2003. Analysis of Stellar Occultation Data. II. Inversion, with
2083 Application to Pluto and Triton. *The Astronomical Journal* 126, 1041–1079. doi:10.1086/375546

2084

2085 Eluszkiewicz, J., 1991. On the microphysical state of the surface of Triton. *J. Geophys. Res.* 96,
2086 19217-19229.

2087 Ferrari, C. & Lucas, A., 2016. Low thermal inertias of icy planetary surfaces. Evidence for
2088 amorphous ice? *Astronomy and Astrophysics*, 588, A133.

2089

2090 Forget, F., Bertrand, T., Vangvichith, M., Leconte, J., Millour, E., & Lellouch, E., 2017. A post-
2091 New Horizons global climate model of Pluto including the N₂, CH₄ and CO cycles. *Icarus*, 287,
2092 54–71. <https://doi.org/10.1016/j.icarus.2016.11.038>.

2093

2094 Fray, N., Schmitt, B., 2009. Sublimation of ices of astrophysical interest: A bibliographic review.
2095 *P&SS* 57, 2053-2080.

2096

2097 Gaeman, J., Hier-Majumder, S., Roberts, J. H., 2012. Sustainability of a subsurface ocean within
2098 Triton's interior. *Icarus* 220, 339–347. doi:10.1016/j.icarus.2012.05.006.

2099

2100 Grundy, W. M., Fink, U., 1991. A new spectrum of Triton near the time of the Voyager encounter.
2101 *Icarus* 93, 379–385. doi:10.1016/0019-1035(91)90220-N.

2102

2103 Grundy, W. M., & Young, L. A., 2004. Near-infrared spectral monitoring of Triton with IRTF/SpeX
2104 I: Establishing a baseline for rotational variability. *Icarus*, 172(2), 455–465.
2105 <https://doi.org/10.1016/j.icarus.2004.07.013>

2106

2107 Grundy, W. M., Young, L. A., Stansberry, J. A., Buie, M. W., Olkin, C. B., Young, E. F., 2010.
2108 Near-infrared spectral monitoring of Triton with IRTF/SpeX II: Spatial distribution and evolution of
2109 ices. *Icarus* 205, 594-604.

2110

2111 Grundy, W. M., Binzel, R. P., Buratti, B. J., Cook, J. C., Cruikshank, D. P., Dalle Ore, C. M., Earle,
2112 A. M., Ennico, K., Howett, C. J. A., Lunsford, A. W., Olkin, C. B., Parker, A. H., Philippe, S.,
2113 Protopapa, S., Quirico, E., Reuter, D. C., Schmitt, B., Singer, K. N., Verbiscer, A. J., ... Young, L.
2114 A., 2016. Surface compositions across Pluto and Charon. *Science*, 351(6279).
2115 <https://doi.org/10.1126/science.aad9189>.

2116

2117 Gurrola, E. M., 1995. Interpretation of Radar Data from the Icy Galilean Satellites and Triton.
2118 Ph.D. thesis, Stanford University.

2119

2120 Gurwell, M., Lellouch, E., Butler, B., Moreno, R., Moullet, A., Strobel, D., 2019. The Atmosphere
2121 of Triton Observed With ALMA. EPSC-DPS Joint Meeting 2019.

2122

2123 Hansen, C.J., Paige, D.A., 1992. A thermal model for the seasonal nitrogen cycle on Triton. *Icarus*
2124 99, 273-288.

2125

2126

2127 Herbert, F., Sandel, B.R., 1991. CH₄ and haze in Triton's lower atmosphere. *JGR Supp.* 96,
2128 19241-19252.

2129

2130 Hillier, J., Helfenstein, P., Verbiscer, A., & Veverka, J., 1991. Voyager photometry of Triton: Haze
2131 and surface photometric properties. *Journal of Geophysical Research*, 96(S01), 19203.
2132 <https://doi.org/10.1029/91ja01736>.

2133

2134 Hillier, J., Veverka, J., Helfenstein, P., Lee, P., 1994. Photometric Diversity of Terrains on Triton.
2135 *Icarus* 109, 296–312. doi:10.1006/icar.1994.1095.

2136

2137 Holler, B. J., Young, L. A., Grundy, W. M., & Olkin, C. B., 2016. On the surface composition of
2138 Triton's southern latitudes. *Icarus*, 267, 255–266. <https://doi.org/10.1016/j.icarus.2015.12.027>.

2139

2140 Howard, A. D., Moore, J. M., White, O. L., Umurhan, O. M., Schenk, P. M., Grundy, W. M., Schmitt,
2141 B., Philippe, S., McKinnon, W. B., Spencer, J. R., Beyer, R. A., Stern, S. A., Ennico, K., Olkin, C.

2142 B., Weaver, H. A., & Young, L. A., 2017. Pluto: Pits and mantles on uplands north and east of
2143 Sputnik Planitia. *Icarus*, 293, 218–230. <https://doi.org/10.1016/j.icarus.2017.02.027>.

2144

2145 Hussmann, H., Sohl, F., Spohn, T., 2006. Subsurface oceans and deep interiors of medium-sized
2146 outer planet satellites and large trans-neptunian objects. *Icarus* 185, 258–273.
2147 doi:10.1016/j.icarus.2006.06.005.

2148

2149 Krasnopolsky, V. A., Cruikshank, D. P., 1999. Photochemistry of Pluto's atmosphere and
2150 ionosphere near perihelion. *J. Geophys. Res.* 104, 21979–21996. [http://dx.doi.org/](http://dx.doi.org/10.1029/1999JE001038)
2151 10.1029/1999JE001038.

2152

2153 Johnson, P. E. and 8 colleagues, 2021. Modeling Pluto's minimum pressure: Implications for haze
2154 production. *Icarus* 356. doi:10.1016/j.icarus.2020.114070.

2155

2156 Johnson, R.E., Oza, A. Young, L.A., Volkov, A. N., Schmidt, C. , 2015. Volatile Loss and
2157 Classification of Kuiper Belt Objects. *ApJ*, 809, 1, 43. doi:[10.1088/0004-637X/809/1/43](https://doi.org/10.1088/0004-637X/809/1/43)

2158

2159 Jovanovic, L., Gautier, T., Vuitton, V., Wolters, C., Bourgalais, J., Buch, A., Orthous-Daunay, F.,
2160 Vettier, L., Flandinet, L., Carrasco, N., 2020. Chemical composition of Pluto aerosol analogues.
2161 *Icarus*, 346, 113774, 10.1016/j.icarus.2020.113774.

2162

2163 Laskar J, Robutel P, 1993. The chaotic obliquity of the planets. *Nature* 361:608–612.

2164

2165 Lee, P., Helfenstein, P., Veverka, J., & McCarthy, D., 1992. Anomalous-scattering region on
2166 Triton. *Icarus*, 99(1), 82–97. [https://doi.org/10.1016/0019-1035\(92\)90173-5](https://doi.org/10.1016/0019-1035(92)90173-5).

2167

2168 Lellouch, E., de Bergh, C., Sicardy, B., Ferron, S., Käufel, H.-U., 2010. Detection of CO in Triton's
2169 atmosphere and the nature of surface-atmosphere interactions. *A&A* 512, L8-L13.

2170

2171 Lellouch, E., de Bergh, C., Sicardy, B., Käufel, H. U., Smette, A., 2011. High resolution
2172 spectroscopy of Pluto's atmosphere: detection of the 2.3 μm CH₄ bands and evidence for carbon
2173 monoxide. *Astron. Astrophys.* 530, L4. <http://dx.doi.org/10.1051/0004-6361/201116954>.

2174

2175 Lellouch, E. and 11 colleagues, 2016. The long-wavelength thermal emission of the Pluto-Charon
2176 system from Herschel observations. Evidence for emissivity effects. *Astronomy and Astrophysics*
2177 588. doi:10.1051/0004-6361/201527675.

2178

2179 Lellouch, E., Gurwell, M., Butler, B., Fouchet, T., Lavvas, P., Strobel, D. F., Sicardy, B., Moullet,
2180 A., Moreno, R., Bockelée-Morvan, D., Biver, N., Young, L., Lis, D., Stansberry, J., Stern, A.,

2181 Weaver, H., Young, E., Zhu, X., & Boissier, J., 2017. Detection of CO and HCN in Pluto's
2182 atmosphere with ALMA. *Icarus*, 286, 289–307. <https://doi.org/10.1016/j.icarus.2016.10.013>.
2183

2184 Lewis, B. L. and 12 colleagues, 2021. Distribution and energy balance of Pluto's nitrogen ice, as
2185 seen by New Horizons in 2015. *Icarus* 356. doi:10.1016/j.icarus.2020.113633.
2186

2187 Li, D., Johansen, A., Mustill, A. J., Davies, M. B., Christou, A. A., 2020. Capture of satellites during
2188 planetary encounters. A case study of the Neptunian moons Triton and Nereid. *Astronomy and*
2189 *Astrophysics* 638. doi:10.1051/0004-6361/201936672.
2190

2191 Lunine, J. E., and Stevenson, D. J., 1985. Physical state of volatiles on the surface of Triton.
2192 *Nature* 317, 238-240.
2193

2194 Mangold, N., 2011. Ice sublimation as a geomorphic process: A planetary perspective.
2195 *Geomorphology* 126, 1–17. doi:10.1016/j.geomorph.2010.11.009.
2196

2197 Marques Oliveira, J. et al. 2021. Structure and evolution of Triton's atmosphere from the 5 October
2198 2017 stellar occultation and previous observations. Submitted to *A&A*.
2199

2200 Martin-Herrero, A., Romeo, I., & Ruiz, J., 2018. Heat flow in Triton: Implications for heat sources
2201 powering recent geologic activity. *Planetary and Space Science*, 160, 19–25.
2202 <https://doi.org/10.1016/j.pss.2018.03.010>.
2203

2204 Materese, C. K., Cruikshank, D. P., Sandford, S. A., Imanaka, H., Nuevo, M. 2015. Ice Chemistry
2205 on Outer Solar System Bodies: Electron Radiolysis of N₂⁻, CH₄⁻, and CO-Containing Ices. *The*
2206 *Astrophysical Journal* 812. doi:10.1088/0004-637X/812/2/150.
2207

2208 McCord, T. B., 1966. Dynamical evolution of the Neptunian system. *Astron. J.* 71, 585.
2209 <http://dx.doi.org/10.1086/109967>.
2210

2211 McEwen, A. S., 1990. Global color and albedo variations on Triton. *Geophys Res Lett* 17, 1765–
2212 1768. <http://dx.doi.org/10.1029/GL017i010p01765>.
2213

2214 McKinnon, W. B., 1984. On the origin of Triton and Pluto. *Nature* 311, 355–358. [http://](http://dx.doi.org/10.1038/311355a0)
2215 dx.doi.org/10.1038/311355a0.
2216

2217 McKinnon, W. B., Lunine, J. I., Banfield, D., 1995. Origin and evolution of Triton. In: Cruikshank
2218 (Ed.), *Neptune and Triton*. University of Arizona Press, Tucson, pp. 807–877.
2219

- 2220 McKinnon W. B., Nimmo F., Wong T., et al., 2016. Convection in a volatile nitrogen-ice-rich layer
 2221 drives Pluto's geological vigour. *Nature*, 534, 82-85.
- 2222
- 2223 Merlin, F., 2015. New constraints on the surface of Pluto. *Astron. Astrophys.* 582, A39.
 2224 <http://dx.doi.org/10.1051/0004-6361/201526721>.
- 2225
- 2226 Merlin, F., E. Lellouch, E. Quirico, and B. Schmitt, 2018. Triton's surface ices: Distribution,
 2227 temperature and mixing state from VLT/SINFONI observations. *Icarus* 314, 274-293.
- 2228
- 2229 Meza, E., Sicardy, B., Assafin, M., Ortiz, J. L., Bertrand, T., Lellouch, E., Desmars, J., Forget, F.,
 2230 Bérard, D., Doressoundiram, A., Lecacheux, J., Oliveira, J. M., Roques, F., Widemann, T., Colas,
 2231 F., Vachier, F., Renner, S., Leiva, R., Braga-Ribas, F., Benedetti-Rossi, G., Camargo, J. I. B.,
 2232 Dias-Oliveira, A., Morgado, B., Gomes-Júnior, A. R., Vieira-Martins, R., Behrend, R., Tirado, A.
 2233 C., Duffard, R., Morales, N., Santos-Sanz, P., Jelínek, M., Cunniffe, R., Querel, R., Harnisch, M.,
 2234 Jansen, R., Pennell, A., Todd, S., Ivanov, V. D., Opitom, C., Gillon, M., Jehin, E., Manfroid, J.,
 2235 Pollock, J., Reichart, D. E., Haislip, J. B., Ivarsen, K. M., LaCluyze, A. P., Maury, A., Gil-Hutton,
 2236 R., Dhillon, V., Littlefair, S., Marsh, T., Veillet, C., Bath, K.-L., Beisker, W., Bode, H.-J., Kretlow,
 2237 M., Herald, D., Gault, D., Kerr, S., Pavlov, H., Faragó, O., Klös, O., Frappa, E., Lavyssière, M.,
 2238 Cole, A. A., Giles, A. B., Greenhill, J. G., Hill, K. M., Buie, M. W., Olkin, C. B., Young, E. F., Young,
 2239 L. A., Wasserman, L. H., Devogèle, M., French, R. G., Bianco, F. B., Marchis, F., Brosch, N.,
 2240 Kaspi, S., Polishook, D., Manulis, I., Ait Moulay Larbi, M., Benkhaldoun, Z., Daassou, A., El
 2241 Azhari, Y., Moulane, Y., Broughton, J., Milner, J., Dobosz, T., Bolt, G., Lade, B., Gilmore, A.,
 2242 Kilmartin, P., Allen, W. H., Graham, P. B., Loader, B., McKay, G., Talbot, J., Parker, S., Abe, L.,
 2243 Bendjoya, P., Rivet, J.-P., Vernet, D., Di Fabrizio, L., Lorenzi, V., Magazzú, A., Molinari, E.,
 2244 Gazeas, K., Tzouganatos, L., Carbognani, A., Bonoli, G., Marchini, A., Leto, G., Sanchez, R. Z.,
 2245 Mancini, L., Kattentidt, B., Dohrmann, M., Guhl, K., Rothe, W., Walzel, K., Wortmann, G., Eberle,
 2246 A., Hampf, D., Ohlert, J., Krannich, G., Murawsky, G., Gährken, B., Glostein, D., Alonso, S.,
 2247 Román, A., Communal, J.-E., Jabet, F., deVisscher, S., Sérot, J., Janik, T., Moravec, Z.,
 2248 Machado, P., Selva, A., Perelló, C., Rovira, J., Conti, M., Papini, R., Salvaggio, F., Noschese, A.,
 2249 Tsamis, V., Tigani, K., Barroy, P., Irzyk, M., Neel, D., Godard, J. P., Lanoiselée, D., Sogorb, P.,
 2250 Vérilhac, D., Bretton, M., Signoret, F., Ciabattari, F., Naves, R., Boutet, M., De Queiroz, J.,
 2251 Lindner, P., Lindner, K., Enskonatus, P., Dangl, G., Tordai, T., Eichler, H., Hattenbach, J.,
 2252 Peterson, C., Molnar, L. A., & Howell, R. R., 2019. Lower atmosphere and pressure evolution on
 2253 Pluto from ground-based stellar occultations, 1988-2016. *Astronomy and Astrophysics*, 625, A42.
- 2254 Moore, J. M., Spencer, J. R., 1990. Koyaanismuuyaw - The hypothesis of a perennially
 2255 dichotomous Triton. *GRL* 17, 1757-1760.
- 2256
- 2257 Moore, M. H., Hudson, R. L., 2003. Infrared study of ion-irradiated N₂-dominated ices relevant to
 2258 Triton and Pluto: formation of HCN and HNC. *Icarus* 161, 486-500.
 2259 [http://dx.doi.org/10.1016/S0019-1035\(02\)00037-4](http://dx.doi.org/10.1016/S0019-1035(02)00037-4).
- 2260
- 2261 Nimmo, F., & Spencer, J. R., 2015. Powering Triton's recent geological activity by obliquity tides:
 2262 Implications for Pluto geology. *Icarus*, 246(C), 2-10. <https://doi.org/10.1016/j.icarus.2014.01.044>.
- 2263

2264 Nogueira, E., Brassier, R., & Gomes, R., 2011. Reassessing the origin of Triton. *Icarus*.
2265 <https://doi.org/10.1016/j.icarus.2011.05.003>.

2266

2267 Olkin, C. B., Elliot, J. L., Hammel, H. B., Cooray, A. R., McDonald, S. W., Foust, J. A., Bosh, A.
2268 S., Buie, M. W., Millis, R. L., Wasserman, L. H., Dunham, E. W., Young, L. A., Howell, R. R.,
2269 Hubbard, W. B., Hill, R., Marcialis, R. L., McDonald, J. S., Rank, D. M., Holbrook, J. C., &
2270 Reitsema, H. J., 1997. The thermal structure of Triton's atmosphere: Results from the 1993 and
2271 1995 occultations. *Icarus*, 129(1), 178–201. <https://doi.org/10.1006/icar.1997.5757>.

2272

2273 Paige, D. A., 1985. The Annual Heat Balance of the Martian Polar Caps from Viking Observations.
2274 Ph.D. thesis, Calif. Inst. of Technol., Pasadena.

2275

2276 Pankine, A. A., Tamppari, L. K., Smith, M. D., 2009. Water vapor variability in the north polar
2277 region of Mars from Viking MAWD and MGS TES datasets. *Icarus* 204, 87–102.
2278 doi:10.1016/j.icarus.2009.06.009.

2279

2280 Pankine, A. A., Tamppari, L. K., Smith, M. D., 2010. MGS TES observations of the water vapor
2281 above the seasonal and perennial ice caps during northern spring and summer. *Icarus* 210, 58–
2282 71. doi:10.1016/j.icarus.2010.06.043.

2283

2284 Prokhvatilov, A.I., Yantsevich, L.D., 1983. X-ray investigations of the equilibrium phase diagram
2285 of CH–N, solid mixtures. *Sov. J. Low Temp. Phys.* 9, 94–97.

2286

2287 Protopapa, S., Grundy, W. M., Reuter, D. C., Hamilton, D. P., Dalle Ore, C. M., Cook, J. C.,
2288 Cruikshank, D. P., Schmitt, B., Philippe, S., Quirico, E., Binzel, R. P., Earle, A. M., Ennico, K.,
2289 Howett, C. J. A., Lunsford, A. W., Olkin, C. B., Parker, A., Singer, K. N., Stern, A., Young, L. A.,
2290 2017. Pluto's global surface composition through pixel-by-pixel Hapke modeling of New Horizons
2291 Ralph/LEISA data. *Icarus*, 287, 218–228. <https://doi.org/10.1016/j.icarus.2016.11.028>.

2292

2293 Quirico, E., S. Douté, B. Schmitt, C. de Bergh, D.P. Cruikshank, T.C. Owen, T.R. Geballe, and
2294 T.L. Roush, 1999. Composition, physical state and distribution of ices at the surface of Triton.
2295 *Icarus*, 139, 159-178.

2296

2297 Ruiz, J., 2003. Heat flow and depth to a possible internal ocean on Triton. *Icarus* 166, 436–439.

2298

2299 Schenk, P. M., & Zahnle, K., 2007. On the negligible surface age of Triton. *Icarus*.
2300 <https://doi.org/10.1016/j.icarus.2007.07.004>.

2301

2302 Schenk P. M., Beyer R. A., McKinnon W. B., et al., 2018. Basins, fractures and volcanoes: Global
2303 cartography and topography of Pluto from New Horizons. *Icarus*, 314, 400-433.

2304

2305 Schenk, P. M., et al., 2021. Triton : Topography and Geology of a (Probable) Ocean World with
2306 Comparison to Pluto and Charon. Submitted.

2307

2308 Schmitt, B., Philippe, S., Grundy, W. M., Reuter, D. C., Côte, R., Quirico, E., Protopapa, S.,
2309 Young, L. A., Binzel, R. P., Cook, J. C., Cruikshank, D. P., Dalle Ore, C. M., Earle, A. M., Ennico,
2310 K., Howett, C. J. A., Jennings, D. E., Linscott, I. R., Lunsford, A. W., Olkin, C. B., ... Weaver, H.
2311 A., 2017. Physical state and distribution of materials at the surface of Pluto from New Horizons
2312 LEISA imaging spectrometer. *Icarus*, 287, 229–260. <https://doi.org/10.1016/j.icarus.2016.12.025>.

2313

2314 Smith, B. A., Soderblom, L. A., Banfield, D., Barnet, C., Basilevsky, A. T., Beebe, R. F., Bollinger,
2315 K., Boyce, J. M., Brahic, A., Briggs, G. A., Brown, R. H., Chyba, C., Collins, S. A., Colvin, T., Cook
2316 II, A. F., Crisp, D., Croft, S. K., Cruikshank, D., Cuzzi, J. N., Danielson, G. E., Davies, M. E., De
2317 Jong, E., Dones, L., Godfrey, D., Goguen, J., Grenier, I., Haemmerle, V. R., Hammel, H., Hansen,
2318 C. J., Helfenstein, C. P., Howell, C., Hunt, G. E., Ingersoll, A. P., Johnson, T. V., Kargel, J., Kirk,
2319 R., Kuehn, D.I., Limaye, S., Masursky, H., McEwen, A., Morrison, D., Owen, T., Owen, W.,
2320 Pollack, J. B., Porco, C. C., Rages, K., Rogers, P., Rudy, D., Sagan, C., Schwartz, J., Shoemaker,
2321 E. M., Showalter, M., Sicardy, B., Simonelli, D., Spencer, J., Sromovsky, L. A., Stoker, C., Strom,
2322 R. G., Suomi, V.E., Synott, S. P., Terrile, R. J., Thomas, P., Thompson, W. R., Verbiscer, A.,
2323 Veverka, J., 1989. Voyager 2 at Neptune – imaging science results. *Science* 246, 1422–1449.

2324

2325 Soderblom, L. A., Kieffer, S. W., Becker, T. L., Brown, R. H., Cook II, A. F., Hansen, C. J.,
2326 Johnson, T. V., Kirk, R. L., Shoemaker, E. M., 1990. Triton's geyser-like plumes: discovery and
2327 basic characterization. *Science* 250, 410–415.

2328

2329 Spencer, J. R., 1990. NITROGEN FROST MIGRATION ON TRITON: A historical model.
2330 *Geophysical Research Letters* 17, 1769–1772. doi:10.1029/GL017i010p01769.

2331

2332 Spencer, J. R., & Moore, J. M., 1992. The influence of thermal inertia on temperatures and frost
2333 stability on Triton. *Icarus*, 99(2), 261–272. [https://doi.org/10.1016/0019-1035\(92\)90145-W](https://doi.org/10.1016/0019-1035(92)90145-W).

2334

2335 Stansberry, J. A., Lunine, J. I., Porco, C. C., McEwen, A. S., 1990. Zonally averaged thermal
2336 balance and stability models for nitrogen polar caps on Triton. *Geophysical Research Letters* 17,
2337 1773–1776. doi:10.1029/GL017i010p01773.

2338

2339 Stansberry, J. A., Yelle, R. V., Lunine, J. I., McEwen, A. S., 1992. Triton's surface-atmosphere
2340 energy balance. *Icarus* 99, 242–260. doi:10.1016/0019-1035(92)90144-V.

2341

2342 Stansberry, J. A., Pisano, D. J., Yelle, R. V., 1996a. The emissivity of volatile ices on Triton and
2343 Pluto. *Planetary and Space Science* 44, 945–955. doi:10.1016/0032-0633(96)00001-3.

2344

2345 Stansberry, J. A., Spencer, J. R., Schmitt, B., Benchkoura, A.-I., Yelle, R. V., & Lunine, J. I.,
2346 1996b. A model for the overabundance of methane in the atmospheres of Pluto and Triton.
2347 Planetary and Space Science, 44, 1051.

2348

2349 Stern, S. A., McKinnon, W. B., 2000. Triton's Surface Age and Impactor Population Revisited in
2350 Light of Kuiper Belt Fluxes: Evidence for Small Kuiper Belt Objects and Recent Geological
2351 Activity. The Astronomical Journal 119, 945–952. doi:10.1086/301207.

2352

2353 Stern, S. A., Bagenal, F., Ennico, K., Gladstone, G. R., Grundy, W. M., Mckinnon, W. B., Moore,
2354 J. M., Olkin, C. B., Spencer, J. R., Weaver, H. A., Young, L. A., Andert, T., Andrews, J., Banks,
2355 M., Bauer, B., Bauman, J., Barnouin, O. S., Bedini, P., Beisser, K., Versteeg, M. H., 2015. The
2356 Pluto system: Initial results from its exploration by New Horizons.

2357

2358 Stone, E. C., Miner, E. D., 1989. The Voyager 2 encounter with the Neptunian system. Science
2359 246, 1417-1421.

2360

2361 Strobel, D. F., Summers, M. E., 1995. Triton's upper atmosphere and ionosphere. Neptune and
2362 Triton, 1107–1148.

2363

2364 Tan, S. P., & Kargel, J. S., 2018. Solid-phase equilibria on Pluto's surface. Monthly Notices of the
2365 Royal Astronomical Society, 474(3), 4254–4263. <https://doi.org/10.1093/mnras/stx3036>.

2366

2367 Tegler, S. C. and 13 colleagues, 2019. A New Two-molecule Combination Band as a Diagnostic
2368 of Carbon Monoxide Diluted in Nitrogen Ice on Triton. The Astronomical Journal 158.
2369 doi:10.3847/1538-3881/ab199f.

2370

2371 Trafton, L., 1984. Large seasonal variations in Triton's atmosphere. Icarus 58, 312-324.

2372

2373 Trafton, L. M., D. L. Matson, and J. A. Stansberry, 1998. Surface/atmosphere Interactions and
2374 Volatile Transport (Triton, Pluto and Io). Solar System Ices 227, 773.

2375

2376 Trafton, L. M., Stansberry, J. A., 2015. On the Departure from Isothermality of Pluto's Volatile Ice
2377 due to Local Insolation and Topography. AAS/Division for Planetary Sciences Meeting Abstracts
2378 #47.

2379

2380 Trafton, L. M., 2015. On the state of methane and nitrogen ice on Pluto and Triton: Implications
2381 of the binary phase diagram. Icarus, 246(C), 197–205.
2382 <https://doi.org/10.1016/j.icarus.2014.05.022>.

2383

2384 Tryka, K. A., Brown, R. H., Anicich, V., Cruikshank, D. P., Owen, T. C., 1993. Spectroscopic
2385 determination of the phase composition and temperature of nitrogen ice on Triton. *Science* 261,
2386 751-754.

2387

2388 Tryka, K. A., Brown, R. H., Chruikshank, D. P., Owen, T. C., Geballe, T. R., de Bergh, C., 1994.
2389 Temperature of nitrogen ice on Pluto and its implications for flux measurements. *Icarus* 112, 513–
2390 527. <http://dx.doi.org/10.1006/icar.1994.1202>.

2391

2392 Tyler, G. L., Sweetnam, D. N., Anderson, J. D., Borutzki, S. E., Campbell, J. K., Kursinski, E. R.,
2393 Levy, G. S., Lindal, G. F., Lyons, J. R., Wood, G. E., 1989. Voyager radio science observations
2394 of Neptune and Triton. *Science* 246, 1466-1473.

2395

2396 Umurhan, O. M., Howard, A. D., Moore, J. M., Earle, A. M., White, O. L., Schenk, P. M., Binzel,
2397 R. P., Stern, S. A., Beyer, R. A., Nimmo, F., McKinnon, W. B., Ennico, K., Olkin, C. B., Weaver,
2398 H. A., & Young, L. A., 2017. Modeling glacial flow on and onto Pluto's Sputnik Planitia. *Icarus*,
2399 287, 301–319. <https://doi.org/10.1016/j.icarus.2017.01.017>.

2400

2401 Vetter, M., Jodl, H.-J., Brodyanski, A., 2007. From optical spectra to phase diagrams—the binary
2402 mixture N₂-CO. *Low. Temp. Phys.* 33, 1052-1060.

2403

2404 White, O. L., Moore, J. M., McKinnon, W. B., Spencer, J. R., Howard, A. D., Schenk, P. M., Beyer,
2405 R. A., Nimmo, F., Singer, K. N., Umurhan, O. M., Stern, S. A., Ennico, K., Olkin, C. B., Weaver,
2406 H. A., Young, L. A., Cheng, A. F., Bertrand, T., Binzel, R. P., Earle, A. M., ... Schmitt, B., 2017.
2407 Geological mapping of Sputnik Planitia on Pluto. *Icarus*, 287, 261–286.
2408 <https://doi.org/10.1016/j.icarus.2017.01.011>.

2409

2410 Wood, S. E., and Paige, D. A., 1992. Modeling the martian seasonal CO₂ cycle: Fitting the Viking
2411 lander pressure curves. *Icarus* 99, 1–14.

2412

2413

2414 Young, L. A., Bertrand, T., Trafton, L. M., Forget, F., Earle, A. M. and Sicardy, B., 2021. Pluto's
2415 Volatile and Climate Cycles on Short and Long Timescales. In *The Pluto System After New*
2416 *Horizons* (S. A. Stern, J. M. Moore, W. M. Grundy, L. A. Young, and R. P. Binzel, eds), p.321-
2417 361. Univ. of Arizona, Tucson.

2418

2419 Young, L. A., 2017. Volatile transport on inhomogeneous surfaces: II. Numerical calculations
2420 (VT3D). *Icarus* 284, 443–476. doi:10.1016/j.icarus.2016.07.021.

2421

2422 Zent, A., et al., 1989, Grain size metamorphism in polar nitrogen ice on Triton. *Geophys. Res.*
2423 *Lett.* 16, 965-968.

2424 Appendix - Calculation of the temporal variations of Triton's
2425 subsolar latitude

2426

2427 In our volatile transport model, the calculation of Triton's subsolar latitude is performed by using
2428 a trigonometric equation corresponding to a fit of a solution obtained by a dynamic model of
2429 Triton's motion.

2430 The solution of the dynamic model was obtained over the period 06/09/-807 to 01/01/2100 using
2431 the *ephemph* application of the EPROC project (Berthier, 1998, Forget, 2000). The method,
2432 described by Le Guyader, 1993, includes the disturbances caused by Neptune's flatness at the
2433 poles (Peters, 1981), by the Sun and by the 8 other planets of the solar system, with their revised
2434 coordinates (Davies, 1996).

2435 The trigonometric fit of this solution is based on the trigonometric equation proposed by Harris
2436 (1984) and Trafton (1984), from a suggestion by Dobrovolskis (1980). Changes in subsolar
2437 latitude λ are expressed as a sinus function, resulting from the superposition of 3 harmonics of
2438 different amplitudes and frequencies, as :

2439

2440
$$\sin(\lambda(t)) = A \cos(\alpha_0 - \alpha_1 \mu) + B \sin(\alpha_0 - \beta_0 + (\beta_1 - \alpha_1) \mu) + C \sin(\alpha_0 + \beta_0 - (\alpha_1 + \beta_1) \mu)$$

2441

2442 With:

2443

$$\mu = \frac{365.25 t L_s}{D}$$

2444

2445 Where t is the time in Earth year from year 0 (i.e., t = 2000 corresponds to year 2000 A.D), L_s is
2446 the length of one Triton day in seconds (507773 s) and L_d is the length of one Triton day in Earth
2447 days (5.877 days).

2448 Since the work of Harris (1984) and Trafton (1984), the angles and coefficients have been revised
2449 (Berthier, 1998, Forget, 2000) and the values are:

2450

2451 $A = 0.429870$

2452 $B = 0.370543$

2453 $C = 0.0225091$

2454 $D = 31557595$

2455 $\alpha_0 = 241.52577^\circ$

2456 $\alpha_1 = 0.038142 \text{ rad/year}$

2457 $\beta_0 = -100.79473^\circ$

2458 $\beta_1 = 0.009131 \text{ rad/year}$

2459

2460 The first harmonic evolves at the frequency $\alpha_1 = 0.0381$ rad/year, which corresponds to the sidereal
2461 period of Neptune (165 Earth years). The second harmonic has a frequency equal to $(\beta_1 - \alpha_1)$ with
2462 β_1 the frequency corresponding to the precession of Triton's orbit around Neptune's pole (period
2463 = 650 Earth years). The period of this harmonic is ~ 221 Earth years. The third harmonic has a
2464 low amplitude compared to the others, and its frequency is equal to $(\alpha_1 + \beta_1)$, which corresponds
2465 to a period of 131.5 Earth years.

2466 The error made on the subsolar latitude by using the trigonometric equation (compared to the
2467 dynamical solution) is always smaller than 0.5° , which is largely sufficient for the purpose of this
2468 paper (the latitudinal resolution of our model is 7.5°). In fact, the errors are periodic and their
2469 analysis in frequency (Laskar, 1999) show that the frequency peaks at 82.2, 93.4 and 683.4 years
2470 with an amplitude of the order of 0.1° , while other peaks have an amplitude at least 10 times
2471 smaller.

2472 In conclusion, the trigonometric equation provides an excellent approximation of Triton's subsolar
2473 latitude that can be extrapolated in time. In our model, we compute the past climates of Triton by
2474 using these equations with t typically ranging from $t = -9 \times 10^6$ (9 million years ago) to $t = 2100$ (end
2475 of the current century). Note that over time, Triton's inclination is slowly increasing (getting closer
2476 to perfectly retrograde) and its precession period is slowly getting shorter as its orbit shrinks, but
2477 these are *very* long-term effects that are not significant over the timescale used in this paper (~ 10
2478 Myrs). The obliquity of Neptune does not change significantly over this period either (it is
2479 suggested to be primordial, Laskar and Robutel, 1993).

2480

2481

2482 Berthier, J., 1998. Définitions relatives aux éphémérides pour l' observation physique des corps
2483 du système solaire. Notes scientifiques et techniques du Bureau des longitudes, S061.

2484

2485 Davies, M.E., Abalakin, V.K., Bursa, M., Lieske, J.H., Morando, B., Morison, D., Seidelmann, P.K.,
2486 Sinclair, A.T., Yallop, B., Tjuflin, Y.S., 1996. Report of the TAU/IAG/COSPAR working group on
2487 cartographic coordinates and rotational elements of the planets and satellites: 1994. Celes. Mech
2488 63, 127-148.

2489

2490 Forget, F., Decamp, N., Hourdin, F., 1999. A 3D general circulation model of Triton's atmosphere
2491 and surface. In "Piuto and Triton, comparisons and evolution over time", Lowell Observatory's
2492 fourth annual workshop, Flagstaff, Arizona.

2493

2494 Laskar, J., 1999. Introduction to frequency map analysis. NATO ASI Hamiltonian Systems with
2495 Three or More Degrees of Freedom. C. Simd Ed. Kluwer, Dordrecht. 134-150.

2496

2497 Le Guyader, C., 1993. Solution of the N-body problem expanded into Taylor series of high orders.
2498 Applications to the solar system over large time range. Astron. Astrophys. 272, 687-694.

2499

2500 Harris, A. W., 1984. Physical characteristics of Neptune and Triton inferred from the orbital motion
2501 of Triton. Paper presented to I.A.U Colloquium 77, July 5-9, 1983 at Cornell Univ.

2502

2503 Peters, C. F., 1981. Numerical integration of the satellites of the outer planets. *Astron. Astrophys.*
2504 104, 37-41.
2505
2506
2507
2508
2509
2510
2511